

UCLA

UCLA Electronic Theses and Dissertations

Title

Biomaterials for Modulating VEGF-induced Angiogenesis through Specific Integrin Binding

Permalink

<https://escholarship.org/uc/item/7dc2208x>

Author

Li, Shuoran

Publication Date

2017

Peer reviewed|Thesis/dissertation

UNIVERSITY OF CALIFORNIA

Los Angeles

Biomaterials for Modulating VEGF-induced Angiogenesis through Specific Integrin Binding

A dissertation submitted in partial satisfaction
of requirements for the degree Doctor of Philosophy
in Chemical Engineering

by

Shuoran Li

2017

© Copyright by

Shuoran Li

2017

ABSTRACT OF THE DISSERTATION

Biomaterials for Modulating VEGF-induced Angiogenesis through Specific Integrin Binding

by

Shuoran Li

Doctor of Philosophy in Chemical Engineering

University of California, Los Angeles, 2017

Professor Tatiana Segura, Chair

The objective of this research was to study and engineer the signals that promote angiogenesis in the wound healing process. These signals include but are not limited to growth factors and integrin ligands. Extracellular matrix (ECM) molecules such as fibronectin, growth factors such as VEGF (vascular endothelial growth factors), and their receptors have been shown to be key regulators of angiogenesis and neovascularization, with embryos lacking these genes dying due to defects in angiogenesis^{1,2}. Currently, efforts to optimize angiogenic biomaterials have been focused dominantly on (1) controlling angiogenic factor release or presentation (the binding methods) and (2) modulating the material's bulk physical properties and integrin ligand density.

The controlled growth factor release and presentations have also been thoroughly studied. For example, the design of therapeutic angiogenic materials to treat cardiovascular diseases, such as deficient blood supply to the heart, limbs, and brain, has primarily been driven by the delivery of growth factors within a scaffold. Out of the entire library of growth factors, we selected VEGF as our model molecule, since it has been described as the master regulator of angiogenesis. Methods such as repeated low dosing of soluble VEGF, protease-responsive VEGF nanocapsules and covalently-bound VEGF in hydrogels have shown to promote regeneration of

functional healthy vessels. However, there are still many questions remaining to be answered in the field of growth factors. My dissertation focuses on answering three major ones: (1) How can we monitor the delivery of a growth factor in a signal-response cargo system, such as protease-degradable VEGF nanocapules? (2) Is there another presentation form of VEGF that can effectively promote therapeutic wound healing? (3) Besides the presentation method, does the distribution of growth factors across a substrate or within a matrix affect cellular response? Can we develop a screening system for it?

Aside from growth factors, integrins also play an important role in the process of angiogenesis. However, even though adhesive ligands that promote integrin binding are generally incorporated within therapeutic angiogenic materials, the subsequent cell-material interactions have not been explored as an angiogenic signal. As there are many different types of integrin pairs which exist in nature, we still do not fully understand the function of each one of them in the process of angiogenesis. In this dissertation, I hope to answer the question: Aside from bulk physical properties and integrin ligand density, does the integrin-specific design of biomaterials play a role in biomaterial-mediated angiogenesis? If so, then what type of role? I deeply investigated how integrins affect vessel morphogenesis and therapeutic outcomes using both the subcutaneous mouse and ischemic stroke mouse models. We discovered that integrin specificity can significantly impact the vascular outcomes. This work shows for the first time that precisely controlled integrin activation from a biomaterial can be harnessed to direct therapeutic vessel regeneration and reduce VEGF induced vascular permeability *in vivo*.

The dissertation of Shuoran Li is approved.

Luisa Iruela-Arispe

Yvonne Chen

Tatiana Segura, Committee Chair

University of California, Los Angeles

2017

Dedication

I dedicate this dissertation to my family and best friends.

Mom and Dad

Rex

Xin Nie

Wenshu Guo

Xinyu Fan

Cheng Mao

Meimei Zhang

Without all your love and support, this dissertation would not have been possible.

TABLE OF COTENTS

Chapter 1 Overview of dissertation and specific aims	1
1.1 Motivation and Objectives	1
1.2 Specific Aims.....	2
1.2.1 Specific Aim 1 (Chapter 3)	2
1.2.2 Specific Aim 2 (Chapter 4)	3
1.2.3 Specific Aim 3 (Chapter 5)	3
1.2.4 Specific Aim 4 (Chapter 6)	3
1.3 Dissertation Outline.....	4
Chapter 2 Introductions	6
2.1 Degradable nanoparticles monitoring	6
2.2 integrin ligands	8
2.2.1 Integrins in angiogenesis	8
2.2.2 Integrins in biomaterials.....	10
2.3 Vascular Endothelial Growth Factor (VEGF)	11
2.3.1 introduction of VEGF	11
2.3.2 VEGF regulates vascular development	13
2.3.3 Delivery of VEGF	14
2.3.4 Mechanism study of VEGF induced angiogenesis	18
2.4 Cellular response to nano-patterns	19
Chapter 3 High-throughput quantification of nanoparticle degradation using computational microscopy and its application to drug delivery nanocapsules	22
3.1 Introduction	22
3.2 Materials and methods.....	24
3.2.1 Materials used	24
3.2.2 Field-Portable Holographic On-Chip Microscope	25

3.2.3 Vascular Endothelial Growth Factor (VEGF) nanocapsule synthesis.....	26
3.2.4 VEGF nanoparticle degradation in solution	27
3.2.5 VEGF nanoparticles degradation on trypsin-coated coverslips	27
3.2.6 Measurement of trypsin amount on a surface	28
3.2.7 DLS Measurements	28
3.3 Result and discussions	28
3.4 Conclusions.....	36
Chapter 4 Integrin stimulation from bioengineered scaffolds dictates vascular patterning and reduces VEGF induced vascular permeability after stroke	37
4.1 Introduction	37
4.2 Materials and methods.....	39
4.2.1 Recombinant fibronectin fragments	39
4.2.2 Immobilization of Fn9*10 or Fn9(4G)10 on homogenous gold surface	40
4.2.3 Enzyme-linked immunosorbent assay (ELISA) on Fn9*10 or Fn9(4G)10 immobilized gold surface	41
4.2.4 Cell proliferation assay	41
4.2.5 Cell migration assay	42
4.2.6 2D Immunofluorescence Staining on Fragments Coated Cell Culture Plates	42
4.2.7 2D Immunofluorescence Staining on Fragments immobilized Gold Surfaces.....	43
4.2.8 Sprouting Assay with blank, full length Fibronectin, Fn9*10 or Fn9(4G)10 fibrin gels..	43
4.2.9 Quantification of Vessels and Tip Cells in Sprouting Assay	44
4.2.10 Sprouting Assay with RGD Presence	45
4.2.11 Anastomosis Sprouting Assay with Fn9*10 and Fn9(4G)10.....	45
4.2.12 Flow Cytometry	46
4.2.13 Integrin Blocking Sprouting Assay	46
4.2.14 VE-cadherin Staining on 3D Integrin-Blocking Assay.....	47

4.2.15 VE-cadherin Staining on 2D Fragments-Coated Surfaces	47
4.2.16 Hyaluronic Acid-Acrylate Synthesis	48
4.2.17 Vascular Endothelial Growth Factor Nanocapsules Synthesis	49
4.2.18 HA Hydrogel Storage Modulus Optimization	49
4.2.19 HA Gel Formula for SubQ Mice Model	50
4.2.20 SubQ Mice Model	50
4.2.21 SubQ Mice Model Quantification	51
4.2.22 Ischemic Stroke Model	52
4.2.23 Brain tissue processing	54
4.2.24 Microscopy and Morphoanalysis	54
4.3 Results and discussions	56
4.3.1 Design and characterization of Integrin-specific 2D surfaces	56
4.3.2 Integrin stimulation guides endothelial cell sprouting patterns	58
4.3.3 Matrices modified with RGD peptides show similar vascular pattern as Fn9(4G)10	66
4.3.4 Integrin stimulation guides vascular anastomosis	67
4.3.5 αv activation leads to pathological vasculature through VE-cadherin disruption	68
4.3.6 Integrin stimulation from a bioengineered matrix guides vascular patterns <i>in vivo</i>	72
4.3.7 $\alpha 3/\alpha 5\beta 1$ integrin binding reduces VEGF induced vascular permeability after stroke ...	77
4.4 Conclusions	82
Chapter 5 VEGF clusters improve diabetic skin wound healing	85
5.1 Introduction	85
5.2 Materials and methods	87
5.2.1 Synthesis of VEGF clusters	87
5.2.2 Excisional skin wound model	88
5.2.3 Histological Analyses	88
5.2.4 Immunofluorescent Staining and Analyses	89

5.2.5 Statistical Analysis	89
5.3 Results and discussion	90
5.4 Conclusions.....	95
Chapter 6.....	97
Ultra-large nano-patterned artificial surfaces for the study of distribution effects of biocues such as VEGF	97
6.1 Introduction	97
6.2 Materials and methods.....	99
6.2.1 Materials	99
6.2.2 Gold nanopatterned wafer fabrication.....	100
6.2.3 Heparin-ABH synthesis.....	100
6.2.4 Discontinuous nano-patterned VEGF surface (cVc) processing	101
6.2.5 Homogenous VEGF surface processing (Vc).....	101
6.2.6 Bound VEGF quantification	102
6.2.7 Bound VEGF visualization	102
6.2.8 Cell culture conditions.....	102
6.2.9 Cell exposure to VEGF conditions.....	103
6.2.10 Western blot analysis.....	103
6.2.11 Quantitative real-time PCR.....	104
6.2.12 Short-term exposure immunofluorescent staining	105
6.2.13 Overnight HUVEC spreading on cVc surface	105
6.2.14 Microprinting on nano-patterned surface	106
6.2.15 Cell seeding on microprinted fibronectin-immobilized nano-patterned surface	107
6.2.16 Statistical analysis	107
6.3 Results and discussion	108
6.3.1 Gold nanopatterned wafer fabrication.....	108

6.3.2 VEGF conjugation to nano-patterned glass surface	109
6.3.3 Protein level analysis on VEGFR-2 phosphorylation time course	113
6.3.4 Changes in gene expression in response to nanopatterned VEGF.....	117
6.3.5 2D cellular response to nanopatterned VEGF	119
6.3.6 Microprinting on nanopatterned fibronectin surfaces.....	121
6.4 Conclusions.....	122
Chapter 7 Conclusions and future directions.....	123
7.1 Introduction	123
7.2 Specific Aim 1 (Chapter 3).....	123
7.3 Specific Aim 2 (Chapter 4).....	125
7.4 Specific Aim 3 (Chapter 5).....	126
7.5 Specific Aim 4 (Chapter 6).....	127
Chapter 8 References	129

LIST OF FIGURES AND TABLES

Figure 1.1 The flow of the dissertation.	5
Figure 3.1(a) The photograph of the field portable holographic microscope. The device is about 25 cm in height and weighs less than 500 g. (b) The schematic of the physical hardware of the portable microscope. (c) Pictorial representation of the nanoparticle degradation by trypsin.....	24
Figure 3.2 Schematic of the vascular endothelial growth factor (VEGF) core protease-degradable nanoparticles.....	26
Figure 3.3 The mean particle size of the nanoparticles (L-VEGF, D-VEGF and ND-VEGF) measured by our computational holographic on-chip imaging platform following the degradation process at different time points.	30
Figure 3.4 Comparison between the size distribution of the nanoparticles between Dynamic Light Scattering (DLS) (a-c) and our computational imaging system. (d-f). The nanoparticles are as follows: (a), (d): L-VEGF; (b), (e): D-VEGF and (c), (f): Nondegradable VEGF.	31
Figure 3.5 Measurement of particle size distribution of commercialized polystyrene beads using DLS. The actual particle size and the measured particle size are mentioned in the figure.	32
Figure 3.6 DLS measurement of size distribution when trypsin is directly added to monomer solution. This shows that trypsin induces aggregation of the monomers.....	32
Figure 3.7 Average size of the nanoparticles following the degradation process, measured by our computational holographic on-chip imaging platform. The analysis was performed by averaging the sizes of over 350 nanoparticles, for all the samples, except the 1-day L-VEGF sample, which had lower recovery, with ~80 particles. Error bars denote the standard deviation. The P values are denoted as **: P<0.0015; **** : P<0.0001.	34

Figure 3.8 Schematic of the sandwich structure, depicting the interaction between each nanoparticle-nanolens complex and the trypsin on the surface of a substrate. 34

Figure 3.9 Monitoring the changes in the intensity of the lensfree holograms of the L (fast-degradable) VEGF nanoparticle/nanolens complexes following their contact with the trypsin-coated surface in the sandwich structure. The arrows indicate the selected nanoparticles used for the subsequent analysis reported in Figure 3.10..... 35

Figure 3.10 Temporal changes in the intensity of the lensfree holograms, each corresponding to individual nanoparticles, after their interaction with the trypsin coated surface. The color represents the particles selected in Figure 3.9. 36

Figure 4.1 2D characterizations of Human Umbilical Vascular Endothelial Cells (HUVECs) on Fn9*10 or Fn9(4G)10 coated glass bottom cell culture plate or on fragments immobilized heparin-based gold surfaces. (a) Immunofluorescence staining of $\alpha 5\beta 1$ and $\alpha v\beta 3$ integrin of HUVECs after 18 hours culture in 24-well glass bottom cell culture plate which was pre-coated with 500 μ l of 2 μ M Fn9*10 or Fn9(4G)10 overnight (scale bar 100 μ m). (b) Similar amounts of immobilized recombinant fibronectin fragments Fn9*10 and Fn9(4G)10 on gold surfaces indicated similar reactivity of these two fragments. (c) Immunofluorescence staining of $\alpha v\beta 3$ integrin, vinculin and PECAM for HUVECs after culturing 24 hours on top of fragments immobilized heparin-based gold surfaces (scale bar 50 μ m). (d) Proliferation study of HUVECs after 48 hours of culture on Fn9*10 or Fn9(4G)10 immobilized surfaces with 2ng/ml of VEGF (4 experiments, 8 wells from each experiment, normalized to control well without VEGF). (e) Migration speed analysis of HUVECs on top of Fn9*10 or Fn9(4G)10 immobilized gold surfaces (n=64). **** indicate P < 0.0001. (f) Migration path of HUVECs (overlapping of 64 individual cell path) on control gold surface, control gold

surface with 2ng/ml of VEGF, Fn9*10 and Fn9(4G)10 immobilized gold surfaces with 2ng/ml of VEGF..... 56

Figure 4.2 HUVEC sprouting is great affected by integrin activation from both fibrin matrices with and without full length fibronectin (Fn). (a) Representative immunofluorescent images for Human Umbilical Vascular Endothelial Cell (HUVEC) sprouting assay in both Fib1 (fibronectin and von Willebrand Factor containing Fibrinogen) and Fib3 (fibronectin and von Willebrand Factor depleted fibrinogen) fibrin gel with no fibronectin fragment, 2 μ M Fn9*10 (α 3/ α 5 β 1 specific matrices) or 2 μ M Fn9(4G)10 (α v β 3 specific matrices). Scale bar: 100 μ m. (b,c) Quantification of sprout number and branch points per bead in Fib3 matrices. (d,e) Quantification of sprout number and branch points per bead in Fib1 matrices ($n \geq 15$ HUVEC coated beads, from 3 independent gels). (f) Representative images and 3D views of HUVEC branch structures in both α v β 3 and α 3/ α 5 β 1 specific Fib3 matrices. Intra-loop and intra-joint branch structures were observed in α v β 3 condition (2 μ M Fn9*10) while organized branch structures were observed in α 3/ α 5 β 1 conditions (2 μ M Fn9(4G)10). Scale bar: 50 μ m. (g) Branch clusters per bead was analyzed in Fib3 blank conditions, Fib3+1 μ M Fn, α 3/ α 5 β 1 conditions (2 μ M Fn9*10) and α v β 3 conditions (2 μ M Fn9(4G)10). (h) Cluster number per sprout was analyzed in Fib3 blank conditions, Fib3+1 μ M Fn, α 3/ α 5 β 1 conditions (2 μ M Fn9*10) and α v β 3 conditions (2 μ M Fn9(4G)10). All plots represent mean \pm SD. * and ** indicate $P < 0.05$ and $P < 0.01$, respectively..... 59

Figure 4.3(a) Human Umbilical Vascular Endothelial Cell (HUVEC) sprouting assays were performed within both Fib1(Fn and Von Willebrand Factor containing Fibrinogen) and Fib3(Fn depleted Fibrinogen) matrices. Different amounts of exogenous of Fn were added to Fib3 to understand the effects of fibronectin on sprouting process. Total network length per bead including all sprouts and branches was shown here ($n \geq 15$, from 3 independent gels). (b) Quantification of total network length per bead in Fib3 matrices. (c) Quantification of

total network length per bead in Fib1 matrices. (d-f) The Fib3 (fibronectin-depleted) fibrin sprouting assay were repeated three times on different days. Normalized quantification of sprout number, branch points and total network length per bead with all three experiments were shown here. n=3, each day considered as one sample. (g-i) The Fib1 fibrin sprouting assay were repeated three times on different days. Normalized quantification of sprout number, branch points and total network length per bead with all three experiments were shown here. n=3, each day considered as one sample. (j) Quantification of cluster occurrence per bead in Fib3 (fibronectin-depleted) fibrin matrices with three repeated experiments in different days were shown here. n=3, each day considered as one biological replicate. (k) Quantification of cluster occurrence per bead in Fib1 fibrin matrices with three repeated experiments in different days were shown here. n=3, each experiment considered as one sample. *, **, *** and **** indicate $P < 0.05$, $P < 0.01$, $P < 0.001$ and $P < 0.0001$, respectively. 63

Figure 4.4 Intra-joint and intra-loop structure exist in matrices dosed with 9(4G)10 and RGD. (a) Microscopic analysis of whole bead sprouting outcomes (scale bar: 100 μm) and intra-joint and intra-loop branch structures (scale bar: 50 μm) from the blockage of integrin α_v , α_5 , β_1 or β_3 (5 $\mu\text{g}/\text{ml}$) of 2 μM Fn9*10 or 2 μM Fn9(4G)10 added Fib1 gels. (b) Branch cluster occurrence comparison between 2 μM Fn9(4G)10 Fib1 gels with and without α_v blocking (n=51 HUVEC coated beads from three independent gels). (c,d) Sprout number per bead and branch points per bead were quantified in 0,200,500 and 1000 μM RGD added Fib3 matrices (n \geq 15 HUVEC coated beads, from 3 independent gels). (e) Representative image of intra-loop and intra-joints structures in Fib3 matrices with 1000 μM RGD added. Scale bar: 50 μm . (f) Branch cluster occurrence per bead were quantified in 0,200,500 and 1000 μM RGD added Fib3 matrices. All plots represent mean \pm SD. *, **, *** and **** indicate $P < 0.05$, $P < 0.01$, $P < 0.001$ and $P < 0.0001$, respectively. 64

Figure 4.5 (a,b) Average branch cluster per bead and branch cluster distribution were analyzed for blank, $\alpha3/\alpha5\beta1$ specific (2 μ M Fn9*10) and $\alpha v\beta3$ specific (2 μ M Fn9(4G)10) Fib1 matrices. (c) Branch cluster distribution was analyzed for blank, 1 μ M Fn added, $\alpha3/\alpha5\beta1$ specific (2 μ M Fn9*10) and $\alpha v\beta3$ specific (2 μ M Fn9(4G)10) Fib3 matrices. (d,e) Cluster number per sprout and cluster number per branch were analyzed in blank, $\alpha3/\alpha5\beta1$ specific (2 μ M Fn9*10) and $\alpha v\beta3$ specific (2 μ M Fn9(4G)10) Fib1 conditions. (f) Cluster number per branch were analyzed in blank, 1 μ M Fn added, $\alpha3/\alpha5\beta1$ specific (2 μ M Fn9*10) and $\alpha v\beta3$ specific (2 μ M Fn9(4G)10) Fib3 conditions. (g,h) FACS analysis of the efficiency of αv blocking functional antibody P3G8. 1 μ g/ml of P3G8 in 100ul of media was shown to effectively bind to more than 95% of αv integrin on 60,000 HUVECs. (i,j) Microscopic analysis of whole bead sprouting outcomes (scale bar: 100 μ m) from the blockage of integrin αv , $\alpha5$, $\beta1$ or $\beta3$ (5 μ g/ml, replenished every 2 days) on 0.267 μ M Fn9*10 or 0.239 μ M Fn9(4G)10 dosed Fib1 and Fib3 matrices. (k,l) Microscopic analysis and quantification for total network length in 0,200,500 and 1000 μ M RGD modified Fib3 matrices. *,*** and **** indicate $P < 0.05$, $P < 0.001$ and $P < 0.0001$, respectively..... 65

Figure 4.6 Microscopic analysis of anastomosis process of EGFP-HUVEC sprouts at day 11. (a,d,g) Inter-beads branch overview of blank, 2 μ M Fn9*10 ($\alpha3/\alpha5\beta1$ specific) and 2 μ M Fn9(4G)10 ($\alpha v\beta3$ specific) Fib3 gels. Scale bar: 200 μ m. (b,e,h) Sample 1 of bead-bead tip cell interactions. Scale bar: 100 μ m. (c,f,i) Sample 2 of bead-bead tip cell interactions. Scale bar: 100 μ m. (j) Different tip-tip contact distribution within the 170 μ m of working distance of 60x objective..... 68

Figure 4.7 VE-cadherin disruption was observed on $\alpha v\beta3$ specific 2D surface and in 3D fibrin matrices. (a) Microscopic analysis of 2D VE-cadherin distribution on $\alpha3/\alpha5\beta1$ or $\alpha v\beta3$ specific surfaces without VEGF dosage after 12 hours. Scale bar: 50 μ m. ** indicate $P < 0.01$. (b) Quantification of VE-Cadherin to nuclei area ratio for HUVECs on $\alpha3/\alpha5\beta1$ or $\alpha v\beta3$

specific surfaces without VEGF dosage after 18 hours. (c) Grey value distribution analysis for 3 random cell-cell junctions on $\alpha3/\alpha5\beta1$ specific surface from (a). (d) Grey value distribution analysis for 3 random cell-cell junctions on $\alpha v\beta3$ specific surface from (a). (e) Microscopic analysis of VE-cadherin signals from blockage of αv integrin on $\alpha v\beta3$ specific Fib1 matrices (2 μ M Fn9(4G)10) in comparison to $\alpha3/\alpha5\beta1$ specific matrices. Scale bar: 100 μ m (whole bead) and 50 μ m (sprouts). 69

Figure 4.8 VE-cadherin disruption was observed on $\alpha v\beta3$ specific 2D surface with presence of VEGF and also in 3D fibrin matrices. (a) Microscopic analysis and quantification of 2D VE-cadherin distribution on fragment coated cell culture dish with 2ng/ml VEGF dosage at 12 hour time point. Scale bar: 50 μ m. .*** indicate P < 0.001. (b) Microscopic analysis of VE-cadherin signals from blockage of αv integrin on 0.239 μ M Fn9(4G)10 added Fib1 gels in comparison to 0.267 μ M Fn9*10 added Fib1 gels. (c) Microscopic analysis of VE-cadherin signals from blockage of αv integrin on 0.239 μ M Fn9(4G)10 added Fib3 gels in comparison to 0.267 μ M added Fn9*10 Fib3 gels. 71

Figure 4.9 (a-d) The workflow of modified matrigel plug assay. (e) Scheme for synthesising 100% L, 75% L, 50% L and 25% L protease-sensitive VEGF nanocapsules. (g) Scheme for implanted MMP-crosslinked HA Hydrogels containing fibronectin fragments (Fn9*10 or Fn9(4G)10) and equal amount of each type of VEGF nanocapsules. The HA hydrogels were also labeled with AF555 for visualization purposes.(f) Fluorescent analysis of D1 cell spreading after 2 days in HA hydrogels with 1, 5, 10, 20, 50 μ M of Fn9*10 dosage. 10 μ M fragment induced the most cell spreading without little apoptosis. (h) Optimization of storage modulus for the HA implant hydrogel by varying R ratio (crosslinker thiols to maleimide ratio)..... 72

Figure 4.10 (a) Schematic for light sheet microscopy detection system. (b) Bulk 3D visualization of isolectin-labeled vessel on the surface and inside of blank, $\alpha3/\alpha5\beta1$ specific, $\alpha\nu\beta3$ specific HA matrices (labeled as blue) after 14 days in vivo. (c) Zoom-in 3D heat map for vessel penetration visualization (HA matrices were labeled as blue). (d) Projection view for vessel penetration within blank, $\alpha3/\alpha5\beta1$ specific and $\alpha\nu\beta3$ specific matrices after 2 weeks in vivo. Scale bar: 100 μm 75

Figure 4.11 A modified matrigel plug assay using bioengineered hyaluronic acid (HA) hydrogels is utilized to assess angiogenesis in mice. (a) Comparison of normal mice skin vessel morphologies with the morphologies of infiltrated vessels on the surfaces of implanted blank, $\alpha3/\alpha5\beta1$ specific (10 μM Fn9*10) and $\alpha\nu\beta3$ specific (10 μM Fn9*10) HA hydrogels with VEGF nanocapsules (200ng per gel) 2 weeks after implantation. Scale bar: 200 μm . (b) Representative 40x images of vessels on the surface of $\alpha3/\alpha5\beta1$ specific and $\alpha\nu\beta3$ specific HA matrices. Scale bar: 50 μm . (c) Vessel totuosity comparison among blank, $\alpha3/\alpha5\beta1$ specific and $\alpha\nu\beta3$ specific conditions (n = 4 individual implants). (d) Heat map ananalysis of vessel distribution on the surfaces of blank, $\alpha3/\alpha5\beta1$ specific and $\alpha\nu\beta3$ specific matrices (n=4 individual implants). Darker box indicates higher vessel density in that region while white indicates the absence of vessels. Plot represents mean \pm SD.** indicate P < 0.01. 77

Figure 4.12 An middle cerebral atery occlusion (MCAo) ischemic stroke model was utilized to look at the effects of injected integrin-specific HA matrices on stroke repair 10 days post-injection (injection was performed 5 days post stroke). (a) Fibronectin(Fn) immunofluorescence staining on stroke site and cotralateral side of mouse brain 15 days post stroke showed enhanced Fn signals around stroke site. (b) Schematic illustration of mouse brain coronal sections showing a cortical stroke and the transplantation of an injectable hyaluronic acid (HA) hydrogel within the damaged area represented by the

asterisk. In order to protect the healthy parenchyma from nearby lesion area, star-shaped glial cells, astrocytes, elongate and surround the damaged site, forming the astrocytic scar. This stroke cavity is situated directly adjacent to the region of the brain that undergoes the most substantial repair and recovery, the peri-infarct tissue, where new structures such as vessels develop and infiltrate the infarct while undergoing a drastic remodeling process. The growing vasculature structure and permeability are both associated with tissue repair.

(c) Fluorescent microscopy showing brain vasculature in both the infarct and peri-infarct (stained for Glut-1 or Glut-1 plus tomato lectin intravascular perfusion) as well as leaked red blood cells (stained for Ter-119) in the no gel, 500 μ M RGD , 200ng soluble VEGF(Vs) + 500 μ M RGD, 200 ng Vs+ 10 μ M 9*10, 200ng VEGF nanocapsules (nV) + 10 μ M 9(4G)10 and 200ng nV + 10 μ M 9*10 conditions. VEGF nanocapsules were designed to slowly release VEGF. Scale bar: 100 μ m. (d,e) The results showed a significantly increased positive area for stained vessels in both the infarct and the per-infarct areas of nV+star transplanted mice compared with any other group. ** and *** indicate $P < 0.01$ and $P < 0.001$, respectively. (f) The measure of Ter-119 positive red blood cells in the two nV conditions show a significantly reduced area in the infarct site of nV+star ($\alpha 3/\alpha 5\beta 1$ specific matrices) transplanted mice compared with nV+4G ($\alpha v\beta 3$ specific matrices). This result shows that nV+star decreased leakiness of growing vessels in the stroke brain. * indicates $P < 0.05$. (g) The morphoanalysis of growing vessels in the peri-infarct area shows a significantly increased number of vascular ramifications in the nV+star condition compared with the nV+4G, suggesting that nV+star promotes a post-stroke vascular remodeling into a more physiological network. All plots represent mean \pm SD. * indicates $P < 0.05$ 80

Figure 4.13 (a) Non-stained control and non-primary antibody control of Fibronectin(Fn) immunofluorescence staining on stroke site and cotralateral hemisphere of mouse brain 15 days post stroke. (b) Data presented here showed positively stained vessels of the

contralateral hemisphere in both Glut-1 stained conditions or Glut1 plus tomato lectin perfused conditions. No significant difference was shown on positive vascular area percentage and vessel morphology between these two conditions. Scale bar: 100 μ m..... 81

Figure 4.14 Summary figure for in vitro sprouting assay, in vivo subcutaneous modified matrigel assay and in vivo ischemic stroke model. In conclusion, α 3/ α 5 β 1 and α v β 3 integrin-specific materials regulate angiogenesis process differently both in vitro and in vivo. α 3/ α 5 β 1 specific materials affects vascular patterning in vivo by reducing vessel tortuosity and also promoting the development and maturation of newly formed vessels in the damaged brain, thus representing a promising candidate in the design of therapeutic pro-angiogenic scaffolds..... 83

Figure 5.1 (a) Scheme for heparin nanoparticles and VEGF clusters synthesis. (b) Db/db mice skin wounds were induced at day 0. Mice were sacrificed at day 7 and wound images were taken and analyzed for blank fibrin gel (blk), soluble VEGF + gel(Vs), low clustered VEGF (lcV) and high clustered VEGF (hcV) conditions. Scale bar, 1mm. (c) Traces of wound-bed closure during seven days in vivo for each treatment category. (d) Quantification of the percentage of the remained wounds at day 7 (n=3-4). ** indicates P < 0.01..... 90

Figure 5.2 (a) Day 7 H&E representative images for blank fibrin gel (blk), soluble VEGF + gel(Vs), low clustered VEGF (lcV) and high clustered VEGF (hcV) conditions. Under blk condition, predominated neutrophils concentrated in the edges of the wound area, basal cells at the cut edges of the epidermis show increased mitotic activities, no regenerated epithelium formed and granulation tissue beneath the fibrin clot to fill the open wound area. Under Vs condition, neutrophils are still majority of inflammation cells that covered the surface of epidermis gap, fibrin clot deposited in the dermis are partially replaced by neutrophils and monocytes, still no regenerated epithelium was yielded. Under lcV

condition, wound space is wide open and no granulation tissue filled into the wound area except in the margin. A thin layer of base membrane with scattered neutrophils and monocytes continuously grows to cover the base of wound area. Under hcV condition, neovascularization begins emerge, collagen fibrin begins to bridge the wound area with increased fibroblast. A continuous layer of regenerated epithelium is formed and covers the whole wound area. (b) Comparison of epithelial layer thickness at day 7 (n=3-4, one way anova). ** indicates $P < 0.01$ 92

Figure 5.3(a) Full-scan K14 immunofluorescent representative images for blank fibrin gel (blk), soluble VEGF + gel(Vs), low clustered VEGF (lcV) and high clustered VEGF (hcV) conditions. Scale bar, 1mm. (b) Quantification of K14 staining gap distance at day 7 (n=3-4, one way anova). * indicates $P < 0.05$ 93

Figure 5.4 (a) Representative images for CD31 and NG2 immunofluorescent staining. Top row scale bar, 100 μ m. Bottom row scale bar, 50 μ m. (b) Schematic for endothelial cells (CD31) and pericytes (NG2) interaction. (c,d) Quantification of area percentage of CD31+ and NG2+ cells in granulation tissue at day 7 (n=3-4). **** indicates $P < 0.0001$ 94

Figure 6.1 Schematic of the wafer fabrication process. 97

Figure 6.2 CD-SEM images of photoresist mask and gold nanopatterned glass wafers. (A) Representative matrix of focus offset (vertical axis) and UV exposure energy (horizontal axis) used to generate a range of hole sizes and morphologies on the photoresist layer using a photomask designed for 300 nm holes at a 1.67 μ m pitch. Numbers on the panels reflect the approximate hole diameters measured using the imaging software. (B) Size and morphology of the features before and after gold deposition using an e-beam evaporator. The photoresist mask (left) was lifted off using AZ300T stripper, followed by sonication in

acetone to reveal standing gold cylinders (right).(C) Representative photo of nano-patterned substrate. 109

Figure 6.3 Schematic of the VEGF conjugation procedure. 111

Figure 6.4 Specific binding of VEGF to gold nanopatterned features on glass. (A) Bulk surface concentration of VEGF on homogeneous gold-coated glass (Vc), heterogeneous gold nanopatterned glass (cVc) and bare glass (Vg) following identical VEGF conjugation protocols. Silanization of exposed glass surfaces using mPEG-silane was necessary to reduce non-specific adsorption of VEGF to the non-patterned surface (compare clear and filled columns). (B) Conjugated VEGF on gold nanopatterned glass visualized by standard immunofluorescent techniques employing a primary anti-VEGF antibody and fluorescently-tagged secondary antibody. The gold islands were visualized under brightfield and overlaid with the fluorescent images, demonstrating specific binding of VEGF to the gold nanofeatures (cVc+). The no VEGF control (cVc-) processed in the absence of VEGF demonstrated no fluorescence under identical imaging conditions. (C) Representative immunofluorescent images of HUVECs seeding on cVc surface. 112

Figure 6.5 Time course for the phosphorylation status of VEGFR-2 at the tyrosine 1175 and 1214 residue (pY1175, pY1214 respectively) of cells in contact with different forms of VEGF quantified using Western blot densitometry. (A, B) Phosphorylation time course of VEGFR-2 from cells in contact with soluble VEGF (Vs+; solid circles) or the no VEGF buffer control (Vs-; empty circles). (C, D) Phosphorylation time course of VEGFR-2 from cells in contact with VEGF covalently conjugated on a continuous gold film at high concentration (Vc+ high; solid squares) or low concentration (Vc+ low; solid circles), and gold film with no VEGF (Vc-; empty circles). (E, F) Phosphorylation time course of VEGFR-2 from cells in contact with VEGF covalently conjugated on a gold nanopattern (cVc+; solid circles), and gold

nanopattern with no VEGF(cVc-; empty circles). (G) Relative phosphorylation of ERK1/2. (H) Relative phosphorylation of p38. (I) Relative phosphorylation of Akt..... 114

Figure 6.6 Fold change in mRNA levels (relative to the corresponding negative controls) of the VEGFRs and Notch ligands from cells in contact with different forms of VEGF quantified using quantitative real time PCR. (A) Fold change in VEGFR-1 mRNA levels. (B) Fold change in VEGFR-2 mRNA levels. (C) Fold change in VEGFR-3 mRNA levels. (D) Fold change in Dll4 mRNA levels. (E) Fold change in Jag1 mRNA levels. (F) Fold change in Dll1 mRNA levels..... 118

Figure 6.7 Intracellular distribution of Jagged1 (green) and Dll4 (red) in cells in contact with different forms of VEGF imaged using confocal microscopy. Hoescht 33528 (blue) was used to stain the nuclei. (A-C) Intracellular distribution of Jagged1, Dll4, and the overlay (with Hoescht) in cells exposed to Vs for 30 min. (D-F) Intracellular distribution of Jagged1, Dll4, and the overlay (with Hoescht) in cells exposed to Vs for 120 min. (G-I) Intracellular distribution of Jagged1, Dll4, and the overlay (with Hoescht) in cells exposed to Vc high for 30 min. (J-L) Intracellular distribution of Jagged1, Dll4, and the overlay (with Hoescht) in cells exposed to Vc high for 120 min. (M-O) Intracellular distribution of Jagged1, Dll4, and the overlay (with Hoescht) in cells exposed to Vc low for 30 min. (P-R) Intracellular distribution of Jagged1, Dll4, and the overlay (with Hoescht) in cells exposed to Vc low for 120 min. (S-U) Intracellular distribution of Jagged1, Dll4, and the overlay (with Hoescht) in cells exposed to cVc for 30 min. (V-X) Intracellular distribution of Jagged1, Dll4, and the overlay (with Hoescht) in cells exposed to cVc for 120 min. 119

Figure 6.8 (A) Representative of microprinting outcomes on nanopatterned surface. (B) 10X images of D1 cells attachment on nanopatterned fibronectin surface with microprinting

patterns. (C)Enlarged image of D1 cells seeding on nanopatterned fibronectin surface within circular microprinting patterns..... 121

Table 4.1 HA Gel Formula for SubQ Mice Model..... 50

Table 4.2 HA Gel Formula for Ischemic Stroke Model 53

ACKNOWLEDGEMENTS

This dissertation would not have been possible without the help, guidance, and support of so many individuals.

First, I would like to thank my parents. Without their support and love, I wouldn't be able pursue my study in United States. As a daughter, I am really sorry that I spent so little time with them in the past 7 years. Without your guidance and encouragement, I would not be who I am right now. Thank you so much for your understanding and support, mom and dad.

I would also like to thank me husband, Rex. We met here in UCLA and it has really been a wonderful three years. Thank you so much for your encouragement when I was depressed. Thank you so much for helping me out when I am lost. I would not be able to survive the hardest time if you were not here.

Another super important person I would like to thank here is my supervisor, Tatiana Segura. You have been such a great mentor. All your guidance and support really mean a lot to me. Without your patience and caring, I wouldn't be able to complete my study in UCLA. I feel really lucky that I joined Segura Lab. The past six years in Segura Lab will become the best memory in my life.

I would also like to thank my best friends here. Guoguo, Xinyu, Meimei, Zhuxi and Sanjin, you are the most awesome people I have met! My life has been more splendid because of you! Best luck to all of you!

I would also like to thank my awesome labmates here. Talar, Anandika, Shiva, Allyson and Jon, thanks for your guidance when I first joined the lab. Don, Lina, Sasha Cai, Suwei, Cynthia, Nikki, Elias, Rob, Shayne, Yining, Victor, Norman and Weixian, it was really a great experience working with all of you! Wish all you guys achieve your dreams! Especially, I would also like to thank my undergrad Chris here. Thank for choosing me to be your mentor. I really enjoy the time we worked together and wish you a bright future.

I would also like to thank my collaborators from other labs here. Without your help, it would be impossible for me to experience so many interesting researches. Sincerely thanks to Helena Escuin, Peng Fei, Yichen Ding, Aniruddha Ray, Haylee Bachman, Prof. Antoni Ribas, Prof. Tzung Tsiai, Prof. Aydogan Ozcan, Prof. Thomas Barker and Prof. S. Thomas Carmichael.

Lastly, I would like to thank NIH funding number 1R01NS07969.

VITA

EDUCATION

Sep 10 – June 12 UCLA Department of Biomedical Engineering
Master of Science: Bioengineering

Sep 06 – July 10 Shanghai Jiao Tong University (SJTU)
Bachelor of Science: Applied Chemistry/ Bachelor of Arts: English

EXPERIENCE

Sep 11 – present Graduate Researcher, Segura Laboratory, UCLA
Integrin Activation as A Tool to Regulate Vascular Patterning

Designed specific integrin activation 2D system for human endothelial cell proliferation, migration and morphologies

Utilized 3D fibrin sprouting assay to investigate inter-bead and intra-bead tip cell interactions *via* confocal microscopy

Verified the *in vitro* findings *in vivo* by 2-week hydrogel implantation in SubQ balb/c mice model

Analyzed whole mount 3mm*1mm *in vivo* hydrogel samples *via* sheet confocal microscopy

2D Gold Islands Platform for Biocue Interactions and Clustering Effects Study

Designed 500nm diameter gold islands glass slide platform for biocue immobilization such as VEGF

Immobilized VEGF/ Integrin Co-signaling Study

Designed 2D synergy platform for pathway activation study of specific integrin activation together with VEGF

Utilizing Surface Plasmon Resonance and ELISA to verify the protein co-immobilization

Observed cell morphology changes *via* immunofluorescent staining

Oct 15 – Dec 15 Visiting Scholar, Leibniz Institute for Polymer Research, Germany

Partnered with an international scientist team of 30+ member to study HUVEC network formation in 3D matrix

Sept 11 – Sept 12 Student Chair, UCLA Career Center

Led a team of 9 in real-time updating internship/job lists and conducting student satisfaction surveys

Reviewed 100+ company websites, contacted 20+ companies by phone daily

Completed 47 internship opportunity lists (1000+ pages) on UCLA website which benefits 20,000+ students

Sent out student satisfaction surveys and logged student feedbacks into marketing database daily

Provided face-to-face resume critique services to 100+ drop-in students, hosted 10+ students' residential hall workshops

Feb 11 – June 12 Graduate Researcher, Lu Lab, UCLA

Nanocapsule Platform for Therapeutic Protein Delivery

Synthesized polymerization-protected tyrosinase nanocapsules for treatment of albinism

Established a dual-enzyme nanocapsule system for intracellular scavenge of reactive oxygen species

Built sound foundation for future design of complex multi-enzyme intracellular delivery system

Oct 08 – July 10 Lab Researcher, Group of Polymeric Biomaterials, SJTU

Dendrimer Carrier for Sustained Drug Release

Designed a pH-sensitive biocompatible pharmaceutical carrier for effectively cancer drug delivery *in vitro*

Achieved steady and consistent drug release rate for cancer treatment

POSTERS&PRESENTATIONS

- Li S.**, Barker T., Segura T. Integrin Activation as a Tool to Modulate Vascular Patterning. Stanford Bio-X & ADATE Symposium, Stanford, CA. 14 September 2016. Oral presentation.
- Li S.**, Barker T., Segura T. Integrin Activation as a Tool to Modulate Vascular Patterning. 2015 The International Society for Applied Cardiovascular Biology (ISACB), Nuremberg, Germany. 4 December 2015. Oral presentation.
- Li S.**, Barker T., Segura T. Integrin Activation as a Tool to Modulate Vascular Patterning. 2015 Society of Biomaterials, Charlotte, NC. 16 April 2015. Oral presentation.
- Li S.**, Barker T., Segura T. Integrin Activation as a Tool to Modulate Vascular Patterning. 2015 Tech Forum, Los Angeles, CA. 3 Feb 2015. Poster presentation.
- Li S.**, Soon A., Segura T. Co-immobilized VEGF and Fn Variants Alters VEGFR-2 Pathway Regulation and Enhances Angiogenesis. 2014 Tech Forum, Los Angeles, CA. 6 Feb 2014. Poster presentation.
- Li S.**, Soon A., Segura T. Co-immobilized VEGF and Fn Variants Alters VEGFR-2 Pathway Regulation and Enhances Angiogenesis. 2013 Vasculata, North American Vascular Biology Organization, San Diego, CA. 30 July 2013. Poster Presentation
- Soon A., Gojgini S., **Li S.**, Segura T. Modulation of Endothelial Cell Response Through Surface Patterning of VEGF. 2013 Society For Biomaterials Annual Meeting and Exposition, Boston, MA. 11 April 2013. Oral Presentation.

PUBLICATIONS

- Escuin-Ordinas H., **Li S.**, et al. "Cutaneous wound healing through paradoxical MAPK activation by BRAF inhibitors." *Nature Communications*, August, 2016.
- Sideris E., Griffin D., Ding Y., **Li S.**, Weaver W., Di Carlo D., Hsiai T., Segura T. "Particle Hydrogels Based on Hyaluronic Acid Building Blocks.", *ACS Biomaterials Science & Engineering*, Sept., 2016.

AWARDS

- 2015 UCLA International Travel Grant
- 2013 North American Vascular Biology Organization (NAVBO) Vasculata Scholarship
- 2006-2009 Academic Distinguished Scholarships of SJTU

Chapter 1

Overview of dissertation and specific aims

1.1 Motivation and Objectives

The design of therapeutic angiogenic materials to treat cardiovascular diseases, such as deficient blood supply to the heart, limbs, and brain, has primarily been driven by the delivery of angiogenic factors within a scaffold. Fibronectin, VEGF and their receptors have been shown to be key regulators of angiogenesis and neovascularization, with embryos lacking these genes, resulting in lethality due to defects in angiogenesis^{1,2}. Optimization of these materials has been focused dominantly on controlling angiogenic factor release or presentation and modulating bulk physical properties. The objective of this research was to understand and engineer the signals that promote wound healing. These signals include but not limited to growth factors and integrin ligands.

To study the effects from growth factors, we first wanted to evaluate the current nanocapsule technology for growth factor delivery and develop techniques to help us better visualize nanocapsules and monitor the degradation process. In our study, we used VEGF-core nanocapsules with different protease-degradability to test a portable computational imaging system. Second, we would also like to investigate how different formats of growth factor affects vessel regeneration process. In our study, we mainly investigated VEGF (Vascular Endothelial Growth Factor) in a cluster format. We would like to understand how different presentations of growth factors (not limited to soluble, electrostatically-bound, covalently-bound) actually affect therapeutic outcomes on diseased animal model. We hypothesized that this would help us

design more efficient growth factor delivery methods for therapeutic purposes. Third, we hoped to develop a universal system to look at the distribution effects of growth factors. We hypothesized that by generating a nano-patterned surface, the pathway activation from different distribution of growth factors can be studied. We hypothesized that even with the identical amount of growth factor dosage, the difference in distribution of growth factors can greatly affects cellular response.

For integrin activation studies, the objective is to understand how integrin activation guides endothelial cell fate. Although adhesive ligands that promote integrin binding are generally incorporated within therapeutic angiogenic materials, the subsequent cell-material interaction has not been explored as an angiogenic signal. It has been known that integrin activation can guide MSC (Mesenchymal Stem Cell) differentiation, yet no study has been done to really understand how the different integrin activation affect vessel regeneration. We hypothesized that materials with different integrin activation affects HUVEC sprouting and branching, which leads to different vessel morphogenesis and functionality.

1.2 Specific Aims

1.2.1 Specific Aim 1 (Chapter 3)

This aim developed a portable imager which detects nanocapsule degradation real-time. The VEGF nanocapsules with different protease-degradability were utilized as template in this study. Samples treated with protease at different time points were tested. Samples were also real-time imaged to monitor real-time degradation.

Hypothesis 1: Nano-lens based computational microscopy can be utilized as an effective tool to monitor nanocapsule degradation, such as protein-core VEGF nanocapsules.

1.2.2 Specific Aim 2 (Chapter 4)

This aim investigated the effects of specific integrin activation on angiogenesis. A 3D fibrin gel sprouting assay was carried out to study HUVEC sprouting and branching *in vitro*. Then a modified matrigel assay was performed on mouse model to look at neo-vessel infiltration and neo-vessel morphology. Later, an ischemic stroke mouse model was also utilized to study the neo-vessel generation and infiltration in the stroked area *in vivo*.

Hypothesis 2: Integrin-specificity matrix can be utilized to as a morphogenic cue in guiding endothelial cell responses both *in vitro* and *in vivo*. Specific integrin activation could induce the generation of healthy and non-leaky vessels.

1.2.3 Specific Aim 3 (Chapter 5)

This aim utilized the cluster format of VEGF to treat diabetic mouse cutaneous wounds. The wound closure percentage, epithelial layer thickness, endothelial cell and pericyte infiltration percentage were all studied.

Hypothesis 3: Clustered VEGF can promote diabetic cutaneous wound healing.

1.2.4 Specific Aim 4 (Chapter 6)

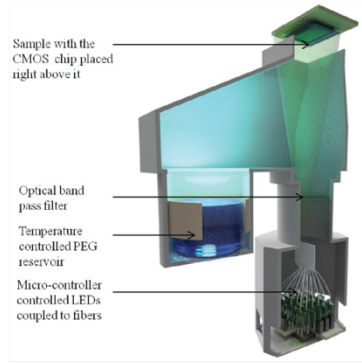
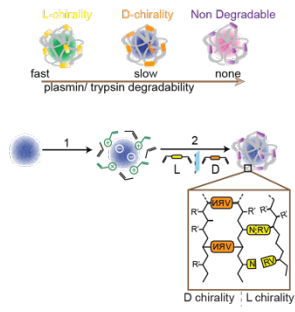
This aim designed a large nano-patterned surface to study the distribution effects of VEGF. VEGF was immobilized to nano-islands on ultra-flat glass surface which is about 600-700nm in diameter. Homogenous immobilized VEGF was used as control. VEGFR-2 activation study was performed using Western Blots and qPCR. HUVECs were later directly seeded on the nano-patterned surface to look at cell attachment and spreading.

Hypothesis 4: The discontinuous distribution of VEGF immobilization on nano-patterned surfaces will result in a distinct VR-2 phosphorylation pattern, downstream signal, EC morphology and phenotype compared with homogenous immobilized VEGF. Both western blot analysis and PCR technique can be used to analyze the outcomes on the protein and mRNA expression levels.

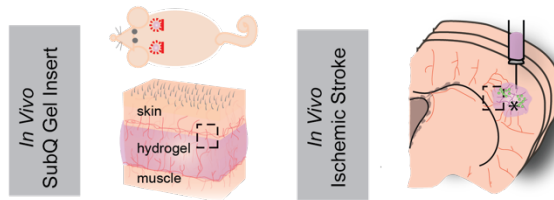
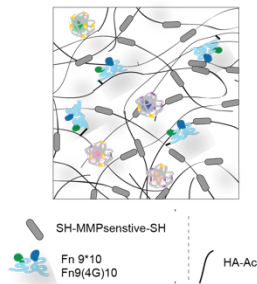
1.3 Dissertation Outline

After this introductory Chapter, Chapter 2 will provide relevant background to the dissertation topic. The flow of the dissertation is illustrated in Figure 1.1. After testing the VEGF nanocapsules degradability using computational imaging system (Chapter 3), the VEGF nanocapsules were incorporated into hydrogel matrix together with different types of integrin-specific fibronectin fragments to look at the effects of integrin specificity on angiogenesis outcomes both in subcutaneous mouse model and stroke mouse model (Chapter 4). After determining the angiogenesis effects from integrin specificity, the research actually turned to investigate the different presentation formats of VEGF, which is the master regulator in angiogenesis. VEGF clusters were dosed on diabetic mouse model to study the effects of VEGF clusters on cutaneous wound healing (Chapter 5). Besides looking at the angiogenesis effects from different growth factor presentation, the discontinuous distribution effects of growth factor was also studied. Here, VEGF is still used as a template. The nano-patterns with discontinuous VEGF immobilization was compared with homogeneous distributed VEGF to look at the difference in VEGFR-2 activation (Chapter 6).

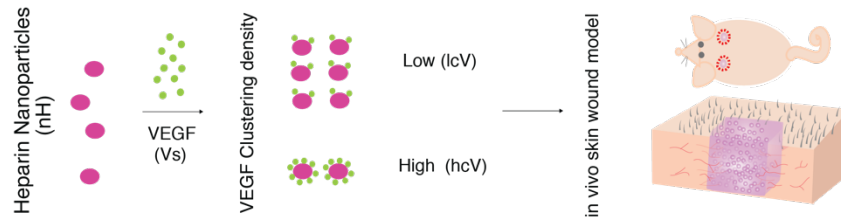
Aim 1: Hypothesis 1 (Chapter 3)



Aim 2: Hypothesis 2 (Chapter 4)



Aim 3: Hypothesis 3 (Chapter 5)



Aim 4: Hypothesis 4 (Chapter 6)

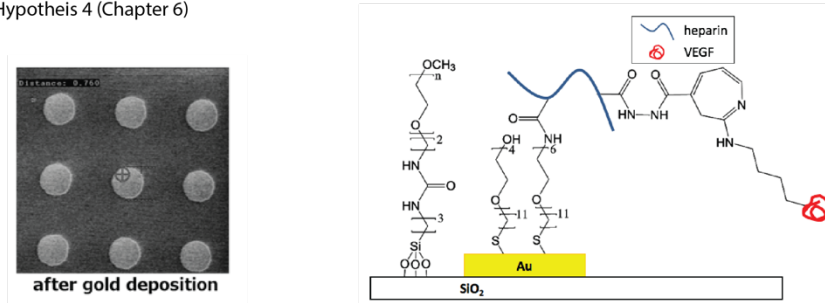


Figure 1.1 The flow of the dissertation.

Chapter 2

Introductions

2.1 Degradable nanoparticles monitoring

Design and synthesis of degradable nanoparticles are very important in drug delivery and bio-sensing fields. Although accurate assessment of nanoparticle degradation rate would improve the characterization and optimization of drug delivery vehicles, current methods rely on estimating the size of the particles at discrete points over time using e.g., electron microscopy or dynamic-light-scattering (DLS), among other techniques, all of which have several drawbacks and practical limitations. There is a significant need for a high-throughput and cost-effective technology to accurately monitor nanoparticle degradation as a function of time and using small amounts of sample. To address this need, here we present two different computational imaging based methods for monitoring and quantification of nanoparticle degradation. The first method is suitable for discrete testing, where a computational holographic microscope is designed to track the size changes of protease-sensitive protein-core nanoparticles following degradation, by periodically sampling a subset of particles mixed with proteases. In the second method, a sandwich assay was utilized to observe, in real-time, the change in the properties of liquid nanolenses that were self-assembled around degrading nanoparticles, permitting continuous monitoring and quantification of the degradation process. These cost-effective holographic imaging based techniques enable high-throughput monitoring of the degradation of any type of nanoparticles, using an extremely small amount of sample volume that is at least three orders of magnitude smaller than what is required by e.g., DLS-based techniques.

Over the past few decades nanotechnology has been utilized extensively in biomedical sciences for a variety of applications such as oncology, cardiology, wound healing, and many others¹. Various types of nanoparticles have been designed and synthesized to deliver different payloads, such as drug molecules, proteins, nucleic acids to target cells or tissues². Compared with bulk delivery without a carrier, utilization of nanoparticle carriers offers several advantages, such as drug stability, controlled release rate and also targeted delivery. A nanoparticle carrier is generally designed (*i*) to protect its cargo from *in vivo* degradation and external perturbations to its physical and bio-chemical properties and (*ii*) to deliver the drug at controlled dosages. Additionally, surface modification of nanoparticles enables specific targeting to particular cells, which helps in reducing cellular toxicity, especially in chemotherapy, improves systematic circulation time and increases retention at target sites, such as tumor^{3,4}. It can also be utilized to simultaneously carry multiple drugs to the same target, such as a chemo-drug and a sensitizer⁵.

To achieve controlled drug delivery, nanoparticles are often designed to be degradable⁶. An important design principle of degradable nanoparticles is that they degrade into non-toxic components that can be cleared by the body. Generally, such nanoparticles are designed to undergo degradation triggered and facilitated by the local microenvironment that is specific to the targeted disease. Different diseases can lead to formation of unique microenvironments at the cellular or tissue level, as a hallmark of the disease. For example, certain tumor microenvironments are characterized by elevated glutathione levels, low pH and increased protease activity, wounds are characterized by lower oxygen and higher protease levels, etc. These known features of some diseases have been exploited to develop specific nanocarriers, with degradation mediated by e.g., pH^{7,8}, glutathione⁹, proteases, enzymes^{10,11}, antigens¹² etc. Another common approach is to design nanoparticles that can release drugs after degradation due to external perturbations such as light¹³, heat^{14,15}, ultrasound, electric¹⁶ and magnetic fields^{17,18}.

During their design and test phase, the most commonly used method for observing nanoparticle degradation is by correlating it with the amount of drug released¹⁴. The drug release is monitored by isolating the free drug molecules followed by direct quantification using analytical or bio-chemical techniques or by indirectly monitoring its effect. However, these methods can only be used for drug loaded nanoparticles undergoing degradation. In general, design and synthesis of biodegradable nanoparticles, without the cargo, require a direct method for observing and quantification of the changes in their matrix. Several techniques such as Raman spectroscopy¹⁹, fluorescence resonance energy transfer²⁰, optical absorption^{21,22,23} and Magnetic Resonance Imaging (MRI)²⁴ have been previously utilized to monitor the degradation process of the nanoparticle matrix. However, these methods can only be used for specific types of nanoparticles and are not universally applicable for any type of particle. Some of the more general strategies that have been used for monitoring nanoparticle degradation involve measurement of weight or size by using chromatography²⁵, dynamic light scattering (DLS)¹⁴ and electron microscopy (EM)²⁶. These methods can provide an estimation of the nanoparticle degradation process but each has its own set of drawbacks. For example, EM is performed on dry samples and thus it is not possible to perform degradability measurements with most polymeric nanoparticles, such as hydrogels, liposomes etc. DLS, on the other hand, can perform measurements in solution but is not very accurate and also is quite limited in terms of the dynamic range of particle size and density that can be measured, often requiring large amounts of sample volume for each measurement.

2.2 integrin ligands

2.2.1 Integrins in angiogenesis

Integrins are family of heterodimeric transmembrane proteins that mediate cell surface binding to the extracellular matrix (ECM) and intracellular actin cytoskeletal components³. These

receptors are formed by pairs of alpha (α) and beta (β) subunits, and have been associated with processes ranging from cell structure and adhesion to cell differentiation and survival, which are cell behaviors critical to tissue morphogenesis, homeostasis and repair³⁻⁵. It is known that the expression of integrins can vary as a function of time and/or environment to support a variety of tissue remodeling events. For example, $\beta 1$ integrin expression was slowly upregulated on the brain vessels overtime as vessels gets more mature⁶. Another example would be $\alpha \beta 3$ expression in endothelial cells under different environments. Unlike resting endothelial cells which express little or no $\alpha \beta 3$, cytokine-activated endothelial cells or cells within malignant tumors showed markedly upregulated $\alpha \beta 3$ ⁷⁻⁹. Besides the expression level difference, functions of the same integrin can also vary between cell types and/or environmental states. For example, $\alpha 2 \beta 1$ on platelets is specific for collagen and not laminin¹⁰, however, on other cells it can recognize both ligands^{11, 12}.

When we look at endothelial cells specifically, at least seven α and β heterodimers ($\alpha \nu \beta 3$, $\alpha \nu \beta 5$, $\alpha \nu \beta 1$, $\alpha 1 \beta 1$, $\alpha 2 \beta 1$, $\alpha 3 \beta 1$ and $\alpha 5 \beta 1$) are expressed by endothelial cells and have been implicated in vascular morphogenesis and vessel patterning¹³⁻¹⁵. Though a complete understanding role of all these integrin pairs in the process of angiogenesis is yet to be available, the role of $\beta 1$ and $\beta 3$ integrins in angiogenesis is important in vascular lumen formation^{16, 17} and tight cell-cell junction formation^{16, 18-22}. Further, both up-regulation and abolishment of $\beta 1$ and $\beta 3$ integrin activation have shown to be related to pathological angiogenesis^{3, 20-25}. For example, while excessive suprabasal expression of $\beta 1$ integrin in skin has been shown to induce a psoriasis phenotype²⁴, the knockout of $\beta 1$ integrin resulted in the weakening of endothelial cell junctions and induction of blood leakage in a retinal angiogenesis assay²⁰. Likewise, the upregulation $\beta 3$ integrin leads to enhanced endothelial cell permeability²⁶ while the abolition of $\beta 3$ integrin leads to intrauterine bleeding, defective coronary capillaries, and

enhanced tumor angiogenesis (induced by the compensatory VEGF increase after $\beta 3$ knockout)^{21, 22, 25}.

Certain integrin types have been discovered in cancer progression and seems to be related to metastasis and provisional matrix invasion. The increased expression of integrins $\alpha\beta 3$ and $\alpha\beta 5$ seems to promote the binding of angiogenic endothelial cells to provisional matrix proteins such as vitronectin, fibrinogen, von willebrand factor, osteopontin and fibronectin that are deposited in the tumor microenvironment²⁷. On the contrary, other integrins are discovered to positively impact vessel maturation. For example, $\beta 1$ integrin is shown to promote vessel maturation and reduce vessel leakiness in central nervous system^{6, 20}. Likewise, $\alpha 4\beta 1$ integrin has shown to promote close intercellular interaction between endothelial cells and pericytes and thus is required for blood vessel maturation²⁸. Thus, it is extremely important to design proper ECM during the angiogenesis process is to present the growing vessels with the appropriate integrin binding ligands to generate normal, non-pathological vessels. Materials designed for therapeutic angiogenesis, should likewise, provide the appropriate integrin binding ligands to support revascularization of diseased tissues.

2.2.2 Integrins in biomaterials

The incorporation of integrin binding peptides derived from natural ECM proteins to biomaterials is a popular approach to promote integrin engagement²⁹⁻³⁴. Integrin-binding RGD peptide derived from fibronectin is by far the most widely utilized peptide in the generation of materials for cell growth *in vitro* or promote tissue repair *in vivo*. Though integrin-binding peptides can support cell attachment, migration, and differentiation, they have severely reduced binding affinity and specificity compared to the same peptide presented within 3D structure of the full-length protein. However, due to the enormous size and complexity of full-length ECM

proteins, the expression process is difficult and an alternative approach to present peptide motifs in a native 3D structural context is needed. One approach is to express only the integrin binding domains from the full-length protein, which is significantly smaller and less complex. For example, recombinant fibronectin (Fn) fragments of the 9th type III repeat and 10th type III repeat (Fn III9-10) have been expressed to present RGD sequence in the correct 3D structural context and improve binding affinity and specificity^{35, 36}. However, without the rest of the full-length protein these protein fragments do not contain the natural switches that modulate integrin engagement (e.g. native fibronectin can bind several integrin pairs depending on the level of extension of the protein³⁷⁻⁴⁰) and, thus, lack complete specificity.

Thus, the fibronectin 9th type III repeat and 10th type III repeat has been engineered further to promote $\alpha3/\alpha5\beta1$ specific binding and shown to enhance bone formation⁴¹, mesenchymal stem cell differentiation toward bone³⁵, and modulate epithelial to mesenchymal transition⁴². The extracellular matrix (ECM) has also been successfully engineered to coordinate and modulate simultaneous integrin and growth factor signaling to enhance vascularization, bone formation, and skin healing^{41, 43-48}.

2.3 Vascular Endothelial Growth Factor (VEGF)

2.3.1 introduction of VEGF

The VEGF family, in mammals, consists of five members: VEGF-A, B, C, D and Placenta growth factor (PLGF)⁴⁹⁻⁵¹. VEGF-A was initially discovered as a vascular permeability factor (VPF) associated with tumor growth in 1983^{49, 52}. In 1989, a few years after, Ferrara and Henzel, isolated a protein that induced the proliferation of endothelial cells and called it VEGF. Further studies showed that actually VEGF and VPF was the same molecule^{49, 50}.

Naturally, splicing of VEGF transcripts results in generation of different protein isoforms which regulates affinity for the extracellular matrix (ECM). In particular, the gene encoding VEGF-A consists of eight exons that are separated by seven introns, resulting in the generation of 206, 189, 183, 165, 148, 145 and 121 amino acids. VEGF-A 165 is the most abundant isoform followed by 121 and 189 isoforms. VEGF-A 165 and 121 differs from each other only by lack of exon 7 in 121; as a consequence, 165 isoform binds heparan sulfate proteoglycans in the extracellular matrix, whereas the 121 does not. Another splice variant of VEGF-A, known as VEGF-A 165b, an inhibitory isoform, has been proposed to negatively regulate VEGFR activity. In mice, VEGF-A isoforms are one amino acid shorter than their corresponding human isoforms^{49, 50, 52, 53}.

VEGF binds to VEGFRs which are members of the receptor tyrosine kinases (RTKs) superfamily and are equipped with an approximately seven immunoglobulin-(Ig)-like domains in the extracellular domain. VEGF-A binds to both VEGFR-1(Flt-1) and VEGFR-2(Flk-1/KDR) which are primarily expressed in vascular endothelial cells, whilst VEGF-C and D bind to VEGFR-3(Flt-4) which is exclusively expressed in lymphatic endothelial cells. VEGFs also interact with a family of co-receptors, such as neuropilins (NRP) and HSPG^{49, 51, 52}.

In Angiogenesis, the first and the most leading cells to start a vessel branch is the “tip cell” which is specialized of endothelial cells with their numerous filopodia that respond and migrate toward angiogenic stimulus in the microenvironment. Stalk cells, on the other hand, proliferate behind the tip cells and form lumen. Tip cells are characterized by the expression of VEGF receptor (VEGFR) 2, VEGFR3, platelet-derived growth factor (PDGF)-BB, Delta-like ligand-4(Dll4) and others. The communication of tip-to-stalk cell is controlled by NOTCH signaling pathway. In response to the VEGF stimuli, tip cells will become specialized by the expression of Dll4, which activates Notch in stalk cells, which reduces stalk sensitivity to VEGF stimulation, down regulates VEGFR2 signaling and consequently suppresses tip cell phenotype

in the neighboring cells. Different VEGF isoform, soluble or matrix-bound forms stimulate more lumen formation for the former or more branches formation for the latter⁵⁴⁻⁵⁶.

2.3.2 VEGF regulates vascular development

Vascular endothelial growth factor (VEGF) is one of the most widely studied and applied growth factors that regulate vascular development. Since a major obstacle in tissue regeneration is the lack of stable blood vessel infiltration into engineered tissue implants, VEGF has been extensively utilized as a means to induce vascularization^{57, 58}. To prevent diffusion and control release, VEGF has been encapsulated⁵⁹ and electrostatically⁶⁰ or covalently immobilized⁶¹⁻⁶⁴ to the tissue engineering scaffold. Although the end outcome of enhanced blood vessel formation *in vivo* is achieved^{63, 64}, the characterization of the bioactivity of VEGF-incorporated matrices *in vitro* has been limited to cellular migration and proliferation studies^{61, 65}, while extensive signaling studies have not been conducted until recently.

It is now known that growth factors, particularly VEGF, send different signals to endothelial cells when presented to their receptors with different degrees of matrix affinity^{66, 67}. By changing the growth factor affinity for the matrix, cells will receive different signals and behave accordingly. Incorporation of the heparin-binding (i.e. ECM binding) domain in exon 7 increases matrix affinity⁶⁸ and leads to induction of migration signaling over proliferative signaling⁶⁷. Developmental biology studies in mouse embryos have shown that the physical presentation of VEGF is critical to the development of a normal vasculature. The over-expression of VEGF with high matrix affinity results in aberrant vessels with reduced vessel thickness enhanced vascular branching and increased capillary density⁶⁹. In contrast, embryos expressing VEGF with no matrix affinity displayed poor branching and enlarged vessel diameter⁶⁹. Further, embryos expressing both VEGF with high and no matrix affinity contained a

normal vasculature⁶⁹, indicating that for normal vasculature to result a combination of soluble and bound VEGF must be present.

In the adult, VEGF physical presentation is also critical for angiogenesis; VEGF lacking the protease sensitive region but containing the matrix binding domain (resembles high matrix affinity VEGF) results in highly branched vessels, while VEGF lacking the matrix binding domain (resembles no matrix affinity VEGF) results in vascular hyperplasia and increased permeability⁷⁰. In the adult when VEGF without an ECM binding domain is presented to endothelial cells, the resulting blood vessel morphology becomes large and leaky, with extensive lumens⁶⁶. With the ECM binding domain included, VEGF leads to a vessel architecture that is smaller in diameter with more branching points. VEGF genetically engineered with a deletion of the MMP-cleaveable sequence, but with the ECM binding domain intact leads to a dense network of small capillaries⁶⁶. In a therapeutic setting, neither extreme in blood vessel morphology is desirable. Vessels should not be excessively branched (thin diameter) or large (thick diameter). For example, to achieve restoration of blood flow in a limb ischemic wound models both vessels size and number must increase⁷¹.

2.3.3 Delivery of VEGF

Endothelial cells can be activated by VEGF, which result in increased vessel permeability, cell migration and proliferation. However, when utilizing VEGF for therapeutic usage, there are three major obstacles. First, VEGF has short life. It has high instability once injected as a bolus from the attack of proteases. Second, the dosage matters. Local high amount of VEGF may result in deleterious effects including the formation of irregularly shaped sac-like vessels associated with massive and highly disruptive edema⁷² or even formation of endothelial cell-derived intramural vascular tumors⁷³. Third, sustained vessel formation needs

long-term stimulus. A short VEGF stimulus, if it is not sustained, is associated with the regression of the newly formed vessels when discontinued⁷².

All these leads to the need for sustained VEGF delivery. From one hand, it reduces the VEGF in-activation risk; from the other hand, it prevents negative outcomes from over-dosage while gives out long-term stimulation. Many methods are being developed for this purpose, such as nanoparticles, hydrogel matrix, etc. All these are good references for our design of delivery system in the future.

PLGA nanoparticles has been utilized for sustained VEGF release and more promising result for blood vessel growth has been showed in animal models than soluble VEGF⁷⁴. The 89% of VEGF was released gradually from the 200-600 nm PLGA nanoparticles within 4 days. Aortic ring angiogenesis assay was utilized to verify the bioactivity of encapsulated VEGF. In a mouse femoral artery ischemia model, VEGF-NP-treated limbs showed a significant increase in total vessel volume and thickness compared with soluble VEGF and saline conditions while no significant difference was found for vessel density or spacing. Interestingly, the unchanged anisotropy indicated that VEGF-NP treatment did not change the degree to which vessel were oriented in a specific direction. What's more, when taking VEGF dosing into account, VEGF-NPs were over an order of magnitude more potent than unencapsulated VEGF in increasing blood vessel volume in vivo⁷⁴.

Besides nano-scale PLGA particles, PLGA microspheres, the size of which is 5.1 ± 1.3 um, were also tested in the rat model of cardiac acute-reperfusion-ischemia⁷⁵. Unlike low-yield nano-scale encapsulation system, the yield of microencapsulation process was over 80% and 75% of VEGF was being released within 28 days. Treatment with VEGF-MP induced not only an increase in capillaries, but also in vessels of greater caliber (arterioles), suggesting that prolonged release of VEGF indirectly promotes arteriogenesis by stabilizing the vessels through

pericyte and/ or smooth muscles recruitment and proliferation. No hemangioma formation or leaking vessels were detected in the VEGF-MP group.

VEGF-MPs of even bigger size are also utilized in neo-vascularization of stroke cavity⁷⁶. Implantation of VEGF MPs of 50-100 um could stimulate angiogenesis, potentially providing a neovascularization of the denove tissue forming inside the lesion cavity and thus increase the survival and integration of transplanted cells. However, with the dosage of VEGF-MPs, the density of endothelial cells and newly forming blood vessels is much denser than found in normal tissue and it is unclear if this will eventually prune some unnecessary branches or if this could remain as a hyper-vascularized tissue.

Later, based on the previous study about rat model of acrdiac acute-reperfusion-ischemia, PEGylated-PLGA microparticles containing VEGF was fabricated to reduce particle phagocytosis in order to increase treatment efficacy⁷⁷. The bioactivity of VEGF was fully preserved. However, the *in vivo* result in the same model is unclear yet.

Other materials other than PLGA are also been developed for controlled growth factor delivery, such as hyaluronic acid/chitosan nanoparticles⁷⁸. However, in the dual-growth factor delivery system, even though PDGF-BB release was in sustained manner for 1 week, VEGF release was uncontrolled. What's more, *in vivo* study still needs to be done.

Hydrogel systems are also being considered as an option for sustained VEGF delivery. Particles consisting of VEGF co-lyophilized with trehalose was mixed with injectable, low viscosity poly(trimethylene carbonate) for both *in vivo* and *in vitro* experiment⁷⁹. However, the vessels generated were not stable and were reduced in number by 3 weeks, probably due to the unsustained and low concentration of VEGF release. Moreover, there was no distinctive difference in average blood vessel diameter in the tissue surrounding the VEGF implants and that surrounding RSA/trehalose only control.

In order to prolong the releasing cycle, nanoparticles together with hydrogel implanting system are being tried out. On the platform of PLGA microspheres, both collagen matrix⁸⁰ and fibrin gel^{81, 82} are being utilized for controlled release of VEGF, as well as commercialized Pluronic F127 hydrogel⁸³. The collagen scaffolds, which has constant VEGF releasing rate of 0.6ng/mg per day, induced a strong angiogenic response in a CAM assay leading to a 2.5 –fold increase in the number of newly formed blood vessels compared with that of collagen loaded with interspersed VEGF⁸⁰. For the nanoparticle-fibrin gel complex (NP-Fibrin), instead of loading a protein inside the PLGA particles, the authors utilized PLGA nanoparticles as a core that can be coated with heparin/pluronic layer, which in turn, interact with VEGF. This system is believed to maintain the bioefficacy of loaded protein better than other system by avoiding the o/w/o or s/o/w double emulsion method. The system was then loaded inside the fibrin get for sustained release⁸¹. In a rabbit ischemic hind limb model, VEGF-NP-Fibrin resulted in a significant increase in the recovered calf blood pressure, the angiographic score and the density of collaterals, as compared with VEGF-Fibrin or Fibrin⁸².

PLGA nanospheres are also and using different scaffolds as carrier for VEGF delivery. metal stent⁸⁴, collagen-coated polycaprolactone scaffolds⁸⁵, mesoporous hydroxyapatite⁸⁶, porous polyethylene implants⁸⁷, poly(lactide-co-glycolide) sintered microsphere scaffolds⁸⁸, Elastain/PLGA/PCL⁸⁹. Besides scaffolds, membrane is also utilized for sustained release of VEGF⁹⁰, heparin cross-linked dematerialized bone matrix⁹¹

Besides delivering VEGF by itself, all kinds of other growth factors are being used to co-deliver with VEGF for better outcomes. Such as dual delivery of VEGF and PDGF through membrane⁹², VEGF and FGF-2 co-delivery from allografts⁹³. Besides growth factors, other dual delivery system is also being developed, such as VEGF and CoQ(10)⁹⁴, sequential delivery of VEGF and TAT-HSP27⁹⁵, dual delivery of VEGF and MCP-1⁹⁶.

2.3.4 Mechanism study of VEGF induced angiogenesis

The binding of VEGF to VEGFR-2 induces receptor dimerization and autophosphorylation of specific intracellular tyrosine residues. In particular, Y1175 and Y1214 are major phosphorylation sites associated with the activation of the MAPK pathways in endothelial cells, activating intracellular signaling cascades critical for proliferation, migration and survival^{97, 98}. Matrix-bound VEGF has molecular distinction from soluble VEGF. The anchorage of VEGF to a PEG matrix not only elicits prolonged activation of VEGFR2, but also promotes reciprocal responses on β_1 integrin⁹⁹.

Cell signaling data is normally collected by exposing a confluent monolayer of cells to a soluble growth factor of interest. The interaction is studied over a course of a few minutes because that is the time scale for receptor activation and signal quenching. Recently, the field has noticed that matrix-bound growth factors lead to an altered profile of cell reaction. Although some groups have studied matrix bound growth factor signaling through plating cells directly on surfaces with the immobilized growth factor, this method does not allow cell-signaling studies on the order of minutes. In order to circumvent this limitation, others and we have devised alternative culturing and exposing platforms. One is based on exposing collagen bound VEGF to cells cultured on regular tissue culture plastic. VEGF is entrapped within the collagen gel. The loosely bound VEGF is allowed to release and the resulting gel containing matrix bound is gently added to the surface of the cells and allowed to incubate for minutes to one hour. From a signaling perspective, VEGF-matrix affinity affects the tyrosine phosphorylation profile and kinetics of VEGFR-2, along with downstream marker activation. In the soluble case, tyrosine residue Y1175 is preferentially phosphorylated, which leads to phospho-AKT activation⁶⁷. This pathway is involved in permeability and survival^{100, 101}. When VEGF is matrix bound, β_1 integrin

clusters with VEGFR-2 and phosphorylation of VEGFR2 at Y1214 is extended, as is phosphorylation of p38⁶⁷. These pathways are involved in cell migration¹⁰⁰.

Our laboratory also developed an approach to study covalently immobilized VEGF signaling with confluent cells. In our approach, growth factors are bound to a biomimetic SAM surface, while a confluent monolayer of cells is grown on a flexible PDMS material. Thus, the cells can be exposed to the immobilized growth factor by flipping the cell sheet on top of the modified surface. This exposure can be for several minutes and then analyzed.

2.4 Cellular response to nano-patterns

It has been known for decades that cells respond to topographical cues and signals from contact^{102, 103}. *In vivo*, cells interact with the extracellular matrix in nanometer scale. However, it is extremely difficult to study nanometer-scale signals *in vivo*. Thus, engineering an artificial surface that exhibits nano-sized features of biocues is therefore of great interest.

Distribution of biocues in nano-meter scale has been shown to greatly affect cellular outcomes. It has been shown that on 2D surface, integrins on cell surface only cluster and get activated when integrin ligands are 58 to 73nm apart¹⁰⁴. In 3D culture, distribution of nano-sized integrin ligands such as RGD peptides¹⁰⁵ were shown to affect cellular and therapeutic outcomes as well as nano-sized clusters of vascular endothelial growth factors (VEGF)¹⁰⁶. Thus, for tissue engineering purposes, it is extremely important to understand and precisely control cellular response to nano-scaled distribution of biocues, such as growth factors and integrin ligands.

While the majority of biocues distribution studies focusing on cell-substrate interactions, both on micro-scale features^{107, 108} and nano-scale integrin-ligand features^{109, 110}, studies of nano-scaled growth factor distribution are still missing. Unlike integrin activation study which can

be easily verified by immunofluorescence staining using a small area ($\sim\text{mm}^2$) nanopatterns, the study of nano-scaled growth factor distribution requires large ($\sim\text{cm}^2$) nanopatterns to enable protein and mRNA levels of quantification. For example, the use of Western blots, a mainstay for cell signaling studies, requires micrograms of protein, which can only be derived from thousands of cells growing on a surface of several square centimeters.

Lots of work have been done to create nano-sized features of biocues on artificial surfaces. However, most of the works proposed a small area ($\sim\text{mm}^2$) nanopatterns which makes the follow-up cellular studies really difficult due to the small regions and the small number of cells on the surface. Thus, to enable cell behavior studies at surfaces and to generate statistically relevant data such as cell attachment area and migration speed, nano-pattern were fabricated by electron-beam lithography (EBL)¹¹¹, sparse colloidal lithography¹¹²⁻¹¹⁴ and self-assembly-based approaches^{104, 115, 116}. However, the protein and mRNA expression remained un-studied on nano-patterned surfaces. This is mainly due to the difficulty of generating ultra-large surfaces, the lack of batch production capability and also the lack of consistency between samples.

VEGF is chosen as a growth factor template because it is known that presentation and distribution of growth factors can greatly change the molecular pathway and cellular outcomes. Specifically, for VEGF, studies have shown that covalently immobilized VEGF activates VEGFR2 pathway differently from soluble VEGF and electrostatically-bond VEGF⁹⁹. In particular, there was an upregulation in the phosphorylation of the p38 kinase, part of the signaling cascade associated with endothelial cell migration. This suggests that altering the way VEGF in which is presented is sufficient for modulating endothelial cell response. Other study also shows that clusters of covalently bound VEGF (cVc) result in enhanced EC sprout branching and total network length, compared to soluble VEGF. Thus, it was suggested that distribution of VEGF in nano-scale greatly impacts the cellular outcomes, yet no system was

available to test out this distribution effects from both mRNA expression and protein expression level.

Chapter 3

High-throughput quantification of nanoparticle degradation using computational microscopy and its application to drug delivery nanocapsules

3.1 Introduction

Here, we present computational holographic imaging based methods for monitoring nanoparticle degradation. These methods enable cost-effective and high-throughput quantification of nanoparticle degradation, using a very small volume of sample, e.g., < 15-20 nL (i.e., at least three orders of magnitude smaller than that is typically required for DLS).^{27, 28} We combine the advantages of lensfree holographic microscopy and self-assembled liquid nanolenses for rapid imaging and quantification of nanoparticle size over a large field-of-view of e.g., >20-30 mm².^{29,30,31} The nanoparticles under test are deposited on a coverslip followed by continuous exposure to polyethylene glycol (PEG) vapor, leading to the formation of nanolenses around nanoparticles, which amplify the optical signature of each nanoparticle, enabling its detection and size quantification (Figure 3.1). The sample is irradiated from the bottom using a programmable array of light-emitting-diodes (LEDs) and the resulting interference patterns (i.e., in-line holograms) formed due to the interference between the directly transmitted wave and the scattered wave from each nanoparticle-nanolens complex are captured using a complementary metal-oxide-semiconductor (CMOS) imager chip, placed at sub mm distance from the sample plane. A set of sub-pixel shifted holograms are recorded by turning the illumination LEDs on/off, which is then used to digitally synthesize a pixel super-resolved hologram that contains higher spatial frequencies of the sample. This pixel super-resolved hologram is reconstructed to yield phase and amplitude images of the nanoparticles on the substrate and the phase channel of the

sample image is used to quantify the size of the nanoparticles with a sizing accuracy of ± 11 nm³⁰.

The feasibility of this computational imaging method for monitoring nanoparticle degradation is demonstrated using vascular endothelial growth factor (VEGF) core protease-degradable nanoparticles (Figure 3.2). Growth factors are especially critical for regular cellular function and their incorporation within therapeutic materials has been a major focus of recent research³². In this work, for proof-of-concept we used VEGF, which has been described as the master regulator of angiogenesis³³. Protease degradable VEGF nanocapsules were synthesized through *in situ* radical polymerization of acrylate and acrylamide containing monomers and protease-sensitive peptide crosslinkers around the VEGF protein core.^{34,35} The final product is a protein-loaded nanoparticle containing 1-2 proteins per nanoparticle that is degradable by proteases that recognize the peptide crosslinker used (e.g., plasmin, trypsin). In this system one can control the release rate of the protein cargo by using the D enantiomer of the protease labile peptide. By changing the amino acids in the peptide crosslinker from L enantiomer to D enantiomer, the kinetics of enzymatic cleavage are decreased by 10-fold and thus the degradation rate of the nanocapsule is decreased. By mixing L- and D-enantiomer peptides in the same nanocapsule we can control the release rate of VEGF over time. However, the degradation process for these types of protein-core nanoparticles is hard to measure/monitor using existing techniques. First, due to the small batch production amount and costly ingredients, DLS is not an ideal testing method since the concentration of the nanoparticles is generally close to the lower detection limit of DLS instruments. Second, EM readout is feasible for dehydrated samples only and is unable to measure the size of hydrated nanoparticles. Third, biochemical assays such as Enzyme Linked Immuno-sorbent Assay (ELISA) is not accurate as the protein core gets degraded by proteases once exposed.

Therefore, this simultaneous degradation of the protein core and the polymer shell makes ELISA assays unreliable

3.2 Materials and methods

3.2.1 Materials used

Concentrated pure VEGF-A was a gift from Genentech. The peptide sequence Lys-Asn-Arg-Val-Lys of both L- and D- forms were purchased from China Tech Peptide Co. Ltd. Polyethylenimine (Linear 2.5KDa) and N-(3- aminopropyl) methacrylamide hydrochloride (APPMA) were purchased from Polysciences. Trypsin powder and aprotinin were purchased from Sigma-Aldrich. 0.25% Trypsin solution was purchased from Thermo Fisher Scientific.

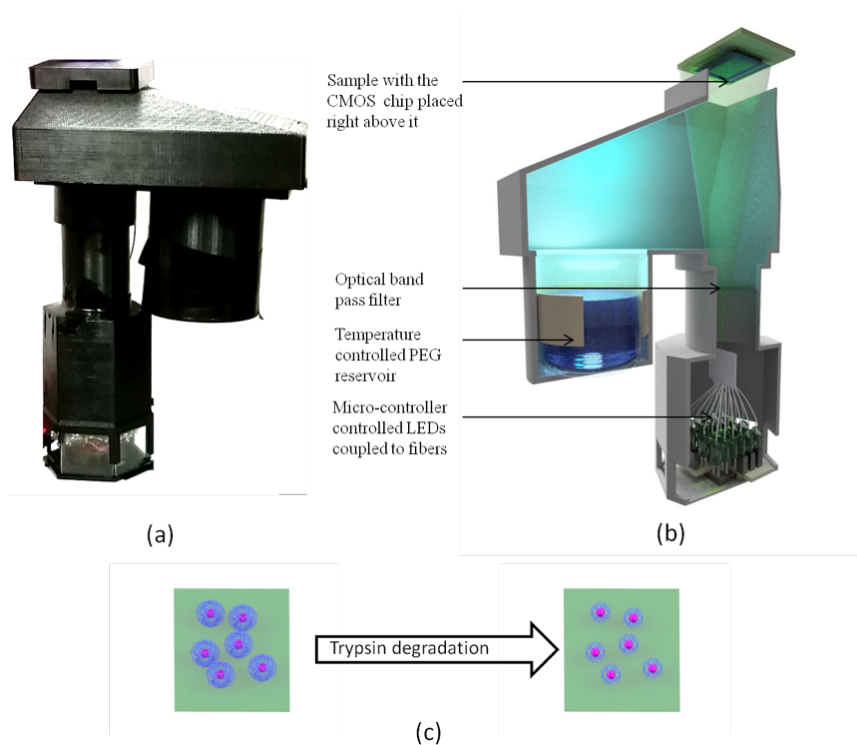


Figure 3.1(a) The photograph of the field portable holographic microscope. The device is about 25 cm in height and weighs less than 500 g.(b) The schematic of the physical hardware of the portable microscope. (c) Pictorial representation of the nanoparticle degradation by trypsin.

Trypsin amount was tested using Pierce™ Colorimetric Protease Assay Kit.

3.2.2 Field-Portable Holographic On-Chip Microscope

The schematic of the lensfree holographic on-chip microscope used in this work follows previous designs^{27,31,29,38} and is shown in Figure 3.1a,b. The field portable imaging device was constructed using custom-made 3D printed parts³⁰. This super resolution imaging system consists of a set of 20 LEDs (controlled by a micro-controller), each of which is coupled to an individual optical fiber⁴¹, an optical band pass filter with a central wavelength of 532 nm and a bandwidth of 10 nm, a mechanical adaptor for sample placement and a CMOS image sensor chip with USB readout (Imaging Development Systems UI-1492LE-M, 10 mega-pixels). Illumination of the sample was performed from the bottom using one LED at a time, and the resulting lensfree transmission holograms of the VEGF nanoparticles are recorded using a CMOS camera, which is placed close to the sample, at a distance of less than 1 mm. A custom developed LABVIEW program was used to control the entire imaging system. These sub-pixel shifted holograms are then used to generate a pixel super-resolved hologram, which is then reconstructed to obtain the phase and amplitude images of the nanoparticles^{37,38,39}.

A reservoir containing PEG-300, attached to the imaging system was utilized to form self assembled nanolenses over the nanoparticles. A resistive heater (Omega Engineering, KHLV-101/10), placed inside the reservoir, is used to heat the PEG-300 solution to the desired temperature (e.g., 90-105°C). A thermistor, interfaced to the main PC through a LabVIEW program, is used to monitor and control the temperature of the reservoir. We first acquire a set of raw holograms before the PEG condensation, which serves as a baseline to the evaporation process. Then, the temperature of the PEG was gradually increased to 95 °C, which results in PEG evaporation and condensation around the sample, leading to the formation (i.e., self-

assembly) of nanolenses around nanoparticles under test. During this deposition process we continuously acquire images to monitor and optimize the time-evolution of the nanolenses.

The image analysis was performed by dividing the field of view into smaller segments. The size distributions resulting from these individual segments were later combined to generate the final measurement dataset per sample. This analysis was performed over a subset of randomly selected FOVs, each $\sim 5 \text{ mm}^2$. The statistical analysis was performed using one-way analysis of variance (ANOVA) test and was followed up with the Tukey test⁴², which compares the mean of every time point, for a particular type of nanoparticle, with others and report the P value for each comparison. All our analysis was performed with a confidence interval set at 95 % ($P < 0.05$). These analyses were performed using GraphPad Prism software .⁴³

3.2.3 Vascular Endothelial Growth Factor (VEGF) nanocapsule synthesis

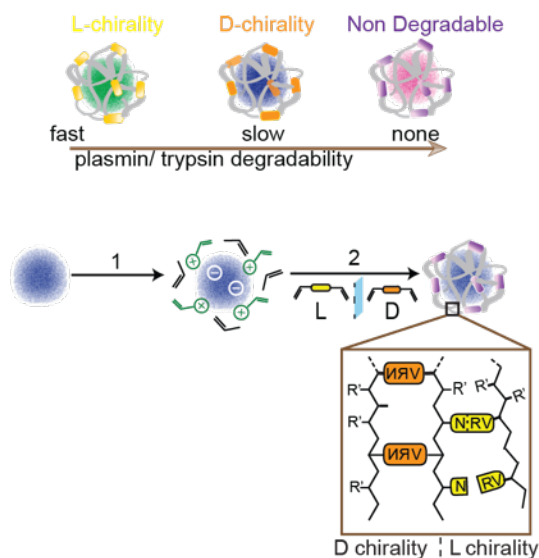


Figure 3.2 Schematic of the vascular endothelial growth factor (VEGF) core protease-degradable nanoparticles.

The nanocapsules were synthesized using *in situ* free-radical polymerization as previously published^{34,35}. Briefly, to synthesize n(VEGF), VEGF was diluted in a buffer solution of 10 mM sodium bicarbonate (pH = 8.55) at a final reaction concentration of 100 µg/ml. Acrylamide (AAM) and N-(3-aminopropyl)methacrylamide (APM) and crosslinkers (bisacrylated L/D-KNRVK, or methylene bisacrylamide) were subsequently added to the protein solution (at the molar ratio of VEGF:AAM:APM:crosslinker = 1:3000:3000:600). Three different crosslinkers (L, D or non-degradable) were used to synthesize VEGF nanoparticles with varying degrees of degradability (100%L, 100%D or non-degradable). These VEGF nanoparticles were later utilized for our degradation measurements reported in our Results section.

3.2.4 VEGF nanoparticle degradation in solution

VEGF nanocapsules (100 µg/ml) were mixed with equal volume of Trypsin (25 µg/ml, 100 times dilution from 0.25% Trypsin-EDTA in PBS) and incubated at 37°C for different time points (10, 15, 30 min or 1 day). The samples were subsequently quenched with aprotinin (10 µg/ml in DI water) and then placed on ice before imaging. Prior to imaging, the samples were further diluted by four orders of magnitude.

3.2.5 VEGF nanoparticles degradation on trypsin-coated coverslips

Trypsin coated coverslips were prepared by first plasma treating them, followed by 20 min of incubation with 2mg/ml PEI. After aspiration of PEI solution, fresh trypsin (5mg/ml in DI water) was added to the surface and incubated on ice for 20 min. The coverslips were dried and used shortly after this last step.

The nanoparticles were first deposited on the coverslip at the desired concentration. This was followed by the self-assembly of the nanolenses using PEG vapor, which was monitored

using the lensfree holographic on-chip microscope. After the nanolens deposition, the coverslips were placed on top of each other to form a sandwich structure and facilitate the interaction between the nanoparticle and trypsin, leading to the degradation process.

3.2.6 Measurement of trypsin amount on a surface

6mm-diameter PDMS wells were casted and placed on top of each coverslip. The wells were then subsequently treated with PEI and trypsin or PEI only as described above. Pierce™ Colorimetric Protease Assay Kit was then used to test the amount of trypsin on the coverslips.

3.2.7 DLS Measurements

DLS measurements were taken with ZetaSizer (Malvern Instruments) at 173° backscatter angle. VEGF nanocapsule samples of at least 20 μ L volume were measured in the precision cell made of quartz SUPRASIL® (Hellma).

3.3 Result and discussions

To measure the size of the VEGF nanoparticles, we first deposit them onto plasma treated hydrophilic coverslips. In order to maintain the hydration of the nanoparticles, they are coated with PEG prior to deposition since it has been previously shown that PEG can help improve retention of surface water³⁶. The nanoparticles are then exposed to PEG vapor that condensate to form droplets around them, acting as nanolenses. These self-assembled nanolenses significantly increase the signal to noise ratio of the nanoparticle holograms on the CMOS imager, enabling their lensfree detection and size quantification. During each experiment, the nanoparticles under test are continuously imaged, during and after the nanolens formation, using a custom-developed holographic on-chip microscope as shown in Figure 3.1a,b. A set of 20 sub-pixel shifted lensfree holograms is recorded using the CMOS imager by

digitally changing the illumination LED, and this information is used to digitally synthesize a super-resolved hologram, which effectively has sub-micron pixel size, undoing the effect of pixel induced spatial undersampling at the hologram plane^{37,38,39}. This super resolved hologram is then reconstructed to obtain phase and amplitude images of the nanoparticles on the substrate³⁸. The reconstructed phase information is utilized to determine the size of the VEGF nanoparticle, by using a linear regression model created with the measured phase information of nanoparticles with known size. This entire nanoparticle sizing process is performed using an automated segmentation algorithm running in MATLAB³⁰. The algorithm first reconstructs the super-resolved images at different heights (z_2) from the CMOS image sensor plane and initiates the particle counting process. Larger particles that have a higher peak phase value are counted first. These counted particles are then digitally removed from each super-resolved image (including their twin image artifact) by replacing their amplitude and phase by the background average. This process helps with the detection of smaller particles that would have otherwise been masked by the optical signatures of larger particles. These steps are repeated until all the VEGF nanoparticles are measured.

Based on our experiments and the above detailed size measurement process, the size distributions of VEGF nanoparticles, synthesized using different cross-linkers, L (*fast degradable*), D (*slowly degradable*) and non-degradable crosslinkers (e.g., bisacrylamide), were measured as shown in Figure 3.3. For these experiments, common methods of nanoparticle size quantification such as scanning/transmission electron microscopy or atomic force microscopy cannot be used for verification, as they are generally used on dry samples, unless special sample treatment is used. Therefore, we used DLS technique for independent validation of our results – see Supplementary Figure 3.4. Overall, we observed a slightly smaller particle size measured using DLS compared to our computational holography measurements. In order to verify the accuracy of the DLS instrument, we also measured the particle size of commercially

available polystyrene beads that were used for the initial calibration of the holographic imaging system and verified using electron microscopy measurements. In these measurements, we also consistently observed a lower particle size reading using DLS as shown in Supplementary Figure 3.5.

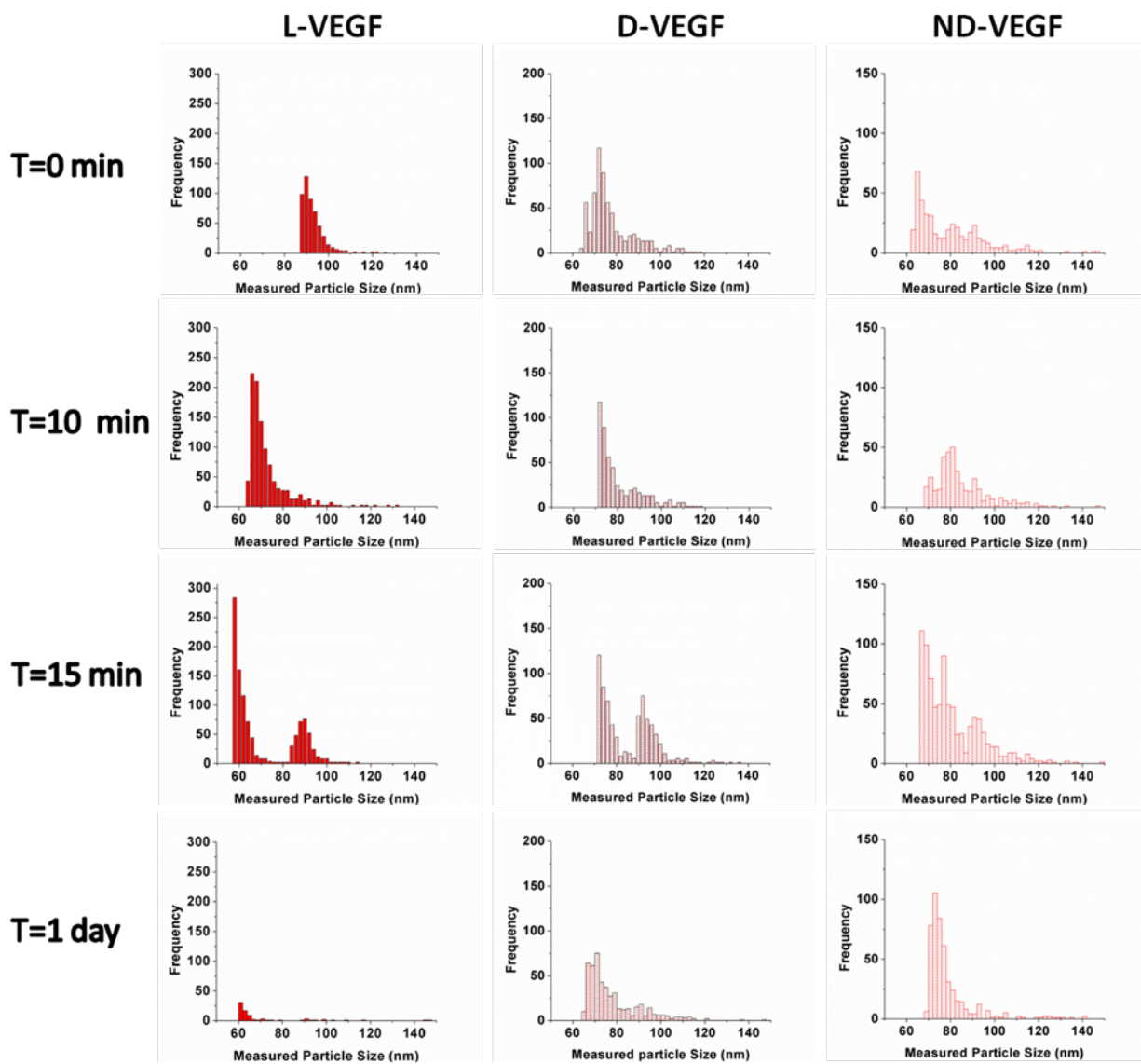


Figure 3.3 The mean particle size of the nanoparticles (L-VEGF, D-VEGF and ND-VEGF) measured by our computational holographic on-chip imaging platform following the degradation process at different time points.

After these initial experiments, to monitor as a function of time the degradation of VEGF nanoparticles with different degradability levels, the particles were incubated with trypsin at 37°C

for 0, 10, 15, 30 min and 1 day. Trypsin degradation was quenched with aprotinin. Samples were then preserved on ice and immediately used for size analysis. After the first 10 min of incubation, the L nanoparticles showed significant decrease in size, indicating a fast degradation process, as expected. In comparison to the L nanoparticles, both the D and non-degradable particles maintained stable size within the first 30 min. However, after 24 hours of incubation, D nanoparticles showed a noticeable decrease in size compared to earlier time points, indicating the progression of a slow degradation process. On the other hand, non-degradable nanoparticles maintained their size even after 1 day of incubation (Figure 3.3). These observations are consistent with the natural degradation of L and D enantiomer. In nature, only L-amino acids are manufactured in cells and incorporate into proteins, and D-amino acids are found to be strongly resistant to proteolytic degradation⁴⁰.

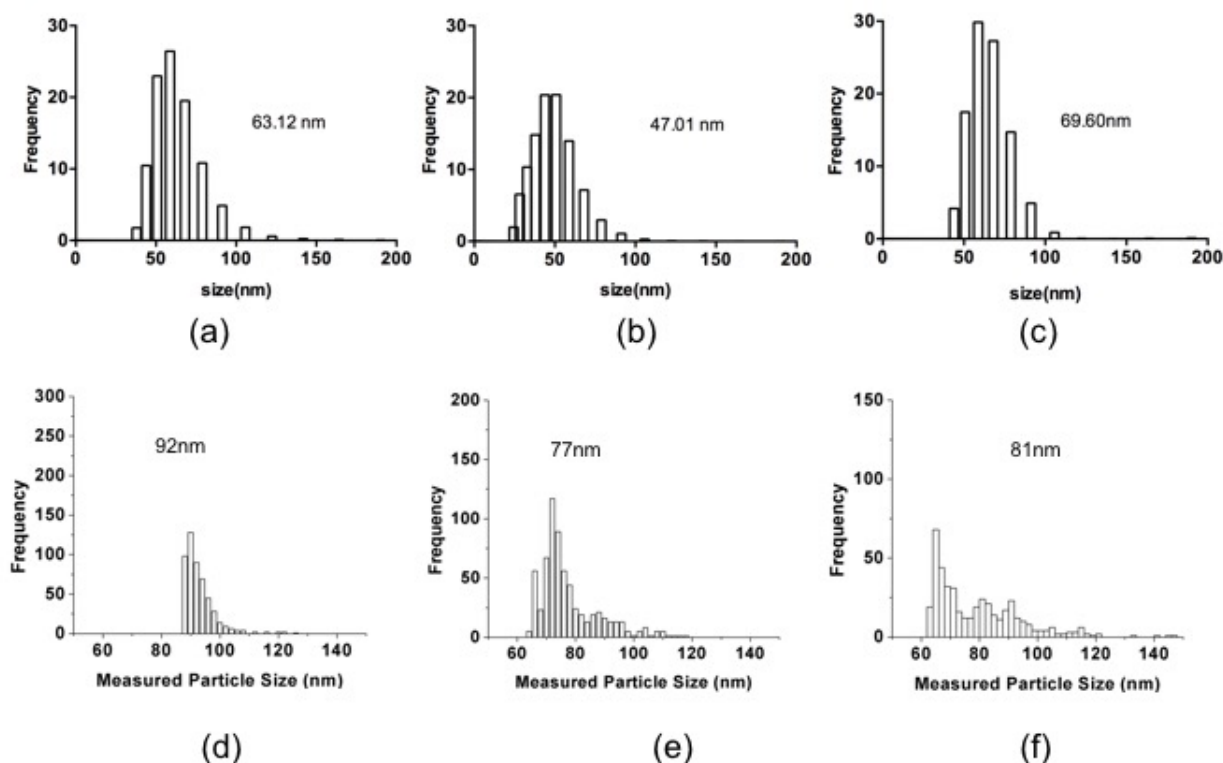


Figure 3.4 Comparison between the size distribution of the nanoparticles between Dynamic Light Scattering (DLS) (a-c) and our computational imaging system. (d-f). The nanoparticles are as follows: (a), (d): L-VEGF; (b), (e): D-VEGF and (c), (f): Nondegradable VEGF.

Quite interestingly, during our experiments a significant second peak was observed around a particle size of 90-110 nm for some of the particles undergoing the degradation process. We hypothesize that this peak is due to trypsin-based aggregation of the particles or the monomers. In order to test this hypothesis, we utilized a DLS measurement to study this aggregation effect. Briefly, a solution containing VEGF, monomers, and crosslinkers was directly incubated with trypsin and monitoring of their mean size was performed by DLS. As illustrated in Figure 3.6, a clear aggregation process was also observed using DLS, with a peak in size appearing at around 20-40 min. This shows that trypsin aggregates with the cleaved monomers and crosslinkers during the incubation process and this leads to the occurrence of the second peak in our particle size distribution measurements (Figure 3.3). The average size distribution measured at different time points for each of the nanoparticles is also summarized in Figure 3.7, where this aggregation related second peak was not included in the average particle size.

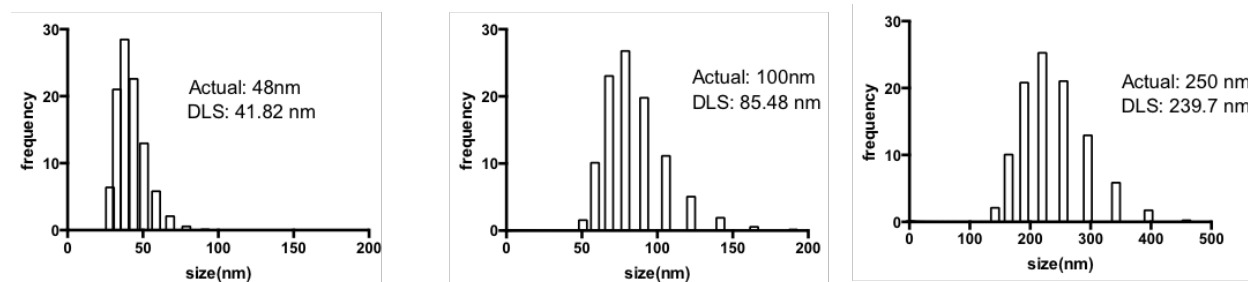


Figure 3.5 Measurement of particle size distribution of commercialized polystyrene beads using DLS. The actual particle size and the measured particle size are mentioned in the figure.

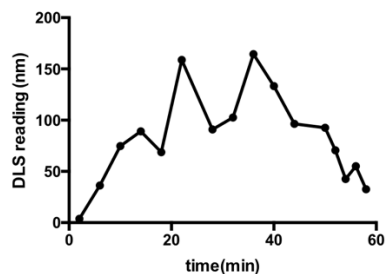


Figure 3.6 DLS measurement of size distribution when trypsin is directly added to nonomer solution. This shows that trypsin induces aggregation of the monomers.

Next, we created a sandwich assay that enabled us to visualize and quantify enzyme-triggered degradation of nanoparticles in real time, i.e., continuously. After the nanolens deposition on VEGF nanoparticles under test, we placed a trypsin coated coverslip to create a sandwich structure, as shown in Figure 3.8. The rationale for this sandwich structure is that upon degradation of VEGF nanoparticles, the nanolens around each particle will be destabilized leading to a loss in the intensity of its lensfree hologram. Indeed, we observed a significant reduction in the intensity of the raw particle holograms for degradable nanoparticles (L enantiomer) as shown in Figure 3.9. This reduction in intensity was observed immediately after placing the trypsin coated coverslip on the sample and the hologram signal intensity became extremely faint within 10 to 15 minutes, quickly approaching to the noise floor of the sensor, indicating the degradation of the nanoparticles. Our control experiments with trypsin coated coverslips and non-degradable particles as well as polyethyleneimine (PEI) coated coverslips with degradable nanoparticles, did not show a significant change in their particle hologram intensity, as shown in Figure 3.10. It should be emphasized that this nanoparticle degradation was observed only when a high concentration of trypsin was used, e.g., $\sim 40\text{-}50$ ng per mm^2 . The need for this high concentration may be due to the limited contact surface between the nanoparticles under test and the trypsin coated surface area.

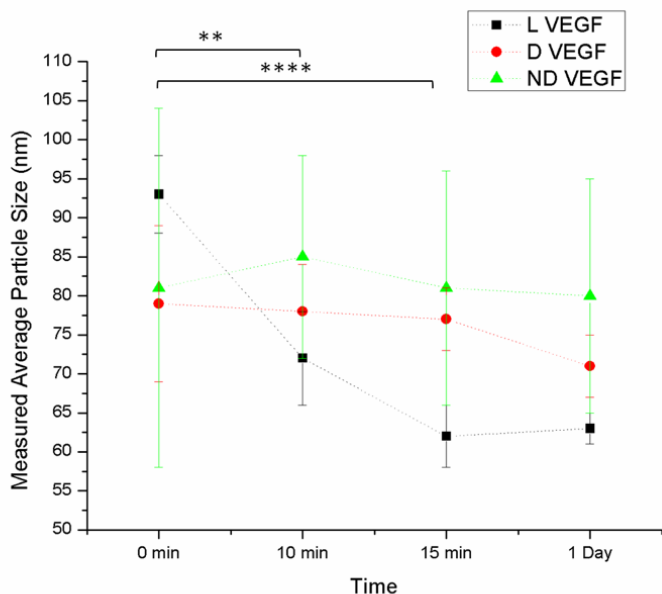
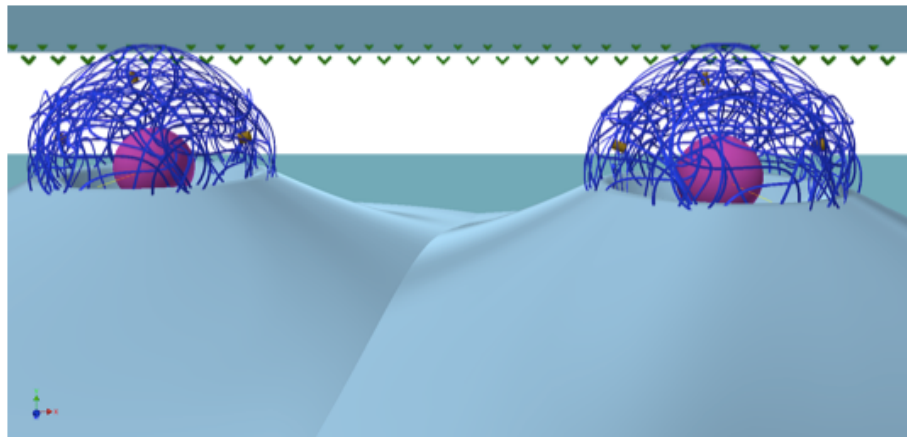


Figure 3.7 Average size of the nanoparticles following the degradation process, measured by our computational holographic on-chip imaging platform. The analysis was performed by averaging the sizes of over 350 nanoparticles, for all the samples, except the 1-day L-VEGF sample, which had lower recovery, with ~80 particles. Error bars denote the standard deviation. The P values are denoted as **: $P < 0.0015$; ****: $P < 0.0001$.



- ✓ Trypsin
- Vascular endothelial growth factor (VEGF) core with protease-degradable polymer shell

Figure 3.8 Schematic of the sandwich structure, depicting the interaction between each nanoparticle-nanolens complex and the trypsin on the surface of a substrate.

Our first method of sampling a subset of nanoparticles undergoing degradation, and computationally sizing them subsequently is more general compared to the second approach that we presented, and can be used for all types of nanoparticles with any degradation

mechanism. This method mainly focuses on the characterization of nanoparticles post-degradation. It gives a clear view of the final outcome of degradation process, however, no real-time visualization is possible. Unlike the first method, our second method starts monitoring the nanoparticles before any degradation happens and facilitates real-time visualization of the entire process. Also, this unique sandwich assay requires an even smaller amount of sample volume compared to the first method. However, this 2D sandwich based method can only be applicable to a select group of nanoparticles, which can degrade using e.g., light, magnetic field etc. or antagonists that can be introduced by a coverslip/substrate.

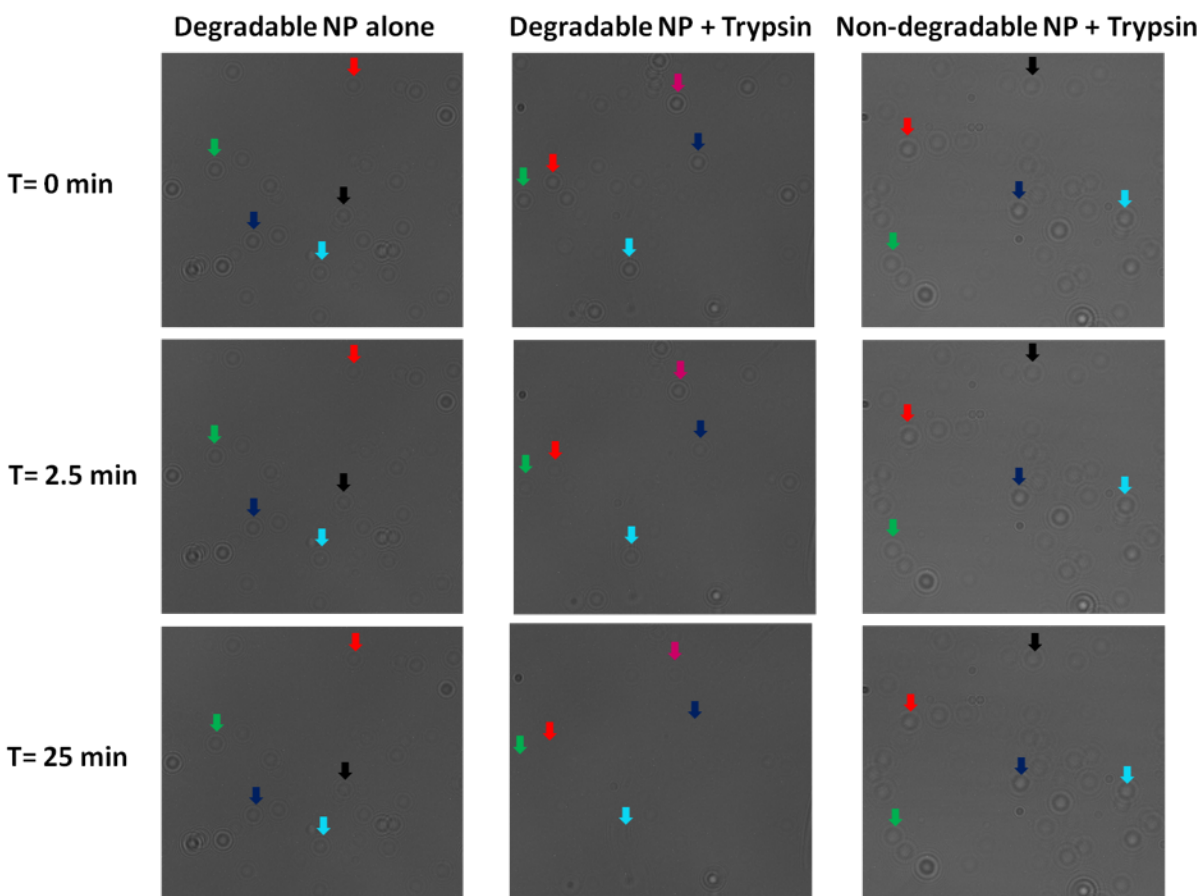


Figure 3.9 Monitoring the changes in the intensity of the lensfree holograms of the L (fast-degradable) VEGF nanoparticle/nanolens complexes following their contact with the trypsin-coated surface in the sandwich structure. The arrows indicate the selected nanoparticles used for the subsequent analysis reported in Figure 3.10.

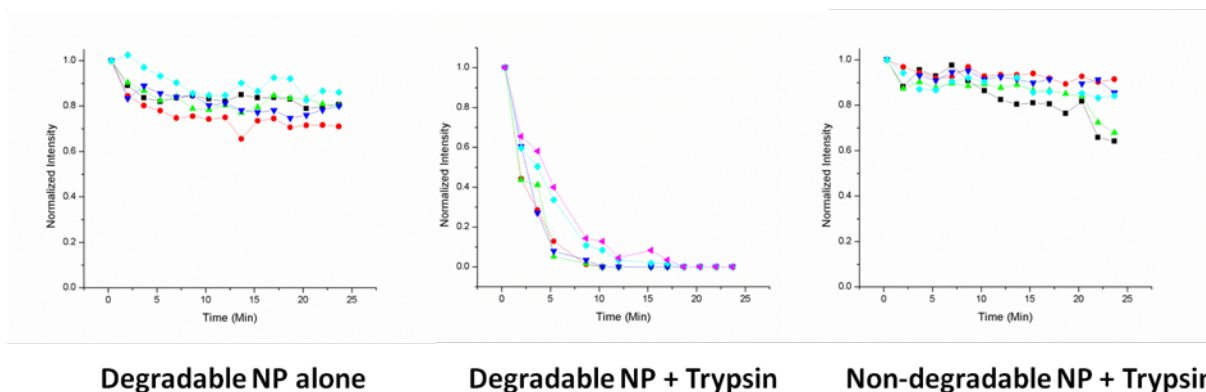


Figure 3.10 Temporal changes in the intensity of the lensfree holograms, each corresponding to individual nanoparticles, after their interaction with the trypsin coated surface. The color represents the particles selected in Figure 3.9.

3.4 Conclusions

By using our computation holographic microscopy based method, these obstacles are overcome. We used two different testing methods to monitor and quantify the degradation of VEGF nanoparticles. The first method involves sizing the nanoparticles by discretely sampling the synthesis solution at different time points after addition of proteases. A second method using a sandwich assay was developed to monitor the live degradation process in a continuous manner by placing a trypsin coated coverslip on the nanoparticle/nanolens complex, also imaged by our computational holographic microscope. These computational imaging experiments were performed on both degradable and non-degradable nanoparticles, showing a drastic change to the polymer matrix bound together by degradable crosslinkers compared to the nondegradable ones. Overall, this computational holographic imaging based nanoparticle monitoring platform provides a much needed, cost effective and high-throughput method to quantify the degradation process of any type of nanoparticle using very small amounts of sample volume.

Chapter 4

Integrin stimulation from bioengineered scaffolds dictates vascular patterning and reduces VEGF induced vascular permeability after stroke

4.1 Introduction

The design of therapeutic angiogenic materials to treat cardiovascular diseases, such as deficient blood supply to the heart, limbs, and brain, has primarily been driven by the delivery of angiogenic factors within a scaffold. Optimization of these materials has been focused dominantly on controlling angiogenic factor release or presentation and modulating bulk physical properties. Although adhesive ligands that promote integrin binding are generally incorporated within therapeutic angiogenic materials, the subsequent cell-material interaction has not been explored as an angiogenic signal.

This present work shows for the first time that specific integrin activation from a biomaterial can be harnessed to direct vascular patterning *in vitro* and *in vivo* leading to enhanced reperfusion of the brain after stroke.

Integrin binding is a fundamental design parameter for engineering matrices for tissue repair and regeneration. The incorporation of integrin binding molecules within engineered matrices ranges from peptides such as RGD¹¹⁷, to protein fragments¹¹⁸, and natural proteins¹¹⁹, with the primary purpose to promote cell spreading and migration within these matrices. However, integrin binding ligands are often overlooked as bioactive cues in capable of dictating morphogenesis and guiding tissue repair. Our work shows for the first time that integrin stimulation from engineered matrices is a morphogenic signal that can be harnessed to

generate either a normal vasculature or a diseased vasculature depending on the integrin being engaged.

Immediately following vascular injury, wounds are not filled with collagen but rather provisional matrices comprised of fibrin and fibronectin. Fibronectin is the major ECM constituent in the early, pre-vascularized wound. In our study, recombinant fibronectin fragments of the 9th type III repeat (Fn III9) and 10th type III repeat (Fn III10) were designed to preferentially bind $\alpha3/\alpha5\beta1$ or $\alpha\nu\beta3$ integrin respectively. To achieve $\alpha3/\alpha5\beta1$ specificity, the thermodynamic stability of Fn III9 was increased through a leucine to proline point mutation at position 1408. This mutation has been previously shown to stabilize the integrin-binding domain of fibronectin, i.e. Fn III9-10, and enhance its binding selectivity to synergy-dependent $\beta1$ integrins, including both $\alpha5\beta1$ and $\alpha3\beta1$ ^{35, 40, 120}. To achieve $\alpha\nu\beta3$ integrin specificity, four (4) glycine residues were then inserted into the linker region between Fn III9 and Fn III10. The 4xGly insertion both physically separates the synergy (PHSRN) and RGD sites located on Fn III9 and Fn III10, respectively, and introduces torsional flexibility between the two domains, resulting in a complete disruption of $\alpha3/\alpha5\beta1$ integrin binding and promoting a $\alpha\nu\beta3$ integrin preference. Though both recombinant fragments can theoretically bind $\alpha\nu\beta3$ integrin via the RGD sequence, we and others consistently observe a preference of the stabilized mutant to bind synergy-dependent integrins, like $\alpha5\beta1$ integrin in cell material interactions^{42, 121}. In this manuscript, we called the Leu-Pro mutated, or stabilized, fragment 9*10 and the 4xGly insertion mutated fragment 9(4G)10. For ease of immobilization onto surfaces and incorporation into natural and synthetic hydrogel biomaterials both fragments were produced with an N-terminal cysteine residue to allow Michael type addition modifications and a factor XIIIa substrate sequence, consisting of residues 1–8 of the protein alpha2 plasmin inhibitor ($\alpha2PI_{1-8}$, NQEQVSPL)¹²² to allow enzymatic conjugation.

4.2 Materials and methods

4.2.1 Recombinant fibronectin fragments

Recombinant fibronectin fragments of the 9th type III repeat (Fn III9) and 10th type III repeat (Fn III10) were designed to preferentially bind $\alpha3/\alpha5\beta1$ or $\alpha\nu\beta3$ integrin respectively. To achieve $\alpha3/\alpha5\beta1$ specificity, the thermodynamic stability of Fn III9 was increased through a leucine to proline point mutation at position 1408. This mutation has been previously shown to stabilize the integrin-binding domain of fibronectin, i.e. Fn III9-10, and enhance its binding selectivity to synergy-dependent $\beta1$ integrins, including both $\alpha5\beta1$ and $\alpha3\beta1$ ^{35, 40, 120}. To achieve $\alpha\nu\beta3$ integrin specificity, four (4) glycine residues were then inserted into the linker region between Fn III9 and Fn III10. The 4xGly insertion both physically separates the synergy (PHSRN) and RGD sites located on Fn III9 and Fn III10, respectively, and introduces torsional flexibility between the two domains, resulting in a complete disruption of $\alpha3/\alpha5\beta1$ integrin binding and promoting a $\alpha\nu\beta3$ integrin preference. Though both recombinant fragments can theoretically bind $\alpha\nu\beta3$ integrin via the RGD sequence, we and others consistently observe a preference of the stabilized mutant to bind synergy-dependent integrins, like $\alpha5\beta1$ integrin in cell material interactions^{42, 121}. In this manuscript, we called the Leu-Pro mutated, or stabilized, fragment 9*10 and the 4xGly insertion mutated fragment 9(4G)10. For ease of immobilization onto surfaces and incorporation into natural and synthetic hydrogel biomaterials both fragments were produced with an N-terminal cysteine residue to allow Michael type addition modifications and a factor XIIIa substrate sequence, consisting of residues 1–8 of the protein alpha2 plasmin inhibitor ($\alpha_2\text{PI}_{1-8}$, NQEQVSPL)¹²² to allow enzymatic conjugation.

The expression system for these recombinant Fn fragments has been optimized from prior publications (Markowski *et al.*) to create a high throughput production process¹²¹. The expression vectors were transformed into MDS™42 LowMut ΔrecA (6262) chemically competent cells and individual clones were picked for successive expansion and increased

protein yields. Transformed cells were grown in 2xYT media with Kanamycin (50 µg/mL) and protein production was induced by addition of 1.5mM IPTG. Incubation at 37°C with shaking for approximately 16 hours allows maximal protein production. Cultures were then centrifuged and lysed via sonication and freeze-thaw cycling. Recombinant Fn9-10-tdtomato-10 His were purified on a HisTrap nickel column (AKTSA Start, GE Healthcare) via affinity chromatography. Tdtomato and 10-His tag were removed by utilizing the thrombin cleavage site and bovine thrombin (Sigma-Aldrich) to separate the fragment and the tdtomato fusion protein. A Benzamidine column bound the free bovine thrombin and the His tag allows collection of C-terminal tdtomato in the HisTrap again and the Fn fragments (Fn9*10 or Fn9(4G)10) were released. The purity of Fn9-10 protein fragments was then analyzed by SDS-PAGE as mentioned in previous works^{35, 42}.

4.2.2 Immobilization of Fn9*10 or Fn9(4G)10 on homogenous gold surface

Standard laboratory microscope glass slides were sequentially washed with acetone, isopropyl alcohol and methanol before gold deposition in e-beam evaporator. Deposition parameter: 5nm titanium at 0.3 Å/s deposition rate, followed by 30 nm gold at 0.5 Å/s deposition rate. Gold slides were then functionalized with 1% HS-C11-EG6-NH2(11-Mercaptoundecyl)hexa(ethylene glycol) amine, ProChimia Surfaces) and 99% HS-C11-EG4-OH (11-Mercaptoundecyl)tetra(ethylene glycol), Sigma-Aldrich). A total of 100mg of EMCH (N-[ε-Maleimidocaproic acid]hydrazide, Fisher Scientific, PI-22106) was first dissolved in anhydrous DMSO(Dimethyl sulfoxide) to make 50Mm stock. 5 mg/ml Heparin (Alfa Aesar, A16198) solution in 100mM 2-(N-morpholino)ethanesulfonic acid (MES) pH6 buffer was then mixed with EMCH, NHS (N-Hydroxysuccinimide ,Sigma-Aldrich) and EDC (1-(3-Dimethylaminopropyl)-3-ethylcarbodiimide hydrochloride, Fisher Scientific) sequentially. Mole ratio of COOH in heparin/

EMCH/ NHS/EDC=1:1:1:10. The reaction continued for 6 hours with gentle shaking followed by dialysis. The dialyzed samples were then lyophilized and sent for NMR for modification verification. The modified heparin was then conjugated to SAMs (99% EG-OH, 1% EG-NH₂) formed on gold slides via EDC/NHS method as previously stated. Either Fn9*10 or Fn9(4G)10 (1000ng/slide, 53.3ng/ cm²) was incubated with the modified heparin-coated surfaces overnight at 4 °C, followed by three PBS washes.

4.2.3 Enzyme-linked immunosorbent assay (ELISA) on Fn9*10 or Fn9(4G)10 immobilized gold surface

Modified gold surfaces was Argon-dried and then assembled together with PDMS sheet that has two 8mm circular wells followed by 60ul/well 0.1%BSA-PBS as blocking buffer for 1 hour at room temperature. After aspiration, 60ul/well of Anti-Fibronectin primary antibody (1:2000 dilution in blocking buffer, ab299, Abcam) was added for 2 hours at room temperature. After 3 washes using 0.05% Tween-20+PBS (washing buffer), 60ul/well of streptavidin-HRP (1:5000 dilution in blocking buffer, #DY998, R&D Systems) was added for 1hour at room temperature. After 3 washes, 60ul/well of TMB substrate (#7004L, Cell signaling) was added, incubated for 8 min in dark and then transferred to 96-well plates containing 1M H₂SO₄. The absorbance was measured at 450nm and normalized against absorbance at 550nm.

4.2.4 Cell proliferation assay

Slides immobilized with Fn9*10 or Fn9(4G)10 were washed twice with sterile PBS and then blew dry in cell culture hood for well assembly with 8-wells ibidi sticky-bottom device (ibidi, #80828). A total of 5000 HUVECs in EGM-2 stripped off fibronectin were seeded in each well with or without 2ng/ml of VEGF and the cell number was assayed after 48 hours using Cyquant assay. A minimum of n=8 per condition was used in this experiment.

4.2.5 Cell migration assay

Slides were then washed twice with sterile PBS and then blew dry in cell culture hood for well assembly with PDMS sheets containing two 8mm holes. 5000 HUVECs pre-stained with SP-DilC18(3) lipophilic red fluorescence dye (Life Technologies) were seeded in each PDMS well on surface in EGM-2 w/o Fibronectin/VEGF medium and allowed for cell attachment for 3 hours in cell incubator. The slides were then transferred into incubation system of Zeiss LSM 780 confocal for 10x phase time-lapse tracking. Images were taken at 4 different locations over time span of 7 hours with 15 min interval. A MATLAB program was then developed to track the strongest lipid signal. Basically, after circling out manually the target cells, the program tracks the brightest lipid stain in the area to create the cell migration path and calculated cell migration distance. A minimum of n=64 in each condition was used to quantify.

4.2.62D Immunofluorescence Staining on Fragments Coated Cell Culture Plates

Glass-bottom 24-well plates were first incubated with 500 μ l of 2 μ M Fn9*10 or Fn9(4G)10 per well overnight. Wells were incubated with 5% BSA-PBS for 1 hour at room temperature before the seeding of HUVECs which were pre-starved in EBM-2 media for 6 hours. A total of 50000 HUVECs in EGM-2 stripped off fibronectin were seeded in each well without VEGF and fixed after 18 hrs. Cell samples were first fixed in 1% PFA for 20 min, washed twice with PBS for 5 min. Samples were incubated at room temperature for 30min in blocking buffer: PBS+ 5% Normal Goat Serum. Primary antibodies were prepared as follows in blocking buffer: Mouse anti- α v β 3 (clone LM609, Millipore; MAB1976) – 1:100, Mouse anti- α 5 β 1(clone HA5, Millipore; MAB1999) – 1:100. Samples were incubated with primary antibodies overnight at 4°C, followed by Secondary antibodies (1:500) and 2 μ g/ml DAPI for 1 hour in the dark at room temperature. Imaging was performed using a Nikon C2 confocal.

4.2.72D Immunofluorescence Staining on Fragments immobilized Gold Surfaces

Slides immobilized with Fn9*10 or Fn9(4G)10 were washed twice with sterile PBS and then blew dry in cell culture hood for well assembly with 12-well customized white Teflon wells. A total of 5000 HUVECs in EGM-2 stripped off fibronectin were seeded in each well with or without 2ng/ml of VEGF and fixed after 24 hrs. Cell samples were first fixed in 4% PFA for 15 min, washed twice with PBS for 5 min each before incubating with PBS+0.1% Triton for 3 min. After washing the samples again with PBS, samples were incubated at room temperature for 30min in blocking buffer: PBS+ 2% Normal Goat Serum. Primary antibodies were prepared as follows in blocking buffer: Rabbit anti-mouse and human VEGFR-2 (Cell Signaling Technology; #2479L) – 1:200, Mouse anti-human PECAM-1 (R&D; #BBA7) – 1:200, Monoclonal mouse anti-Vinculin antibody (Sigma-Aldrich, #V9131) – 1:400, Mouse anti- $\alpha\text{v}\beta\text{3}$ antibody (EMD Millipore, MAB1976) – 1:200. Samples were incubated with primary antibodies overnight at 4°C, followed by Secondary antibodies (1:500) and 2 $\mu\text{g}/\text{ml}$ DAPI for 1 hour in the dark at room temperature. Imaging was performed using a Zeiss confocal and images were analyzed using Image J.

4.2.8Sprouting Assay with blank, full length Fibronectin, Fn9*10 or Fn9(4G)10 fibrin gels

Fibrin bead assay HUVEC were mixed with dextran-coated Cytodex 3 microcarriers (Amersham Pharmacia Biotech) at a concentration of 400 HUVEC per bead in 1 ml of EGM-2 medium (Clonetics). Beads with cells were shaken gently every 20 min for 4h at 37°C and 5% CO₂. After incubating, beads with cells were transferred to a 25-cm² tissue culture flask (BD Biosciences) and left for 12–16 h in 5 ml of EGM-2 at 37°C and 5% CO₂. The following day, beads with cells were collected and washed three times with 1 ml of EGM-2 w/o Fibronectin and resuspended at a concentration of 500 beads/ml in 2 mg/ml fibrinogen (Fib1 or Fib3), 1 U /ml factor XIII and 0.04 U/ml aprotinin at a pH of 7.4 with or without 2 μM Fn9*10, 2 μM Fn9(4G)10,

0.54 μM full length Fibronectin (Millipore, FC010). A total of 250 μl of this fibrinogen/bead solution was added to 0.16 units of thrombin in one well of glass-bottom 24-well plates. Fibrinogen/bead solution was allowed to clot for 5 min at room temperature and then at 37°C and 5% CO_2 for 20 min. EGM-2 w/o Fibronectin was added to each well and equilibrated with the fibrin clot for 30 min at 37°C and 5% CO_2 . Medium was removed from the well and replaced with 1 ml of fresh EGM-2 w/o Fibronectin. A total of 20,000 HDFs were plated on top of the clot and the medium was changed every other day. Bead assays were monitored for 7 days. At least three independent gels were evaluated per condition per sprouting experiment. Quantifications of at least 5 beads from each gel were analyzed (only sprouts with a length of one bead diameter were included). Since beads were seeded sparsely (25-40 beads within 250 μl of total gel volume) and each bead was surrounded by its own microenvironment, we consider each bead as an independent sprouting sample. Additionally, sprouting data were analyzed across experiments performed in different days taking each day as one biological replicate. The trends from both types of analyses are the same.

4.2.9 Quantification of Vessels and Tip Cells in Sprouting Assay

High-resolution images of beads were captured on a Nikon Confocal C2 with a 10X objective. The advantage of taking images at this magnification is the depth of field which includes all sprouts in focus. Images are then analyzed in NIH ImageJ. The number of sprouts per bead, the number of branches per bead, length of total network per bead and branch cluster per bead were counted. Only sprouts with a length of one bead diameter were included. A minimum of $n=15$ was used for each condition from 3 independent wells.

Tip cells images were captured on a Nikon Confocal C2 with a 60X objective. Images are then analyzed in NIH ImageJ. The number of filopodia per tip were counted. A minimum of $n=19$ was used for each condition from 3 independent wells.

4.2.10 Sprouting Assay with RGD Presence

Sprouting assay was performed as previously described in Fib3 fibrin gels with 200, 500 or 1000 μM of $\alpha_2\text{PI}_{1-8}$ -RGD (H-NQEQVSPLRGDSPG-NH₂, GenScript).

4.2.11 Anastomosis Sprouting Assay with Fn9*10 and Fn9(4G)10

EGFP-HUVEC were mixed with dextran-coated Cytodex 3 microcarriers at a concentration of 400 HUVEC per bead in 1 ml of EGM-2 medium. Beads with cells were shaken gently every 20 min for 4h at 37°C and 5% CO₂. Beads with cells were then transferred to a 25-cm² tissue culture flask and left for 12–16 h in 5 ml of EGM-2 at 37°C and 5% CO₂. The following day, beads with cells were washed three times with 1 ml of EGM-2 w/o Fibronectin and resuspended at a concentration of 500 beads/ml in 2 mg/ml Fib3 fibrinogen, 1 U /ml factor XIII and 0.04 U/ml aprotinin, 80,000 cells/ml HDF at a pH of 7.4 with 2 μM of Fn9*10 or Fn9(4G)10. 250 μl of this fibrinogen/bead solution was added to 0.16 units of thrombin in one well of glass-bottom 24-well plates. Fibrinogen/ HUVEC bead/ HDF cells solution was allowed to clot for 5 min at room temperature and then at 37°C and 5% CO₂ for 20 min. EGM-2 w/o Fibronectin was added to each well and equilibrated with the fibrin clot for 30 min at 37°C and 5% CO₂. Medium was removed from the well and replaced with 1 ml of fresh EGM-2 w/o Fibronectin and later was changed every other day. Bead assays were monitored for 11 days. Three independent wells were evaluated per condition. Tip-tip contact distribution from each condition were analyzed within the 170 μm of working distance of 60x objective.

4.2.12 Flow Cytometry

HUVEC cells were harvested from 25 cm² cell culture flask using 1ml of 2mg/ml Collagenase (Thermo Fisher Scientific, ICN1951091) for incubation of 30min at 37°C. The reaction was later quenched with 1mM EDTA in PBS for 5min before centrifugation at 200g for 5min. 60,000 cells per well were then added to 96-well round-bottom plate (Corning, 3365) which already contained 100 µl of serial dilution of P3G8 (Developmental Studies Hybridoma Bank) starting at concentration of 1µg/ml. The plate was then incubated in cell incubator for 30min before centrifuged at 1200rpm for 2min. 200 µl of FACS buffer (2% FBS in PBS) per well was then added to resuspend the cells pellet. This washing step was repeated twice before Goat-anti-Mouse AF488 was diluted in 1:4000 and added into the wells. The secondary antibody incubation was done in dark outside of incubator for 20min. Cells were then centrifuged and washed 3 times like described above. The final cell pellets were resuspended in FACS buffer. Analysis was performed using a MACS Quant VYB and the data was analyzed using FLOWJO. Triplicates were done for each condition with at least 9700 events/sample. The data was gated such that the negative control had 0.5% positive events.

4.2.13 Integrin Blocking Sprouting Assay

Sprouting assays were performed as previously described.

For Fn9*10 gels, HUVEC beads were suspended at a concentration of 500 beads/ml in 2 mg/ml fibrinogen (Fib1 or Fib3), 1 U /ml factor XIII, 0.04 U/ml aprotinin and 2 µM (high dosage) or 0.267 µM (low dosage) Fn9*10 at a pH of 7.4 with or without 5µg/ml of β1 integrin blocking antibody (AIIB2, Developmental Studies Hybridoma Bank) or α5 integrin blocking antibody (BIIG2, Developmental Studies Hybridoma Bank). The blocking antibody (5µg/ml) in fresh fibronectin-free EGM-2 medium was replenished every day.

For Fn9(4G)10 gels, HUVEC beads were suspended at a concentration of 500 beads/ml in 2 mg/ml fibrinogen (Fib1 or Fib3), 1 U /ml factor XIII, 0.04 U/ml aprotinin and 2 μ M (high dosage) or 0.239 μ M (low dosage) Fn9(4G)10 at a pH of 7.4 with or without 5 μ g/ml of β 3 integrin blocking antibody (9H5, Developmental Studies Hybridoma Bank) or α v integrin blocking antibody (P3G8, Developmental Studies Hybridoma Bank). The blocking antibody (5 μ g/ml) in fresh fibronectin-free EGM-2 medium was replenished every day.

4.2.14 VE-cadherin Staining on 3D Integrin-Blocking Assay

Gel samples were first fixed in 1% PFA for 15 min, blocked for 2 hours at room temperature in a blocking buffer of PBS+ 0.05% Tween-20 + 5% Normal Goat Serum. Samples were then incubated in a primary antibody directed against VE Cadherin (Rabbit, Abcam; ab33168, 1:200) overnight at 4°C, followed by a secondary antibody (1:500) and 2 μ g/ml DAPI for 1 hour. Imaging was performed using a Nikon C2 confocal and images were analyzed using Image J.

4.2.15 VE-cadherin Staining on 2D Fragments-Coated Surfaces

A total of 500 μ l of 2 μ M Fn9*10 or Fn9(4G)10 in PBS buffer was added into sterile 24 well glass-bottom plates (MatTek Corporation) for 1 hour in cell incubator, followed by 0.1% heat-deactivated sterile BSA-PBS buffer for 1 hour. HUVECs cells pre-starved for 6 hours in EBM-2 were collected, resuspended in EGM-2 medium w/o Fibronectin either with or without VEGF and seeded into fragments and BSA treated wells. Cell density of 50,000 cells per well in 24-well glass-bottom plates was used. After 12 hours, cells were fixed in 1% PFA for 15 min and stained for VE-cadherin. Cell samples were first fixed in 1% PFA for 15 min, washed three times with 1XPBS for 5 min before blocked for 2 hrs at room temperature in blocking buffer: 1XPBS+

0.1%BSA + 0.1% Tween-20 + 0.3M Glycine+ 10% Normal Goat Serum. Samples were incubated in a primary antibody Rabbit anti- VE Cadherin (Abcam; ab3316, 1:500) overnight at 4°C, followed by a secondary antibodies Donkey anti-Rabbit (1:500) and 2µg/ml DAPI for 1 hour. Imaging was performed using a Nikon C2 confocal and images were analyzed using Image J. At least three independent wells were evaluated per condition. Grey value distributions were analyzed using Image J.

4.2.16Hyaluronic Acid-Acrylate Synthesis

Sodium hyaluronan was modified to contain acrylate functionalities as previously described¹²³. Briefly, hyaluronic acid (2.0 g, 5.28 mmol, 60 kDa) was reacted with 18.0 g (105.5 mmol) of adipic acid dihydrazide (ADH) at pH 4.75 in the presence of 4.0 g (20 mmol) of 1-ethyl-3-[3-dimethylaminopropyl] carbodiimide hydrochloride overnight and purified through dialysis (8000 MWCO) against a 100–0 mM salt gradient water for 2 days. The purified intermediate (HA-ADH) was lyophilized and stored at –20 °C until used. Approximately 60% of the carboxyl groups were modified with ADH, which was determined using ¹H-NMR (D₂O) by taking the ratio of peaks at $\delta = 1.6$ and 2.3 corresponding to the eight hydrogens of the methylene groups on the ADH to the singlet peak of the acetyl methyl protons in HA ($\delta = 1.88$). HA-ADH (1.9 g) was reacted with N-acryloxysuccinimide (NHS-Ac) (1.33 g, 4.4 mmol) in HEPES buffer (10 mM HEPES, 150 mM NaCl, 10 mM EDTA, pH 7.2) overnight and purified through dialysis against a 100–0 mM salt gradient for 1 day, then against DI water for 3–4 days before lyophilization. The degree of acrylation was determined to be ~10% using ¹H-NMR (D₂O) by taking the ratio of the multiplet peak at $\delta = 6.2$ corresponding to the *cis*- and *trans*-acrylate hydrogens to the singlet peak of the acetyl methyl protons in HA ($\delta = 1.88$) (Data not shown here).

4.2.17 Vascular Endothelial Growth Factor Nanocapsules Synthesis

The nanocapsules were synthesized using in situ free-radical polymerization as previously published by our group. Briefly, to synthesize n(VEGF), VEGF was diluted in a buffer solution of 10×10^{-3} M sodium bicarbonate (pH = 8.55) at a final reaction concentration of $100 \mu\text{g ml}^{-1}$. Acrylamide (AAM) and N-(3-aminopropyl)methacrylamide (APM) and crosslinkers (bisacrylated L/D-KNRVK, or methylene bisacrylamide) were subsequently added to the protein solution (at the molar ratio of VEGF:AAM:APM:crosslinker = 1:3000:3000:600). Different ratio of L/D crosslinkers were used to generate 100%, 75%, 50% and 25% n(VEGF). Later, these n(VEGF)s were mixed at equal amount for controlled release of VEGF.

4.2.18 HA Hydrogel Storage Modulus Optimization

HA hydrogel was formed in 0.3M pH 8.2 HEPES buffer, following steps as below.

Tube 1: HA-ADH-Ac in HEPES buffer (ADH modification is 65.62% and Ac modification is 13.33%) was incubated with fibronectin fragments for 20 min. Tube 2: Poly(ethylene glycol) dithiol (MW 1000, Sigma-Aldrich, #717142) and Alexa Fluor 555 C2 Maleimide (Thermo Fisher Scientific, #A-20346) solutions in HEPES buffer were mixed together at equal moles for 20 min to generate fresh SH-PEG-AF555. Tube 1 was then mixed with Tube 2 mixture for 20 min before nanocapsules of VEGF were added. Di-cysteine modified Matrix Metallo-protease (MMP) (Ac-GCRDGPQGIWGQDRCG-NH₂) (GenScript) sensitive crosslinker was added in the end to initiate gelation. Gelation was allowed for 30 min at 37°C. To determine the storage modulus range, gels with different thiol to acrylate (R ratio) were tested. Pre-swelled HA hydrogels (8mm in diameter and 1mm thickness) were placed between 8mm (diameter) rheological discs at normal force of 0.01N using a plate-to-plate rheometer (Anton Paar Physica MCR 301

Rheometer). The storage modulus was measured under constant 1% amplitude, from 10 to 0.1 rad/s angular frequency. Three independent gels were casted and evaluated per R ratio condition.

4.2.19HA Gel Formula for SubQ Mice Model

HA hydrogel was synthesized as described above. Briefly, HA-ADH-Ac is dissolved into 0.08mg/ml solution in 0.3 M HEPES buffer (pH8.2). The solution is then incubated with Fn9*10 or Fn9(4G)10 for 20 min. SH-PEG-AF555, nanoVEGF, and MMP crosslinker are added sequentially. R ratio of 0.60 was used for animal experiment.

Table 4.1 HA Gel Formula for SubQ Mice Model

HA-ADH-Ac	3.5 wt%
MMP crosslinker	3.335mM
SH-PEG-AF555	10 μ M
Fn9*10 or Fn9(4G)10	10 μ M
VEGF nanocapsules	200ng/50 μ l Gel

4.2.20SubQ Mice Model

G*Power was first used to compute the required sample size. Using two-tailed t-test on previous SubQ data and high variance assumption for the tortuosity measurement, we found the required sample size to be within the range of 3 to 6. We choose to start with 6 animals per group.

All *in vivo* studies were conducted in compliance with the NIH Guide for Care and Use of Laboratory Animals and UCLA ARC standards. Seven to nine week old male Balb/c mice were used to study cellular infiltration and blood vessel formation in HA gels with different fibronectin fragments since this strain has been used for wound healing and angiogenesis assay¹²⁴. Mice were anesthetized with 2–3% isoflurane in an induction chamber and kept under anesthesia during the whole surgery. The back of the mouse was shaved, washed with betadine and 70% ethanol. Two lateral incisions appropriate to the size of the implant were made in the skin (one on each side of the midline of the animal) using scissors. Two subcutaneous pockets were subsequently created by blunt dissection using rounded-end scissors. The hydrogels were inserted into each respective subcutaneous pocket and closed with a single wound clip. All animals were administered with an anti-inflammatory agent (Carprofen, Rimadyl, 5mg/kg) for the first 48 hours after surgery. At day 7, the clips were taken off. After 2 weeks, each mouse was injected with 100ul of 1mg/ml of isolectin GS-IB₄-AF488 conjugate (ThermoFisher Scientific, #I21411) through the left external jugular vein before and sacrificed by isoflurane overdose. The implant hydrogels (total of 6 blank gels, 6 Fn9*10 gels, 6 Fn9(4G)10 gels) were then collected and fixed in 1% PFA for 16 hours at 4°C. Due to the variance in sample collection process, the membrane layers attached to the implants were intact only for 4 gel implant per condition. Thus, for confocal imaging, only those with intact membranes were analyzed. For sheet confocal analysis, it doesn't require the intact cell membrane the focus was on vessel infiltration, thus we used 6 individual implant gels per condition for quantification purposes.

4.2.21 SubQ Mice Model Quantification

Samples were first imaged using a Nikon C2 confocal to visualize the superficial vascular network on the surface of the sample. For space filling analysis, confocal images were converted to binary images and analyzed using the Matlab software package. Images were divided into equally sized regions using window sizes of 256 pixels in length for 4x4 heat map

images. The fraction of non-white pixels in each region was calculated and utilized to generate an associated heat map indicating the degree of vascular signaling present in that region. Color map scale bars were set in grayscale.

Light sheet microscopy was then used to image the vascular infiltration in the implanted gel. Briefly, fixed hydrogel samples were inserted into a transparent 6mm tube. The tubes were then filled with 0.3% agarose solution in PBS. After the agarose gel solidified, samples were fixed in position and sheet confocal images were taken at 4x magnification for whole-mount samples (3-5 μ m step size, 6000 images total). After 3D rendering, 100 μ m-thick samples were sliced out to merge into single-plane maximum intensity projection image (none-overlapping samples, 4 to 6 different slices from each gel sample, 6 individual implant gels per condition).

4.2.22 Ischemic Stroke Model

G*Power was first used to compute the required sample size. Using two-tailed t-test on previous stroke data and high variance assumption for the vessel density measurement, we found the required sample size to be within the range of 3 to 9. We used 7 or 8 animals per group.

Animal procedures were performed in accordance with the US National Institutes of Health Animal Protection Guidelines and the University of California Los Angeles Chancellor's Animal Research Committee. Focal and permanent cortical stroke was induced by a middle cerebral artery occlusion (MCAo) on young adult C57BL/6 male mice (8-12 weeks) obtained from Jackson Laboratories. Briefly, under isoflurane anesthesia (2–2.5% in a 70% N₂O/30% O₂ mixture), a small craniotomy was performed over the left parietal cortex. One anterior branch of the distal middle cerebral artery was then exposed, electrocoagulated and cut. Body

temperature was maintained at 36.9 ± 0.4 °C with a heating pad throughout the operation. In this model, ischemic cellular damage is localized to somatosensory and motor cortex ¹²⁵.

Five days later, HA hydrogel precursor (see Table for composition) was loaded into a 25 μ l Hamilton syringe (Hamilton, Reno, NV) connected to a syringe pump. The solution was then injected in liquid form directly into the stroke cavity using a 30-gauge needle at stereotaxic coordinates 0.26 mm anterior/posterior (AP), 3 mm medial/lateral (ML), and 1 mm dorsal/ventral (DV) with an infusion speed of 1 μ l/min. The needle was withdrawn from the mouse brain immediately after the injection was complete.

Table 4.2 HA Gel Formula for Ischemic Stroke Model

HA-ADH-Ac	3.5 wt%
MMP crosslinker	3.335mM
Fn9*10 or Fn9(4G)10 or RGD	10 μ M (FnV) or 500 μ M (RGD)
VEGF nanocapsules (nV) or soluble VEGF (Vs)	200ng/6 μ l Gel

Ten days following the hydrogel transplantation, animals injected with fibronectin fragment (Vs+ Fn9*10, nV+Fn9*10 and nV+Fn9(4G)10) containing hydrogels were perfused with DyLight 594 labeled Lycopersicon Esculentum (Tomato) Lectin (Vector Laboratories, #DL-1177) through the left through external jugular vein and then sacrificed by isoflurane overdose. Other mice conditions (No gel, HA-RGD and Vs+HA-RGD) were perfused with 4% PFA and sacrificed.

4.2.23 Brain tissue processing

Mice brains were harvested and post-fixed in 4% PFA overnight or perfused with PFA before harvesting, then cryoprotected in 30% sucrose in phosphate buffer for 24 hours and frozen. Tangential cortical sections of 30 μm -thick were sliced using a cryostat and directly mounted on gelatin-subbed glass slides. Brain sections were then washed in PBS and permeabilized and blocked in 0.3% Triton and 10% Normal Donkey Serum before being immunohistochemically stained. The primary antibody Rat anti-Ter-119 (R&D Systems, #MAB1125, 1:200), Rabbit anti-Glut-1 (Glucose Transporter1, Abcam, 1:400) or Rabbit anti-Fibronectin (Millipore, AB2040, 1:200) were incubated overnight at +4°C followed by secondary antibodies Donkey anti-rat and rabbit- AF488 (Thermo Fisher Scientific, 1:200) for 1 hour at room temperature. After 3x 10 minute washes in PBS, the slides were dehydrated in ascending ethanol baths, dewaxed in xylene and coverslipped over fluorescent mounting medium (Dako).

4.2.24 Microscopy and Morphoanalysis

Analyses were performed on microscope images of 3 coronal brain levels at +0.80 mm, -0.80 mm and -1.20 mm according to bregma, which consistently contained the cortical infarct area. Each image represents a maximum intensity projection of 10 to 12 Z-stacks, 0.85 μm apart, captured at a 20x magnification with a Nikon C2 confocal microscope using the NIS Element software.

To quantify the vascular bed in the no gel and gel conditions, Glut-1 stained only or Glut-1 plus tomato lectin in tomato lectin-perfused animals were quantified. Tomato lectin alters Glut-1 staining such that in lectin-perfused animals the combination of both stains reveals the vascular bed the same as Glut-1 alone in tomato lectin-unperfused animals (Figure 4.13).

The vascular area (stained by Glut-1 only or by both tomato lectin and Glut-1) in the infarct and peri-infarct areas was quantified in 8 randomly chosen regions of interest (ROI) of 0.3 mm² in both regions. In each ROI, the positive area was measured using pixel threshold on 8-bit converted images (ImageJ v1.43, Bethesda, Maryland, USA) and expressed as the area fraction of positive signal per ROI. Values were then averaged across all ROI and sections, and expressed as the average positive area per animal.

The evaluation of perfused vascular ramifications allows for a quantitative analysis of the vessel architecture, by counting manually the number of branching points on positively tomato lectin perfused vessels of the peri-infarct per mm².

4.2.25 Statistical Analysis

Statistical analyses were performed using Prism (GraphPad, San Diego, CA). Data were analyzed using a one-way analysis of variance (ANOVA) followed by a Tukey post-hoc test and a 95% confidence interval. For 2D VE-cadherin staining analysis (n=3) and stroke model quantification (minimum n=5), two-tailed unpaired test was used. The results are expressed as mean ± SD.

Single, double, triple and quadruple asterisks represent $p < 0.05$, $p < 0.01$, $p < 0.001$ and $p < 0.0001$, respectively. A p value < 0.05 was considered statistically significant.

4.3 Results and discussions

4.3.1 Design and characterization of Integrin-specific 2D surfaces

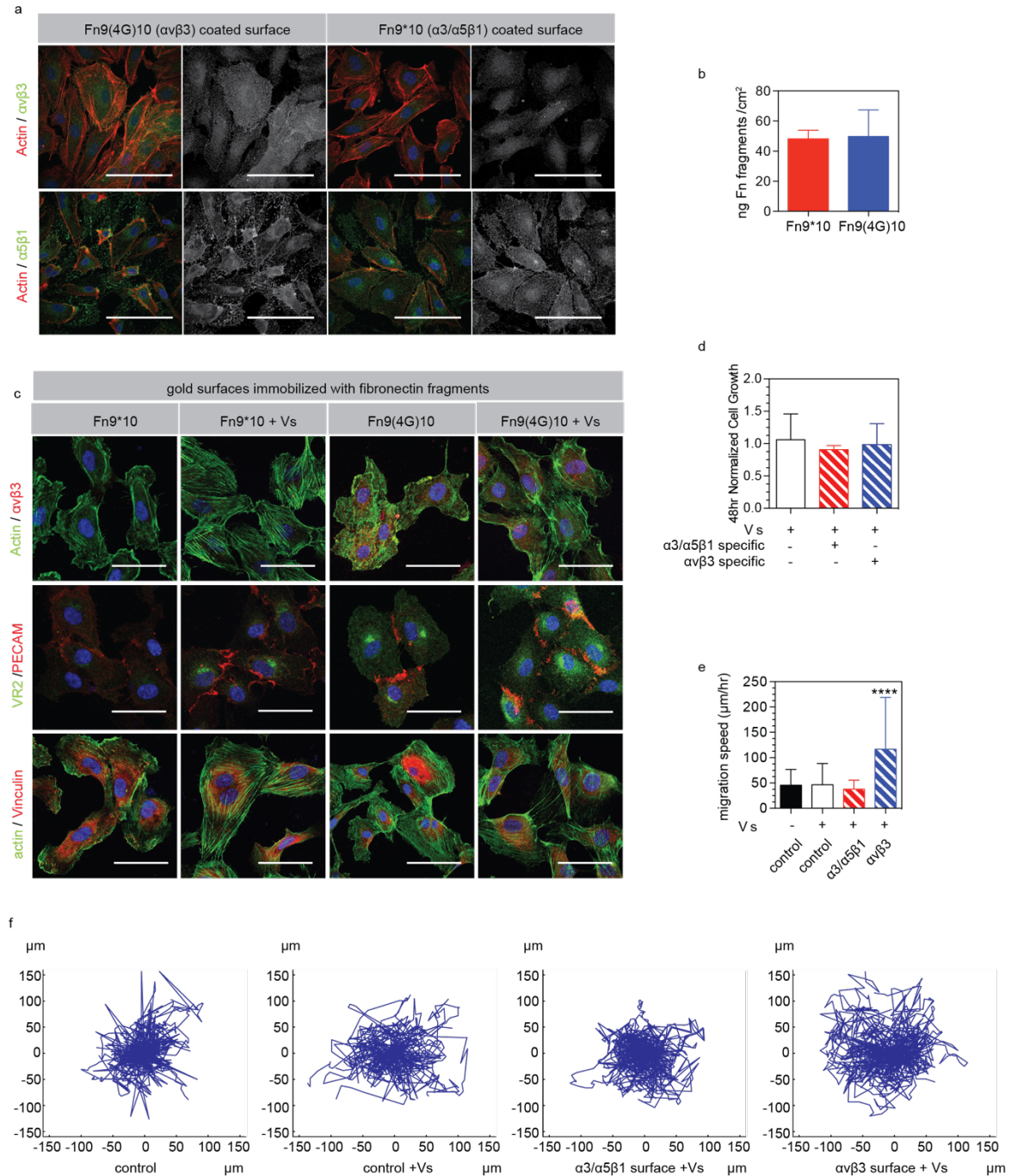


Figure 4.12D characterizations of Human Umbilical Vascular Endothelial Cells (HUVECs) on Fn9*10 or Fn9(4G)10 coated glass bottom cell culture plate or on fragments immobilized heparin-based gold surfaces. (a) Immunofluorescence staining of $\alpha5\beta1$ and $\alpha\beta3$ integrin of HUVECs after 18 hours culture in

24-well glass bottom cell culture plate which was pre-coated with 500 μ l of 2 μ M Fn9*10 or Fn9(4G)10 overnight (scale bar 100 μ m). (b) Similar amounts of immobilized recombinant fibronectin fragments Fn9*10 and Fn9(4G)10 on gold surfaces indicated similar reactivity of these two fragments. (c) Immunofluorescence staining of α v β 3 integrin, vinculin and PECAM for HUVECs after culturing 24 hours on top of fragments immobilized heparin-based gold surfaces (scale bar 50 μ m). (d) Proliferation study of HUVECs after 48 hours of culture on Fn9*10 or Fn9(4G)10 immobilized surfaces with 2ng/ml of VEGF (4 experiments, 8 wells from each experiment, normalized to control well without VEGF). (e) Migration speed analysis of HUVECs on top of Fn9*10 or Fn9(4G)10 immobilized gold surfaces (n=64). **** indicate $P < 0.0001$. (f) Migration path of HUVECs (overlapping of 64 individual cell path) on control gold surface, control gold surface with 2ng/ml of VEGF, Fn9*10 and Fn9(4G)10 immobilized gold surfaces with 2ng/ml of VEGF.

Fibronectin fragments coated surfaces were first used to verify the specific integrin activations on human umbilical endothelial cells (HUVEC). Clear α v β 3 integrin staining was observed on Fn9(4G)10 coated surface while signal on Fn9*10 coated surface was low. Also, clear β 1 integrin staining was observed at cell edge only on Fn9*10 coated surface (Figure 4.1a). Together, these findings verify the integrin activation specificity for these two fragments. To better understand the effects of these fragments when they are immobilized, self-assembled monolayers on gold were used to specifically immobilize fibronectin fragments and the modified surfaces were used for in vitro characterization. Amine containing self-assembled monolayers were constructed and used to immobilize maleimide-modified heparin via carbodiimide chemistry. Fn9*10 and Fn9(4G)10 were subsequently covalently bound using Michael type addition between the maleimide on the surface and the thiol on the N-terminus of the fibronectin fragment. The amounts of attached fragments were then quantified by enzyme-linked immunosorbent assay (ELISA) and shown to be the same (~ 50 ng fragment/cm²) for both fragments (Figure 4.1b), indicating that the reactivity of both fragments is similar. The response of endothelial cells (EC) cultured on fragment-modified surfaces was assessed 24 or 48 hours post plating. ECs were able to attach and spread on either fragment-modified surface. As expected, only ECs seeded on Fn9(4G)10 surfaces showed a positive staining for α v β 3, validating that the fragment Fn9*10 does not mediate significant binding through α v β 3. The actin cytoskeleton for cells cultured on α v β 3 specific Fn9(4G)10 surfaces showed more short and disoriented actin fibers compared with α 3/ α 5 β 1 specific Fn9*10 surfaces, where actin fibers showed extensive length

(Figure 4.1c). This showed that different integrin activation from immobilized fragments impacts EC cytoskeleton arrangement on 2D.

Growth factors are critical for the process of angiogenesis and their incorporation within therapeutic angiogenic materials has been a major focus of the field. Here we are interested in using vascular endothelial growth factor A 165 (VEGF), which has been described as the master regulator of angiogenesis¹²⁶, to induce EC sprouting and angiogenesis *in vivo*. Exposure of ECs plated on Fn9*10 or Fn9(4G)10 did not change the binding to $\alpha v\beta 3$, which remained positive for Fn9(4G)10 but not Fn9*10 (Figure 4.1c). Although no proliferation difference was shown for all the conditions tested (Figure 4.1d), EC migration was significantly increased for cells cultured on Fn9(4G)10 modified surfaces, which showed induced short and disoriented actin alignment (Figure 4.1e,f). Together these findings confirm that ECs alter their cellular behavior depending on the integrin binding specificity dominating their attachment to the surface.

4.3.2 Integrin stimulation guides endothelial cell sprouting patterns

Next, we looked at the influence of fibronectin mediated cell adhesion on vascular endothelial growth factor A 165 (VEGF) induced vascular sprouting. To study the role of fibronectin in EC sprouting, two types of fibrinogen were used, one that contains fibronectin (Fib1) and one that is fibronectin and Von Willebrand factor depleted (Fib3). EC coated beads were suspended in the fibrin matrices and cultured in the presence of 2ng/ml soluble VEGF for 7-days following the protocol of Hughes et al^{127, 128}. At day 7, the cultures were fixed, stained for actin, and quantified for the number of sprouts, number of branching points and total network length per bead.

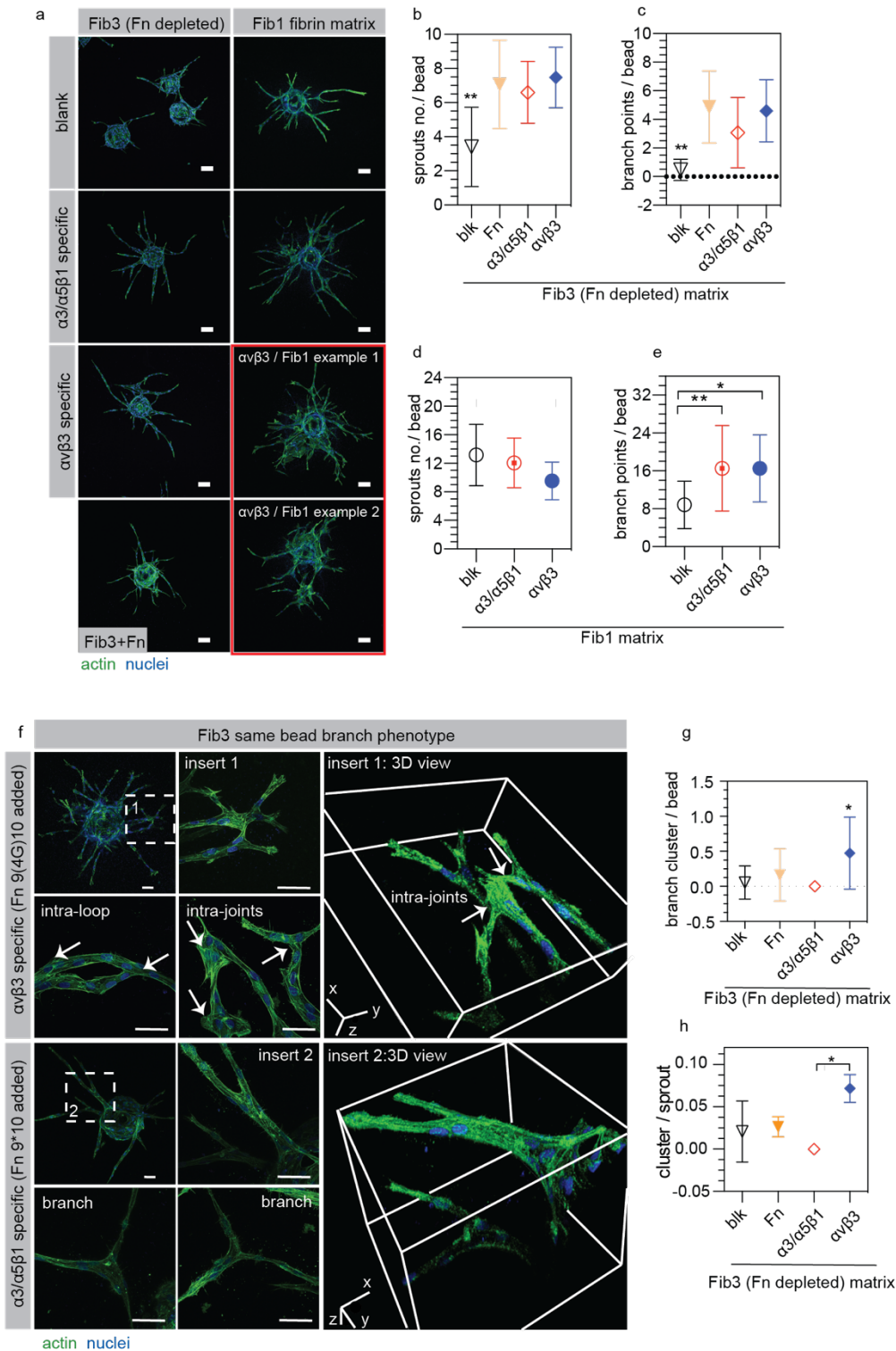


Figure 4.2 HUVEC sprouting is greatly affected by integrin activation from both fibrin matrices with and without full length fibronectin (Fn). (a) Representative immunofluorescent images for Human Umbilical Vascular Endothelial Cell (HUVEC) sprouting assay in both Fib1 (fibronectin and von Willebrand Factor

containing Fibrinogen) and Fib3 (fibronectin and von Willebrand Factor depleted fibrinogen) fibrin gel with no fibronectin fragment, 2 μ M Fn9*10 (α 3/ α 5 β 1 specific matrices) or 2 μ M Fn9(4G)10 (α v β 3 specific matrices). Scale bar: 100 μ m. (b,c) Quantification of sprout number and branch points per bead in Fib3 matrices. (d,e) Quantification of sprout number and branch points per bead in Fib1 matrices ($n \geq 15$ HUVEC coated beads, from 3 independent gels). (f) Representative images and 3D views of HUVEC branch structures in both α v β 3 and α 3/ α 5 β 1 specific Fib3 matrices. Intra-loop and intra-joint branch structures were observed in α v β 3 condition (2 μ M Fn9*10) while organized branch structures were observed in α 3/ α 5 β 1 conditions (2 μ M Fn9(4G)10). Scale bar: 50 μ m. (g) Branch clusters per bead was analyzed in Fib3 blank conditions, Fib3+1 μ M Fn, α 3/ α 5 β 1 conditions (2 μ M Fn9*10) and α v β 3 conditions (2 μ M Fn9(4G)10). (h) Cluster number per sprout was analyzed in Fib3 blank conditions, Fib3+1 μ M Fn, α 3/ α 5 β 1 conditions (2 μ M Fn9*10) and α v β 3 conditions (2 μ M Fn9(4G)10). All plots represent mean \pm SD. * and ** indicate $P < 0.05$ and $P < 0.01$, respectively.

Sprouting and branching points in fibronectin-depleted matrices was significantly decreased compared with fibronectin containing matrices, suggesting that the presence of native fibronectin is critical for EC sprouting (Figure 4.2a and Figure 4.3a). Addition of exogenous fibronectin to fibronectin-depleted matrices partially rescued EC sprouting, resulting in statistically increased sprouting, branching points and total network length (Figure 4.3 a); however, regardless of the amount of exogenous fibronectin added, the level of sprouting in fibronectin-depleted matrices was significantly lower than that observed in fibronectin containing matrices (Figure 4.2a and Figure 4.3a). This indicated that besides the endogenous fibronectin within the Fib1 matrices, other factors removed during the Fib3 preparation (e.g. von Willebrand factor) may also be important for EC sprouting in fibrin. Among all the tested fibronectin concentrations, it was also observed that 1 μ M was the lowest concentration that achieved statistically increased sprouting, branching points and total network length (Figure 4.3a). Thus, we decided to incorporate equal molar concentration of Fn fragments, since each fibronectin protein presents two copies of Fn III9-10, 2 μ M of the fragments were used.

We next tested the role of full length fibronectin, Fn9*10 and Fn9(4G)10 containing matrices of EC sprouting. Both the number of sprouts and the branch points per bead showed no significant difference among full length fibronectin, α 3/ α 5 β 1-specific (Fn9*10 fragment added) and α v β 3-specific (Fn9(4G)10 fragment added) conditions, indicating that integrin engagement

is a major factor that affects the sprouting outcomes (Figure 4.2a-e and Figure 4.3b). Between $\alpha3/\alpha5\beta1$ -specific and $\alpha v\beta3$ -specific conditions we observed no differences in sprout number, branch points or total network length (Figure 4.2b-e, from three independent gels, and Figure 4.3b-i, comparing cross three different days); however, the addition of 9(4G)10 fibronectin fragment ($\alpha v\beta3$ -specific specific gels) resulted in cluster formation (Figure 4.2a,f). We observed sprouting “clusters” in the $\alpha v\beta3$ -specific matrices but not on blank, fibronectin, or $\alpha3/\alpha5\beta1$ -specific matrices (Figure 4.2a,f). The “clusters” are merged vessel branch clumps from the same bead, which can either locate close to the surface of the beads or on the sprouts. They are always presented as chaotic branch bundles, thus the number of branches and sprouts within them are difficult to discern. Using high resolution z-stack confocal imaging we found that the clusters were associated with intra-loop and intra-joint structures both within and between neighboring sprouts, which were not observed in $\alpha3/\alpha5\beta1$ -specific matrices (Figure 4.2 f). The quantification of the number of branch clusters per bead showed statistically significant occurrence in $\alpha v\beta3$ -specific gels compared with the blank, fibronectin and $\alpha3/\alpha5\beta1$ -specific Fib1 or Fib3 matrices from both the representative single day experiment with three independent gels and three different day experiments treating each day as an independent experiment (Figure 4,2g, Figure 4.3j,k and Figure 4.5a-c). The quantification of the number of branch clusters per sprout and per branch also showed a similar trend (Figure 4.2h and Figure 4.5d-f). These intra-loop and intra-joint features represent chaotic tumor-like vasculature with over-branched and excessive-shunt vessels¹²⁹. Taken together, these results demonstrate that although both Fn fragments enhanced sprouting and branching of ECs *in vitro*, they lead to different vascular patterns in the resulting EC network. In particular, $\alpha v\beta3$ -specific matrices promoted the formation of a pathological vascular network containing intra-loop and intra-joint features.

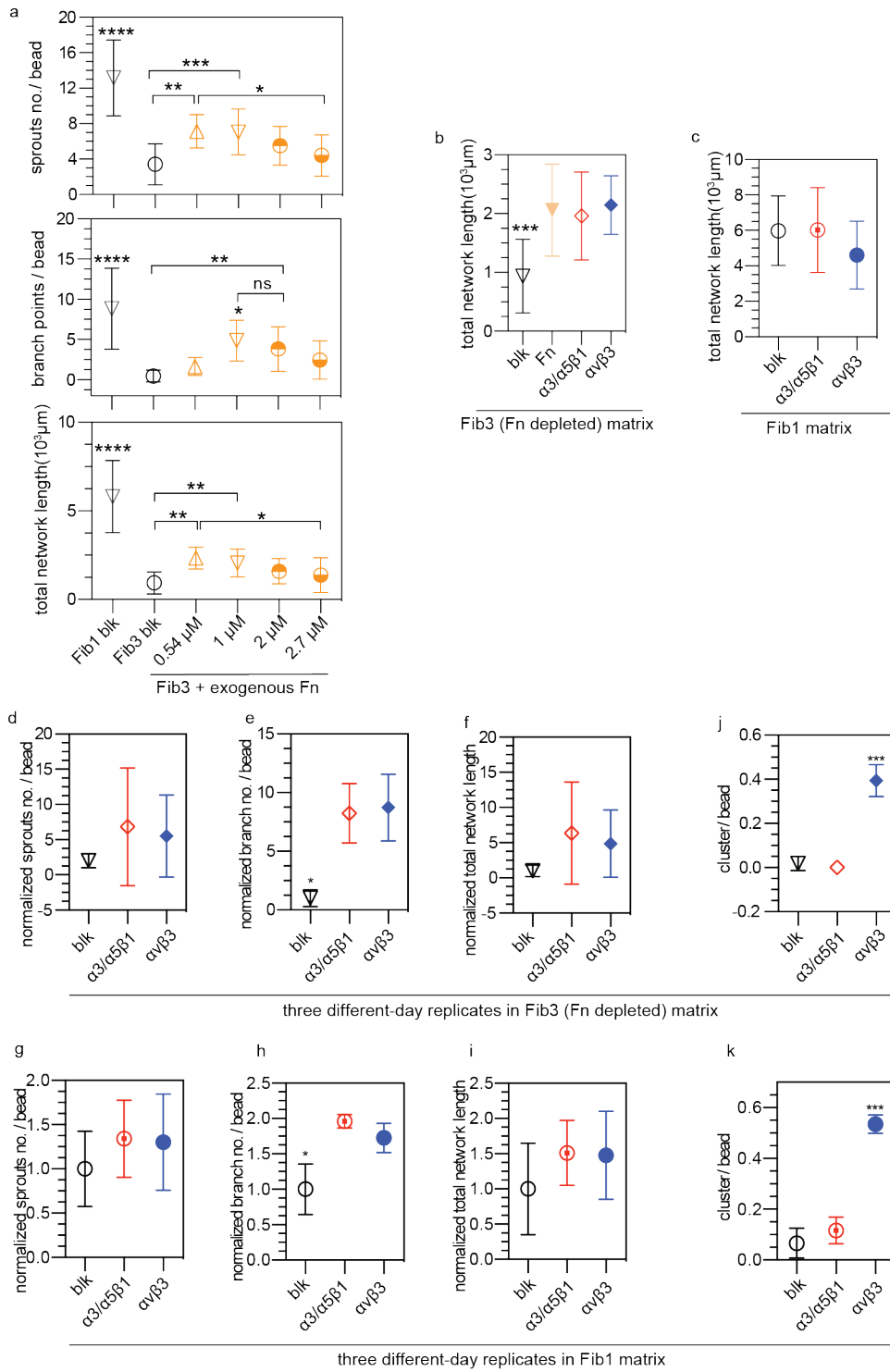


Figure 4.3(a) Human Umbilical Vascular Endothelial Cell (HUVEC) sprouting assays were performed within both Fib1(Fn and Von Willebrand Factor containing Fibrinogen) and Fib3(Fn depleted Fibrinogen) matrices. Different amounts of exogenous Fn were added to Fib3 to understand the effects of fibronectin on sprouting process. Total network length per bead including all sprouts and branches was shown here (n>=15, from 3 independent gels). (b) Quantification of total network length per bead in Fib3 matrices. (c) Quantification of total network length per bead in Fib1 matrices. (d-f) The Fib3 (fibronectin-depleted) fibrin sprouting assay were repeated three times on different days. Normalized quantification of sprout number, branch points and total network length per bead with all three experiments were shown here. n=3, each day considered as one sample. (g-i) The Fib1 fibrin sprouting assay were repeated three times on different days. Normalized quantification of sprout number, branch points and total network length per bead with all three experiments were shown here. n=3, each day considered as one sample. (j) Quantification of cluster occurrence per bead in Fib3 (fibronectin-depleted) fibrin matrices with three repeated experiments in different days were shown here. n=3, each day considered as one biological replicate. (k) Quantification of cluster occurrence per bead in Fib1 fibrin matrices with three repeated experiments in different days were shown here. n=3, each experiment considered as one sample. *, **, *** and **** indicate P < 0.05, P < 0.01, P < 0.001 and P < 0.0001, respectively.

The involvement and importance of integrins in EC sprouting was further confirmed through function blocking antibody studies. VEGF induced EC sprouting in $\alpha 3/\alpha 5\beta 1$ -specific matrices in the presence of function blocking antibodies against either $\alpha 5$ or $\beta 1$ completely inhibited the sprouting process to a level lower than observed in fibronectin depleted matrices. In contrast, EC sprouting in $\alpha v\beta 3$ -specific matrices in the presence of function blocking antibodies against αv did not impact sprouting, while function blocking antibodies against $\beta 3$ again completely inhibited the sprouting process. These results indicate that $\alpha 5$, $\beta 3$, and $\beta 1$ are essential to EC sprouting but αv is not (P3G8 antibody concentration was optimized using flow cytometry in Figure 4.5g,h), further illustrating the importance of integrin binding to biomaterials to promote angiogenesis (Figure 4.4a and Figure 4.5i,j). We next explored whether blocking αv normalized the resulting vasculature by decreasing the number of intra-loop and intra-joint structures. Surprisingly, blocking αv binding significantly decreased the number of branch clusters (Figure 4.4b), suggesting that αv binding is responsible for the sprout clusters formed in the $\alpha v\beta 3$ -specific matrices. These results are in agreement with previous studies showing that activation of $\alpha v\beta 3$ results in increased vascular permeability in 2D²⁶ while inhibition of αv reduces vascular permeability¹³⁰.

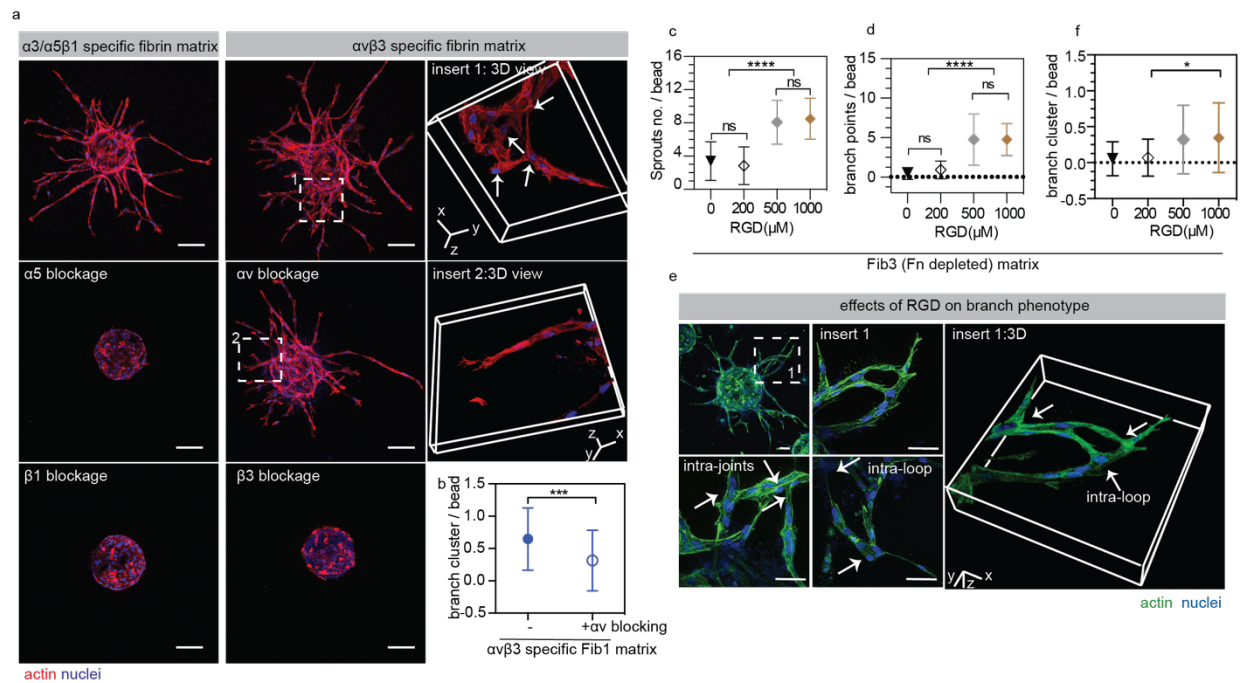


Figure 4.4 Intra-joint and intra-loop structure exist in matrices dosed with 9(4G)10 and RGD. (a) Microscopic analysis of whole bead sprouting outcomes (scale bar: 100 μm) and intra-joint and intra-loop branch structures (scale bar: 50 μm) from the blockage of integrin αv, α5, β1 or β3 (5 μg/ml) of 2 μM Fn9(4G)10 or 2 μM Fn9(4G)10 added Fib1 gels. (b) Branch cluster occurrence comparison between 2 μM Fn9(4G)10 Fib1 gels with and without αv blocking (n=51 HUVEC coated beads from three independent gels). (c,d) Sprout number per bead and branch points per bead were quantified in 0, 200, 500 and 1000 μM RGD added Fib3 matrices (n≥15 HUVEC coated beads, from 3 independent gels). (e) Representative image of intra-loop and intra-joints structures in Fib3 matrices with 1000 μM RGD added. Scale bar: 50 μm. (f) Branch cluster occurrence per bead were quantified in 0, 200, 500 and 1000 μM RGD added Fib3 matrices. All plots represent mean ± SD. *, **, *** and **** indicate P < 0.05, P < 0.01, P < 0.001 and P < 0.0001, respectively.

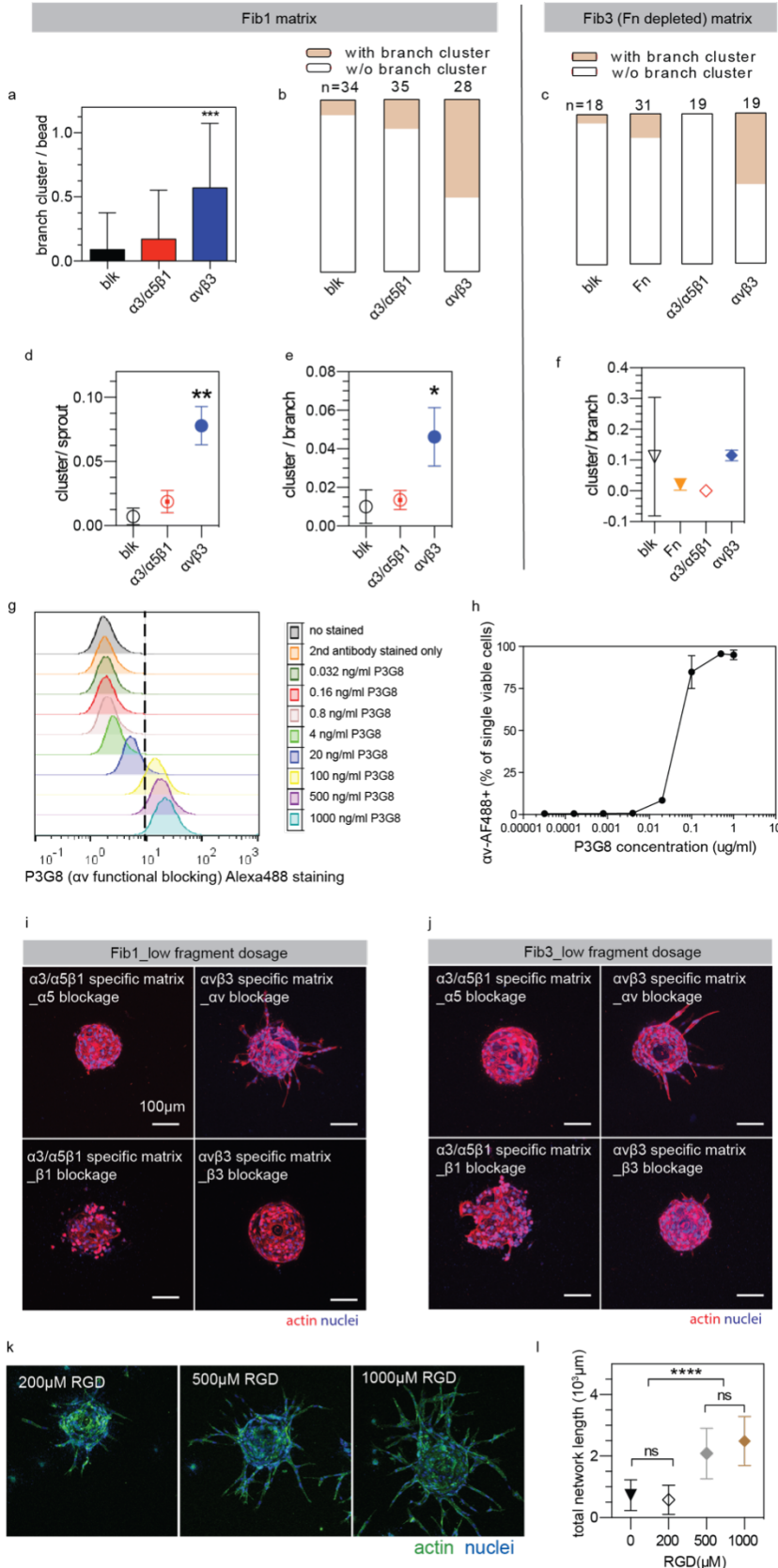


Figure 4.5(a,b) Average branch cluster per bead and branch cluster distribution were analyzed for blank, $\alpha 3/\alpha 5\beta 1$ specific (2μ M Fn9*10) and $\alpha v\beta 3$ specific (2μ M Fn9(4G)10) Fib1 matrices. (c) Branch cluster distribution was analyzed for blank, 1μ M Fn added, $\alpha 3/\alpha 5\beta 1$ specific (2μ M Fn9*10) and $\alpha v\beta 3$ specific (2μ M Fn9(4G)10) Fib3 matrices. (d,e) Cluster number per sprout and cluster number per branch were analyzed in blank, $\alpha 3/\alpha 5\beta 1$ specific (2μ M Fn9*10) and $\alpha v\beta 3$ specific (2μ M Fn9(4G)10) Fib1 conditions. (f) Cluster number per branch were analyzed in blank, 1μ M Fn added, $\alpha 3/\alpha 5\beta 1$ specific (2μ M Fn9*10) and $\alpha v\beta 3$ specific (2μ M Fn9(4G)10) Fib3 conditions. (g,h) FACS analysis of the efficiency of αv blocking functional antibody P3G8. 1μ g/ml of P3G8 in 100ul of media was shown to effectively bind to more than 95% of αv integrin on 60,000 HUVECs. (i,j) Microscopic analysis of whole bead sprouting outcomes (scale bar: 100 μ m) from the blockage of integrin αv , $\alpha 5$, $\beta 1$ or $\beta 3$ (5μ g/ml, replenished every 2 days) on 0.267μ M Fn9*10 or 0.239μ M Fn9(4G)10 dosed Fib1 and Fib3 matrices. (k,l) Microscopic analysis and quantification for total network length in 0, 200, 500 and 1000 μ M RGD modified Fib3 matrices. *, ***, and **** indicate $P < 0.05$, $P < 0.001$ and $P < 0.0001$, respectively.

4.3.3 Matrices modified with RGD peptides show similar vascular pattern as Fn9(4G)10

Next, we sought to examine vascular patterns utilizing the ubiquitously used synthetic peptide derived from fibronectin, RGD. RGD peptides with $\alpha_2\text{PI}_{1-8}$ sequences (H-NQEQVSPLRGDSPG-NH₂) were incorporated within fibrin matrices using the same FXIIIa chemistry used for the incorporation of our fibronectin fragments. As observed with the fibronectin fragments, the incorporation of RGD within Fib3 matrices resulted in enhanced EC sprouting (Figure 4.4c,d and Figure 4.5k,l). Similar intra-loop and intra-joint structures were found in RGD modified fibrin matrices (Figure 4.4e) and the number of clusters were statistically increased for matrices containing 1000 μM RGD peptide (Figure 4.4f). These results suggest that RGD binding without the presence of the proline-histidine-serine-arginine-asparagine (PHSRN) “synergy” domain on the 9th type III repeat^{131, 132}, result in pathological angiogenesis, which may come from the preferential $\alpha\text{v}\beta_3$ binding¹³³. It should be noted that the effect of enhanced sprouting and disorganized structures was only observed for a much higher concentration of RGD peptide (> 500 μM) compared with the concentration of fibronectin fragments used (2 μM); this result confirms that fibronectin fragments more efficiently display the RGD motif to cells resulting in more efficient binding.

Upregulation of $\alpha\text{v}\beta_3$ and alterations in its activation state has been associated with disease states such as cancer^{27, 134, 135} and fibrosis^{136, 137} and has been widely used as a cancer targeting ligand in drug delivery applications^{138, 139}, yet RGD is the most widely used integrin binding peptide to modify biomaterials. Our results show a dose dependent effect of RGD on vascular patterning with increasing doses leading to increased pathological vessels resulting in sprouting vessel clusters. We do not mean to suggest that the use of RGD modified biomaterials for therapeutic angiogenesis is inherently flawed; rather, we believe that the incorporation conditions for RGD peptides such as presentation, concentration, and other neighboring ligands should be studied to ensure that the desired revascularization pattern is

obtained. For example, clustering RGD within hydrogels has been shown to upregulate the expression of $\beta 1$ integrin¹⁰⁵ and immobilization of VEGF leads to $\beta 1$ recruitment⁹⁹.

4.3.4 Integrin stimulation guides vascular anastomosis

Vessel anastomosis is a crucial step in vasculature renewal and repair, guiding the fusion of adjacent vessel branches. In healthy vessels, once a vessel branch is formed, the majority of endothelial cells become quiescent, among which only 0.01% still divide¹⁴⁰. During the angiogenesis process, sprouts from parental vessels fuse with other sprouts or pre-existing blood vessels for the purposes of supplying blood and oxygen to surrounding tissues¹⁴¹⁻¹⁴³. This anastomosis process not only affects vascular network distribution, but also has great impacts on structure, quality and maturation of newly formed vessels. To test the effect of $\alpha v\beta 3$ and $\alpha 3/\alpha 5\beta 1$ on EC sprout anastomosis, a similar bead assay was performed using stably transfected ECs expressing enhanced green fluorescent protein (EGFP). HDFs were seeded within the fibrin matrix to yield more robust and long-lasting tubes for longer culture. EC sprouts were monitored daily and analyzed at day 11 when anastomosis between adjacent beads started. Normal anastomosis results in the binding of tip cells through a single tip cell contact¹⁴⁴. Clear single tip-tip contact or paralleled tip interaction were observed in both blank and $\alpha 3/\alpha 5\beta 1$ specific (Fn9*10 added) conditions (Figure 4.6a-f), indicating that further inducing $\alpha 3/\alpha 5\beta 1$ integrin engagement supports similar anastomosis as native fibronectin present in the Fib1 matrix. In contrast, $\alpha v\beta 3$ integrin engagement through Fn9(4G)10 modified matrices promoted multiple tip-tip contacts, resulting in independent contact sites and loop structures (Figure 4.6g-j). Thus, consistent with our observations in EC sprouting morphogenesis, inter-loop and inter-joint structures are observed in anastomosed sprouts within $\alpha v\beta 3$ -specific matrices.

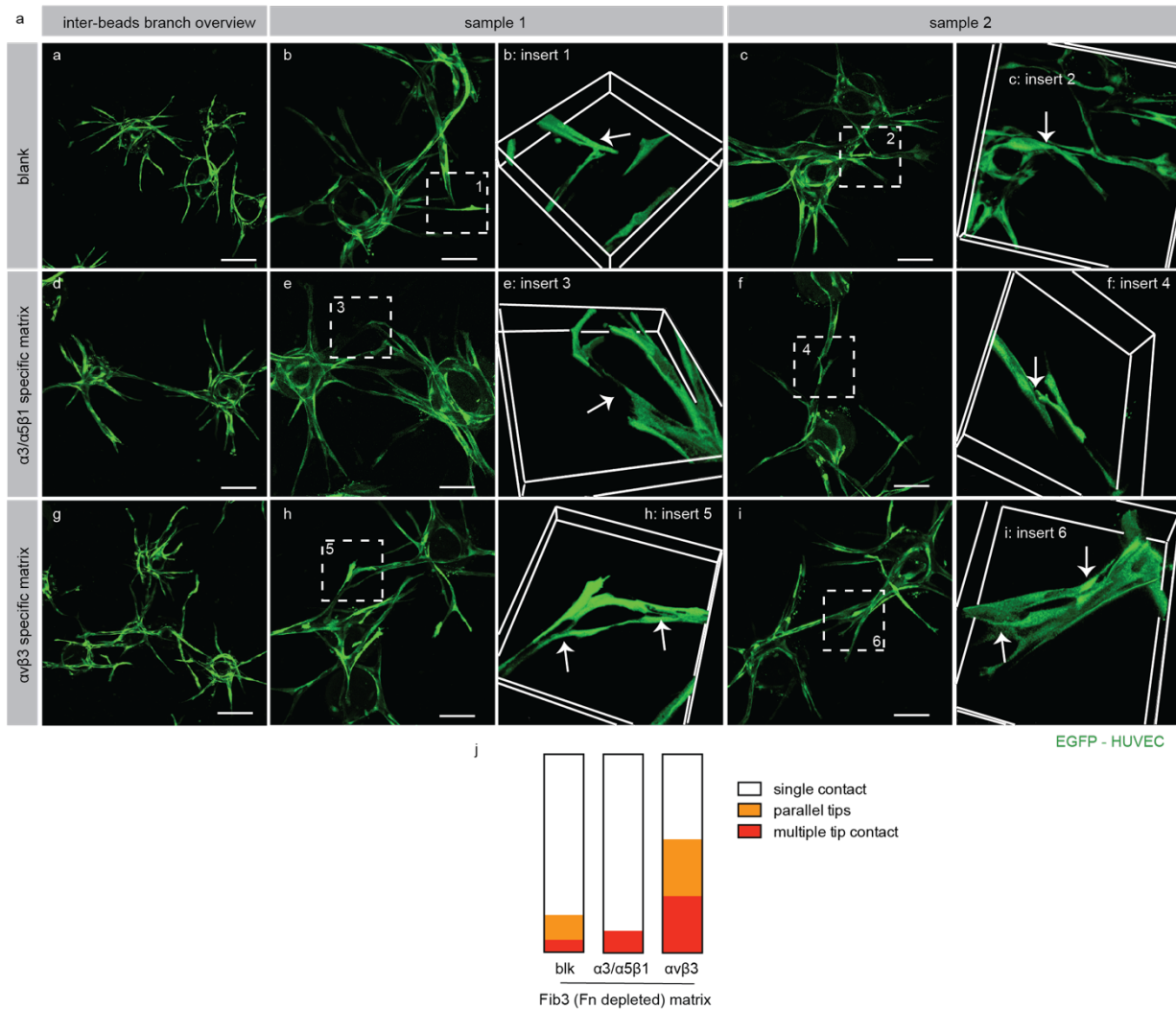


Figure 4.6 Microscopic analysis of anastomosis process of EGFP-HUVEC sprouts at day 11. (a,d,g) Inter-beads branch overview of blank, 2 μM Fn9*10 ($\alpha 3/\alpha 5\beta 1$ specific) and 2 μM Fn9(4G)10 ($\alpha v\beta 3$ specific) Fib3 gels. Scale bar: 200 μm . (b,e,h) Sample 1 of bead-bead tip cell interactions. Scale bar: 100 μm . (c,f,i) Sample 2 of bead-bead tip cell interactions. Scale bar: 100 μm . (j) Different tip-tip contact distribution within the 170 μm of working distance of 60x objective.

4.3.5 αv activation leads to pathological vasculature through VE-cadherin disruption

Next, we investigated possible mechanisms for the observed differences in the vascular patterns generated by $\alpha 3/\alpha 5\beta 1$ -specific and $\alpha v\beta 3$ -specific matrices. Failure to generate single tip-tip contact sites during anastomosis with $\alpha v\beta 3$ -specific modified matrices suggested disturbed polarization events between interacting tip cells and disrupted VE-cadherin signaling

¹⁴⁴. VE-cadherin is known to be necessary for the generation of a single polarization event

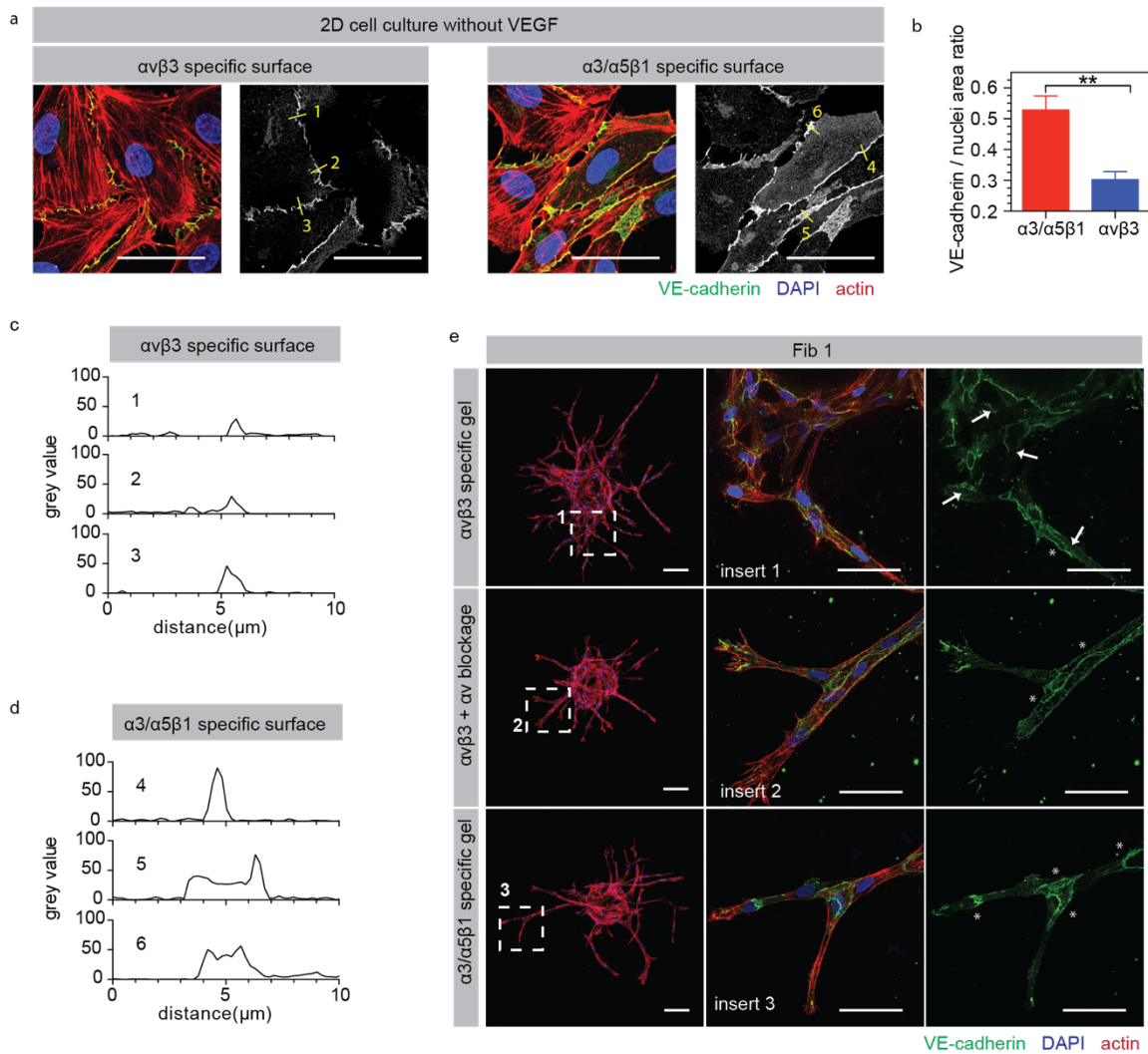


Figure 4.7. VE-cadherin disruption was observed on $\alpha\beta3$ specific 2D surface and in 3D fibrin matrices. (a) Microscopic analysis of 2D VE-cadherin distribution on $\alpha3/\alpha5\beta1$ or $\alpha\beta3$ specific surfaces without VEGF dosage after 12 hours. Scale bar: 50 μm . ** indicate $P < 0.01$. (b) Quantification of VE-Cadherin to nuclei area ratio for HUVECs on $\alpha3/\alpha5\beta1$ or $\alpha\beta3$ specific surfaces without VEGF dosage after 18 hours. (c) Grey value distribution analysis for 3 random cell-cell junctions on $\alpha3/\alpha5\beta1$ specific surface from (a). (d) Grey value distribution analysis for 3 random cell-cell junctions on $\alpha\beta3$ specific surface from (a). (e) Microscopic analysis of VE-cadherin signals from blockage of $\alpha\upsilon$ integrin on $\alpha\beta3$ specific Fib1 matrices (2 μM Fn9(4G)10) in comparison to $\alpha3/\alpha5\beta1$ specific matrices. Scale bar: 100 μm (whole bead) and 50 μm (sprouts).

between interacting tip cells ¹⁴⁴. Vessel sprouts lacking VE-cadherin display irregular anastomosis, characterized by multiple tip-tip contact sites and disturbed junctional connections

¹⁴⁴, similar to our observations in Fn9(4G)10 condition. As an important cell-cell junction protein,

VE-cadherin is not only responsible for shifting endothelial cell response to VEGF from proliferation and migration to survival and quiescence¹⁴⁵, but also functions to maintain low permeability of endothelial cell layer²⁶. Even partial knockout of VE-cadherin can lead to vascular instability and hemorrhages¹⁴⁶. Most importantly, VE-cadherin function can be disrupted by upregulation of $\alpha\beta3$ integrin, enhancing endothelial cell permeability²⁶. Thus, we hypothesize that $\alpha\beta3$ activating scaffolds lead to pathological intra-vessel and inter-vessel features through VE-cadherin disruption. To verify our hypothesis, we first examined VE-cadherin distribution on EC cultured *in vitro* on $\alpha\beta3$ or $\alpha3/\alpha5\beta1$ specific surfaces. After 18 hours, cells seeded on $\alpha3/\alpha5\beta1$ specific surface showed significantly increased amount of VE-cadherin signal at cell-cell junctions compared with $\alpha\beta3$ specific condition both without and with VEGF presence (Figure 4.7a and Figure 4.8a). Obvious absence and significantly lowered VE-cadherin signals between adjacent cells were observed on $\alpha\beta3$ specific surfaces, indicating VE-cadherin disruption (Figure 4.7a,b and Figure 4.8a). VE-cadherin grey value analysis was performed on randomly-chosen cell-cell junctions from Figure 4.7a. It was observed that $\alpha3/\alpha5\beta1$ specific surface led to wider VE-cadherin layer with stronger signal at cell-cell junction when compared with $\alpha\beta3$ specific surfaces (Figure 4.7c,d). EC sprouting in $\alpha\beta3$ specific matrices was also characterized by reduced VE-cadherin staining (missing VE-cadherin staining is labeled using the arrow) on sprout shunts and cell-cell junctions compared with EC sprouting in $\alpha3/\alpha5\beta1$ specific matrices (Figure 4.7e,f). To confirm that increased $\alpha\beta$ integrin binding is responsible for the decrease in VE-cadherin staining, $\alpha\beta$ integrin binding was disrupted using function-blocking antibodies. VE-cadherin staining after $\alpha\beta$ blocking in $\alpha\beta3$ specific fibrin matrices showed EC cells with increased VE-cadherin staining (clear VE-cadherin staining is labeled by star) similar to what was observed in $\alpha3/\alpha5\beta1$ specific matrices, indicating that $\alpha\beta$ binding is responsible for the reduction in VE-cadherin expression. The effect of $\alpha\beta$ blocking was observed in both Fib1 and Fib3 matrices (Figure 4.7e and Figure 8b,c). Taken together, these findings support our hypothesis that VE-cadherin-related pathological

vasculature was caused by αv activation and demonstrate that αv blockage can be utilized to rescue the pathological effects.

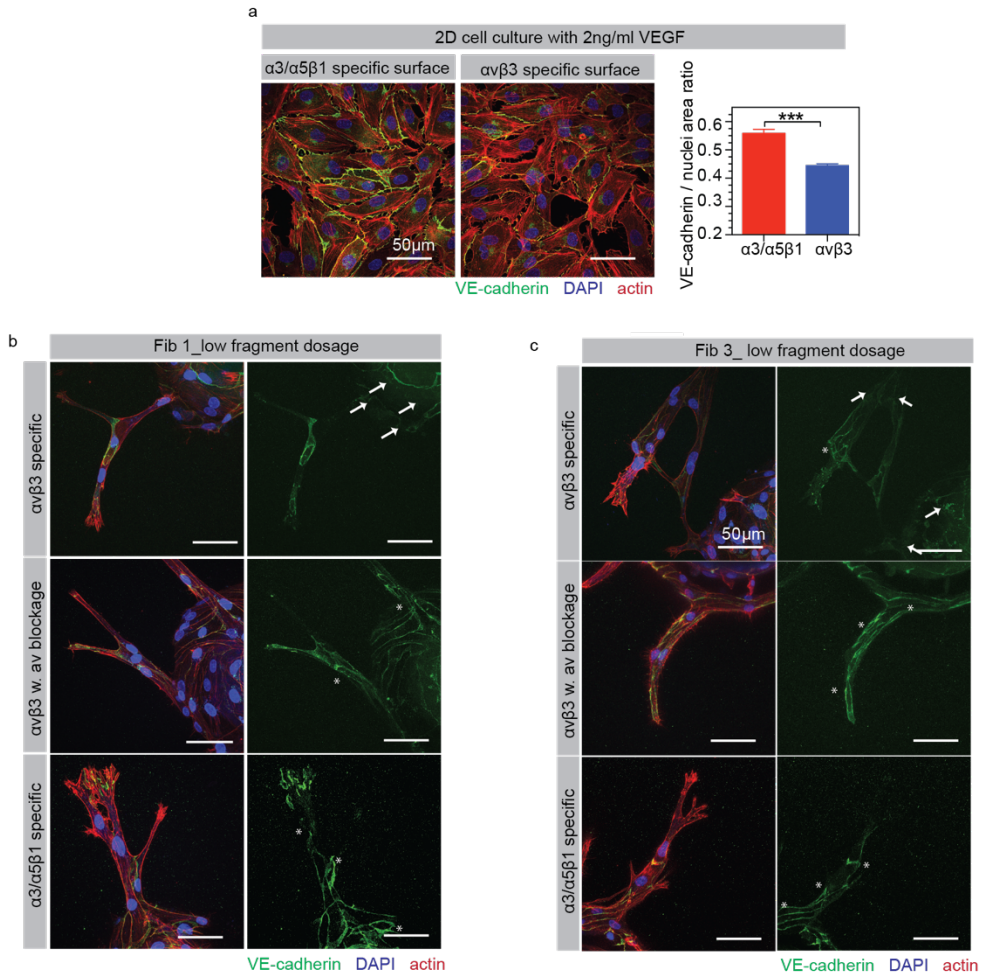


Figure 4.8 VE-cadherin disruption was observed on $\alpha v\beta 3$ specific 2D surface with presence of VEGF and also in 3D fibrin matrices. (a) Microscopic analysis and quantification of 2D VE-cadherin distribution on fragment coated cell culture dish with 2ng/ml VEGF dosage at 12 hour time point. Scale bar: 50 μ m. *** indicate $P < 0.001$. (b) Microscopic analysis of VE-cadherin signals from blockage of αv integrin on 0.239 μ M Fn9(4G)10 added Fib1 gels in comparison to 0.267 μ M Fn9*10 added Fib1 gels. (c) Microscopic analysis of VE-cadherin signals from blockage of αv integrin on 0.239 μ M Fn9(4G)10 added Fib3 gels in comparison to 0.267 μ M added Fn9*10 Fib3 gels.

4.3.6 Integrin stimulation from a bioengineered matrix guides vascular patterns *in vivo*

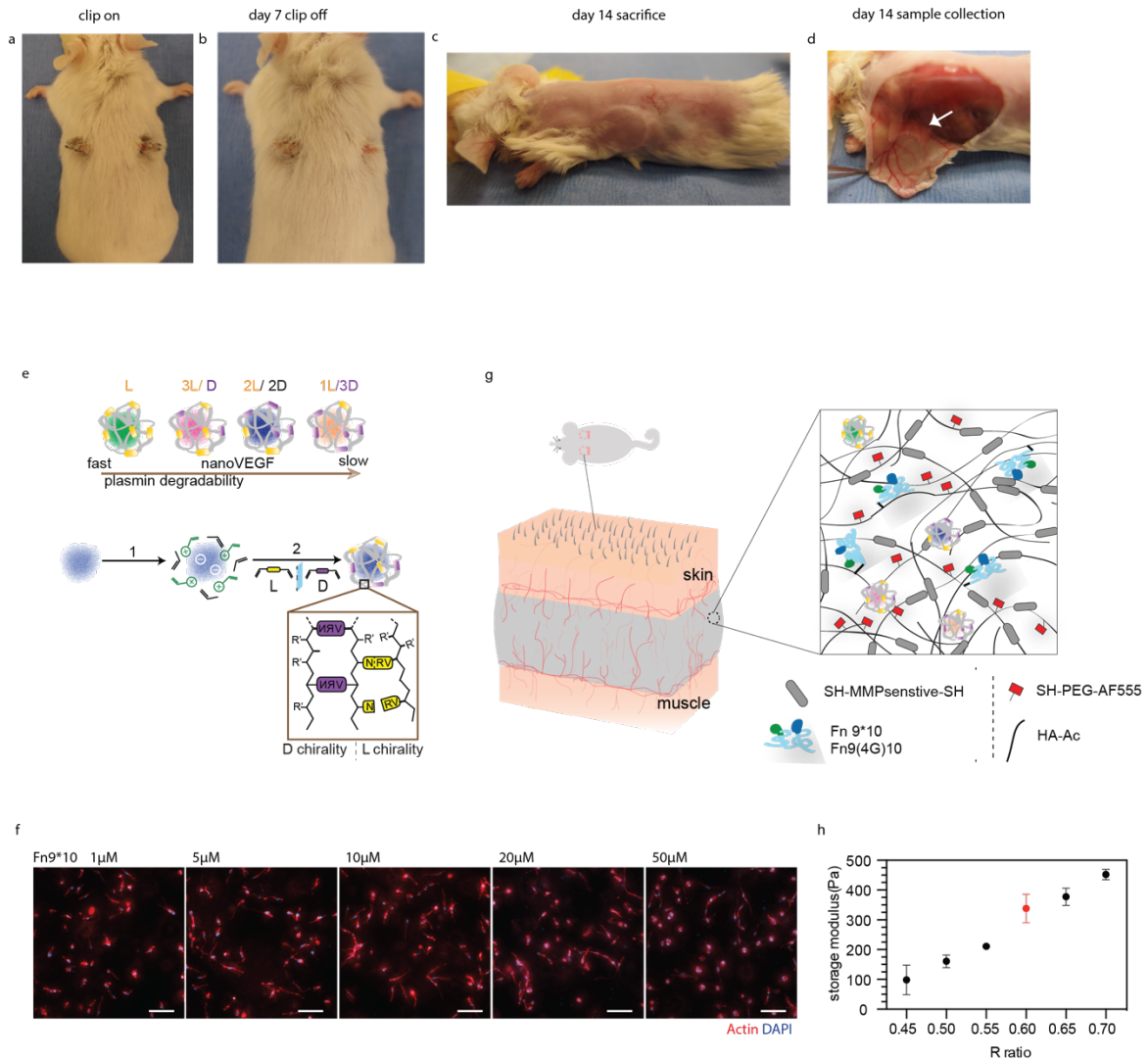


Figure 4.9 (a-d) The workflow of modified matrigel plug assay. (e) Scheme for synthesising 100% L, 75% L, 50% L and 25% L protease-sensitive VEGF nanocapsules. (g) Scheme for implanted MMP-crosslinked HA Hydrogels containing fibronectin fragments (Fn9*10 or Fn9(4G)10) and equal amount of each type of VEGF nanocapsules. The HA hydrogels were also labeled with AF555 for visualization purposes. (f) Fluorescent analysis of D1 cell spreading after 2 days in HA hydrogels with 1, 5, 10, 20, 50μM of Fn9*10 dosage. 10μM fragment induced the most cell spreading without little apoptosis. (h) Optimization of storage modulus for the HA implant hydrogel by varying R ratio (crosslinker thiols to maleimide ratio).

The fibronectin fragments were also tested in a modified matrigel plug assay that uses bioengineered hyaluronic acid (HA) hydrogels instead of matrigel to assess angiogenesis in mice (Figure 4.9a-d). HA hydrogel is chosen for our studies because it does not interact with cells through integrin receptors and provides a clean system to study integrin-mediated events.

HA hydrogel has been injected *in vivo*, has been shown to support delivery of bio cues and is also currently used under clinical settings. HA hydrogels are formed through crosslinking HA molecules using Michael type addition chemistry between acrylamide groups introduced to the backbone of hyaluronic acid and dithiol crosslinker containing protease degradable peptides¹⁴⁷. Fn fragments were also introduced to this protease degradable hydrogel matrix backbone to mediate integrin binding using the same Michael type chemistry through the cysteine in the fragment N-terminus. VEGF was incorporated into the system using a controlled release system based on single protein nanocapsules previously developed in our laboratory^{148, 149}. Nanocapsules are formed through in situ radical polymerization of acrylate and acrylamide containing monomers and peptide crosslinkers around a protein core (Figure 4.9e). The final product is a protein complex in which the protein is surrounded by a hydrated protease-degradable polymeric shell. By changing the amino acids in the peptide crosslinker from L enantiomer to D enantiomer, the kinetics of enzymatic cleavage are modulated to control the release rate of VEGF over time. We have previously shown that by mixing fast and slow degrading nanocapsules we can achieve a release rate that can promote vascularization in skin and brain leading to enhanced wound closure^{148, 150}. Here we utilized nanocapsules crosslinked by the plasmin-degradable peptide KNRVK. We synthesized four different VEGF nanocapsules containing 100% L, 75% L, 50% L or 25% L crosslinker (Figure 4.9e) and mixed them at equal amounts to achieve sustained VEGF release. Hydrogels containing none or 10 μ M fibronectin fragments (this amount has been shown to sufficiently promote cell spreading in HA hydrogel *in vitro*, Figure 4.9f), 200ng VEGF nanocapsules, and having a storage modulus of 350Pa were implanted subcutaneously (Figure 4.9g,h). Evaluation of isolectin perfused whole mount sections was performed 14-days after implantation on light sheet microscopy (Figure 4.10a) and confocal microscopy. HA hydrogels that do not contain fibronectin fragments (blk) resulted in the least vessel sprouting on the hydrogel surface and vessel infiltration within the hydrogel compared with fragment conditions even with the presence of VEGF nanocapsules,

demonstrating that integrin binding is essential for angiogenesis to occur *in vivo* (Figure 4.10b). HA hydrogels modified with either fibronectin fragment supported an angiogenic response; however, the morphology of the vessels on the gel surfaces was significantly different. The $\alpha3/\alpha5\beta1$ specific HA gels (Fn9*10 immobilized) displayed non-tortuous vessels displaying similar features as the normal mouse vasculature (control) while $\alpha\nu\beta3$ specific gels displayed tortuous and unorganized vessels that appeared to clump with one another (Figure 4.11a-c). Also, vessel distribution analysis also indicated a more space-filling vasculature on $\alpha5\beta1$ specific gel surface compared with $\alpha\nu\beta3$ -specific gels (Figure 4.11d). While vessels on $\alpha5\beta1$ specific gel surfaces presented organized and even vessel distribution like the blank gel control, vessels on $\alpha\nu\beta3$ specific gel surfaces yields uneven distribution, which originated from regional tortuous and unorganized vessel clumps (Figure 4.11d).

Next, light sheet fluorescent microscopy was used for large-scale whole-mount gel scan (approximately 8mm in diameter, 3mm in thickness) in order to evaluate the penetration of vessels (Figure 4.10a,b). Through the 3D heat map view, we were able to visualize vessel penetration starting from the gel surface (Figure 4.10c). Projection view was later acquired via dividing whole-scanned 3D gel structure into 100um thickness slices and performing maximum intensity projection. This helped us visualize the penetrating vessels. As expected, clear vessel infiltration was observed in both $\alpha3/\alpha5\beta1$ specific and $\alpha\nu\beta3$ -specific gels (Figure 4.10d).

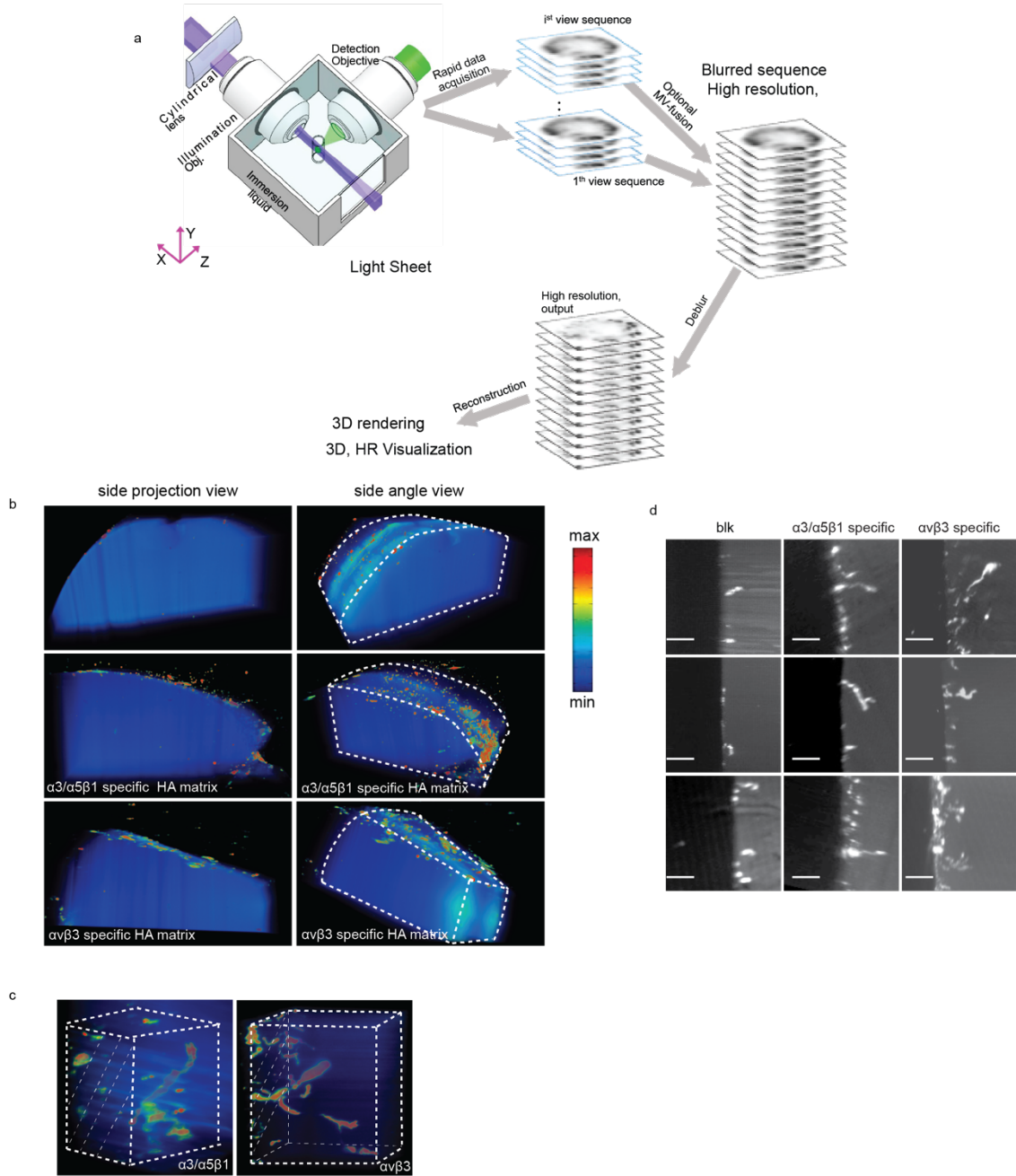


Figure 4.10 (a) Schematic for light sheet microscopy detection system. (b) Bulk 3D visualization of isolectin-labeled vessel on the surface and inside of blank, $\alpha3/\alpha5\beta1$ specific, $\alpha\nu\beta3$ specific HA matrices (labeled as blue) after 14 days in vivo. (c) Zoom-in 3D heat map for vessel penetration visualization (HA matrices were labeled as blue). (d) Projection view for vessel penetration within blank, $\alpha3/\alpha5\beta1$ specific and $\alpha\nu\beta3$ specific matrices after 2 weeks in vivo. Scale bar: 100 μm .

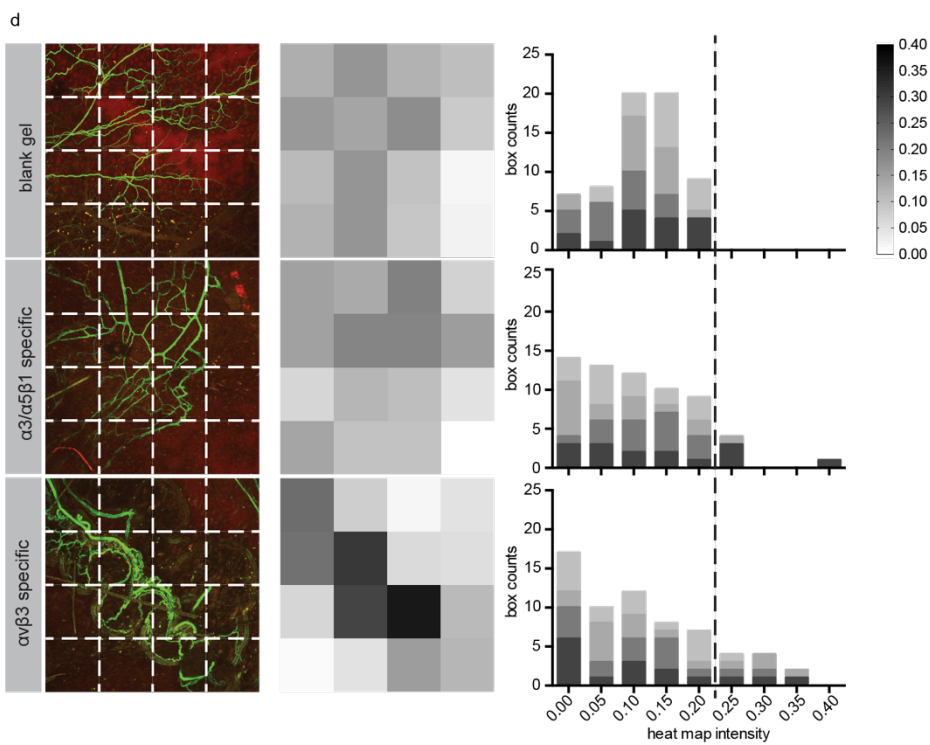
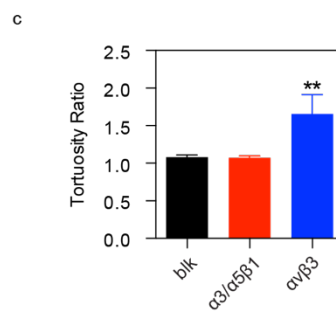
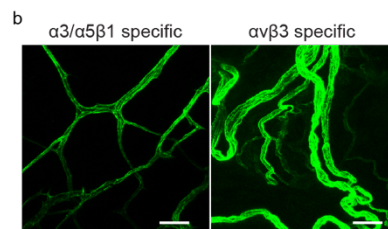
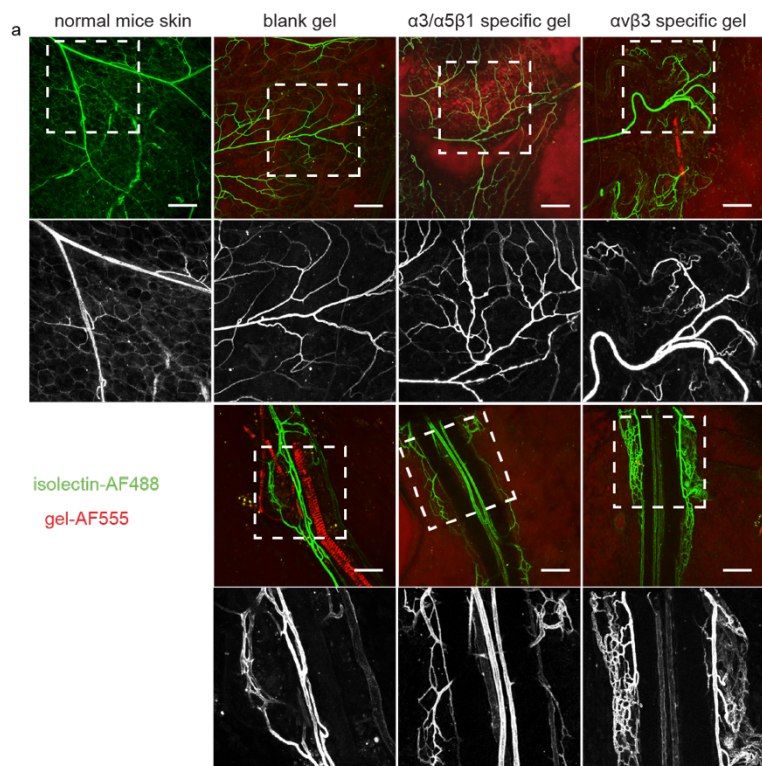


Figure 4.11A modified matrigel plug assay using bioengineered hyaluronic acid (HA) hydrogels is utilized to assess angiogenesis in mice. (a) Comparison of normal mice skin vessel morphologies with the morphologies of infiltrated vessels on the surfaces of implanted blank, $\alpha3/\alpha5\beta1$ specific (10 μ M Fn9*10) and $\alpha v\beta3$ specific (10 μ M Fn9*10) HA hydrogels with VEGF nanocapsules (200ng per gel) 2 weeks after implantation. Scale bar: 200 μ m. (b) Representative 40x images of vessels on the surface of $\alpha3/\alpha5\beta1$ specific and $\alpha v\beta3$ specific HA matrices. Scale bar: 50 μ m. (c) Vessel totuosity comparison among blank, $\alpha3/\alpha5\beta1$ specific and $\alpha v\beta3$ specific conditions (n = 4 individual implants). (d) Heat map analysis of vessel distribution on the surfaces of blank, $\alpha3/\alpha5\beta1$ specific and $\alpha v\beta3$ specific matrices (n=4 individual implants). Darker box indicates higher vessel density in that region while white indicates the absence of vessels. Plot represents mean \pm SD.** indicate P < 0.01.

4.3.7 $\alpha3/\alpha5\beta1$ integrin binding reduces VEGF induced vascular permeability after stroke

VEGF is the key regulator of angiogenesis and it has been widely investigated in clinical and preclinical models to promote perfusion in various organ systems¹⁵¹⁻¹⁵⁴. However, VEGF has been plagued with negative clinical trials showing little therapeutic benefit at safe doses¹⁵⁵⁻¹⁵⁸ and the generation of a leaky and immature vasculature^{159, 160}. Thus, effective VEGF delivery is a holy grail in the field of therapeutic angiogenesis. In the brain, VEGF is one of the essential molecules in normal post-stroke angiogenesis¹⁶¹; however, the delivery of VEGF after stroke has been complicated by the induction of a disordered and permeable vasculature^{162, 163}. Thus, we next sought to evaluate the angiogenic response of integrin stimulation on VEGF-induced angiogenesis in a murine model of brain stroke. Staining of stroke site has revealed increased expression of ECM protein such as fibronectin (Figure 4.12a and Figure 4.13a). We believe that by utilizing integrin specific implants, the micro-ECM environment at the stroke site could be modulated to promote therapeutic outcomes. Adult mice were submitted to a cerebral artery occlusion (MCAo) and transplanted 5 days later with a 350Pa HA-RGD hydrogel containing 200ng of VEGF nanocapsules and 10 μ M fibronectin fragments (nV+Fn9(4G)10 and nV+Fn9*10 directly into the stroke cavity (Figure 4.12b). Animal control groups were transplanted with either HA-RGD hydrogel alone (RGD), HA hydrogel containing soluble VEGF and RGD (Vs+RGD) or the star fragment (Vs+ Fn9*10) or nothing (No gel). Ten days post-transplantation, animals injected with fibronectin fragment containing hydrogels were perfused

with tomato lectin before sacrifice for the purpose of studying perfused vessel morphology while other animals were directly perfused with 4% PFA and sacrificed.

Sections were all stained for Glut-1, a glucose transporter expressed on brain endothelial cells and the positively stained vascular area was quantified in both the infarct and peri-infarct areas (Figure 4.12c). To compare the vascular bed in all conditions, both Glut-1 stained only and Glut-1 plus tomato lectin stained in tomato lectin-perfused animals were quantified. Glut-1 stained for all vessels while tomato lectin only stained for perfused vessels. Tomato lectin alters Glut-1 staining such that in tomato lectin-perfused animals the combination of both stains reveals the vascular bed the same as Glut-1 alone in tomato lectin-unperfused animals (Figure 4.13b). As expected, all the VEGF containing hydrogels showed a greater vasculature area percentage than RGD only gels in the infarct and the peri-infarct regions. However, we found that the vascular area was significantly increased in the nV+star ($\alpha3/\alpha5\beta1$ specific) condition compared with any other group in both regions (Figure 4.12d, e), suggesting a strong role of activated $\alpha3/\alpha5\beta1$ integrin binding in promoting the angiogenesis process. The significantly increased vessel area percentage of nV+ Fn9*10 when comparing with Vs+ Fn9*10 condition in both areas also verified the greater therapeutic effects from VEGF nanocapsules.

In order to evaluate the quality of these newly formed vascular network, both their permeability and structure were studied. For this, Ter-119, a red blood cell marker, was fluorescently stained and quantified in terms of positive area in the stroke regions (Figure 4.12c). The results showed a significantly reduced positive area for Ter-119 in the nV+ Fn9*10 condition compared with the nV+Fn9(4G)10 group, suggesting a beneficial effect of the activation of $\alpha3/\alpha5\beta1$ in promoting vascular permeability and stability while reducing blood leakage (Figure 4.12f). In addition, the morphoanalysis of tomato lectin-perfused vessels was performed by quantifying the number of vascular ramification growing out of a common vascular tree (Figure 4.12b). We found that the number of ramification per mm^2 was significantly greater

in the nV+star condition compared with the nV+4G group, indicating that stimulating $\alpha3/\alpha5\beta1$ integrin activation also promotes the formation of a physiological vascular architecture around stroke site (Figure 4.12g).

These results demonstrate for the first time that the therapeutic effect of VEGF on post-stroke angiogenesis can be regulated by the specific integrin stimulation, influencing not only the intensity of the vascular growth but also its vascular patterning and quality.

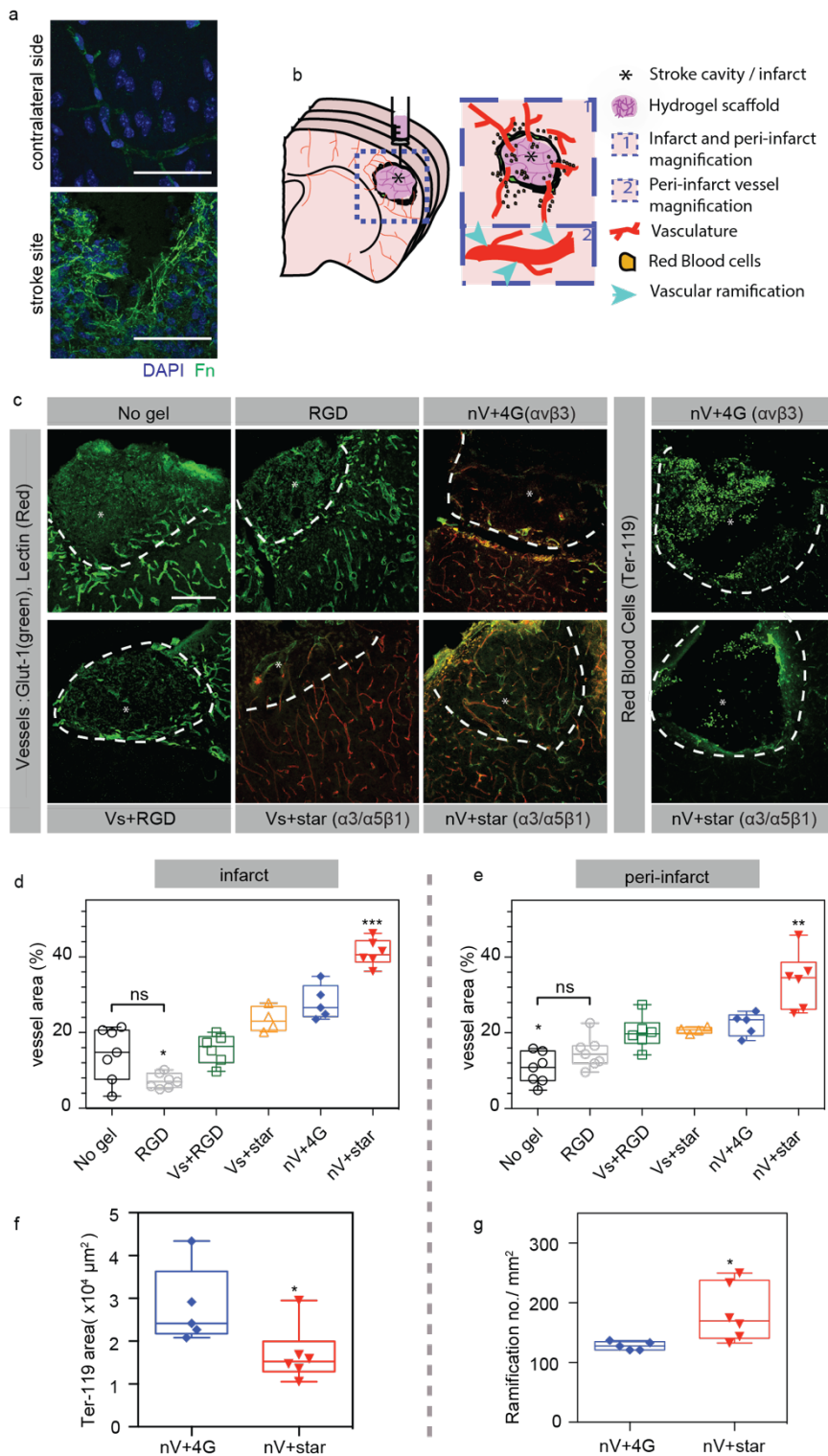


Figure 4.12An middle cerebral artery occlusion (MCAO) ischemic stroke model was utilized to look at the effects of injected integrin-specific HA matrices on stroke repair 10 days post-injection (injection was performed 5 days post stroke). (a) Fibronectin(Fn) immunofluorescence staining on stroke site and cotralateral side of mouse brain 15 days post stroke showed enhanced Fn signals around stroke site. (b)

Schematic illustration of mouse brain coronal sections showing a cortical stroke and the transplantation of an injectable hyaluronic acid (HA) hydrogel within the damaged area represented by the asterisk. In order to protect the healthy parenchyma from nearby lesion area, star-shaped glial cells, astrocytes, elongate and surround the damaged site, forming the astrocytic scar. This stroke cavity is situated directly adjacent to the region of the brain that undergoes the most substantial repair and recovery, the peri-infarct tissue, where new structures such as vessels develop and infiltrate the infarct while undergoing a drastic remodeling process. The growing vasculature structure and permeability are both associated with tissue repair. (c) Fluorescent microscopy showing brain vasculature in both the infarct and peri-infarct (stained for Glut-1 or Glut-1 plus tomato lectin intravascular perfusion) as well as leaked red blood cells (stained for Ter-119) in the no gel, 500 μ M RGD, 200ng soluble VEGF(Vs) + 500 μ M RGD, 200 ng Vs+ 10 μ M 9*10, 200ng VEGF nanocapsules (nV) + 10 μ M 9(4G)10 and 200ng nV + 10 μ M 9*10 conditions. VEGF nanocapsules were designed to slowly release VEGF. Scale bar: 100 μ m. (d,e) The results showed a significantly increased positive area for stained vessels in both the infarct and the per-infarct areas of nV+star transplanted mice compared with any other group. ** and *** indicate $P < 0.01$ and $P < 0.001$, respectively. (f) The measure of Ter-119 positive red blood cells in the two nV conditions show a significantly reduced area in the infarct site of nV+star ($\alpha 3/\alpha 5\beta 1$ specific matrices) transplanted mice compared with nV+4G ($\alpha v\beta 3$ specific matrices). This result shows that nV+star decreased leakiness of growing vessels in the stroke brain. * indicates $P < 0.05$. (g) The morphoanalysis of growing vessels in the peri-infarct area shows a significantly increased number of vascular ramifications in the nV+star condition compared with the nV+4G, suggesting that nV+star promotes a post-stroke vascular remodeling into a more physiological network. All plots represent mean \pm SD. * indicates $P < 0.05$.

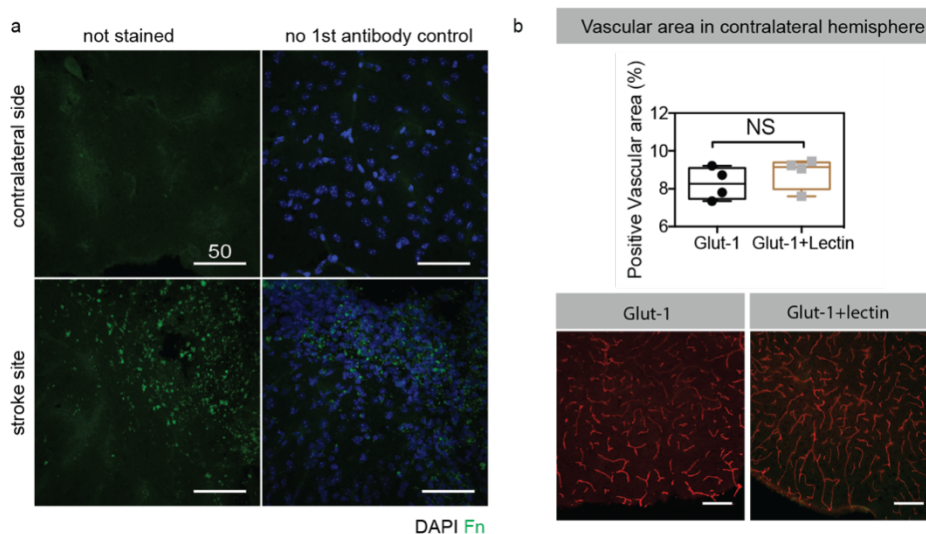


Figure 4.13 (a) Non-stained control and non-primary antibody control of Fibronectin(Fn) immunofluorescence staining on stroke site and cotralateral hemisphere of mouse brain 15 days post stroke. (b) Data presented here showed positively stained vessels of the contralateral hemisphere in both Glut-1 stained conditions or Glut1 plus tomato lectin perfused conditions. No significant difference was shown on positive vascular area percentage and vessel morphology between these two conditions. Scale bar: 100 μ m.

4.4 Conclusions

Integrin binding to bioengineered hydrogel scaffolds is essential for tissue regrowth and regeneration, yet not all integrin binding can lead to tissue repair. Vascular endothelial growth factor (VEGF) is known as the master regulator of angiogenesis. It contributes to vascular permeability at early stages of wound healing, promotes effective granulation formation and also correlates with scar tissue formation at the final stages of wound healing. Acute tissue damage such as brain stroke requires the formation of a mature and organized vasculature induced by VEGF to initiate the recruitment of pro-repair cells and promote tissue regeneration. The vascular remodeling that follows the initial growth is essential for the newly formed vessels, initially permeable and tortuous, to mature into a functional network that can support tissue repair. Here we show that through engineering hydrogel materials to promote $\alpha3/\alpha5\beta1$ integrin binding with VEGF presence, we can promote the formation of a space filling and mature vasculature compared to hydrogel materials that promote a $\alpha v\beta3$ integrin binding. *In vitro*, $\alpha3/\alpha5\beta1$ scaffolds promoted endothelial cells to sprout and branch, forming organized extensive networks that eventually reached and anastomosed with neighboring branches. *In vivo*, $\alpha3/\alpha5\beta1$ scaffolds delivering vascular VEGF promoted non-tortuous blood vessel infiltration and non-leaky blood vessels by 10 days post stroke. In contrast, materials that promote $\alpha v\beta3$ integrin binding promoted endothelial sprout clumping *in vitro* and leaky vessels *in vivo*. This work shows that precisely controlled integrin activation from a biomaterial can be harnessed to direct therapeutic vessel regeneration and reduce VEGF induced vascular permeability *in vivo* (Figure 4.14).

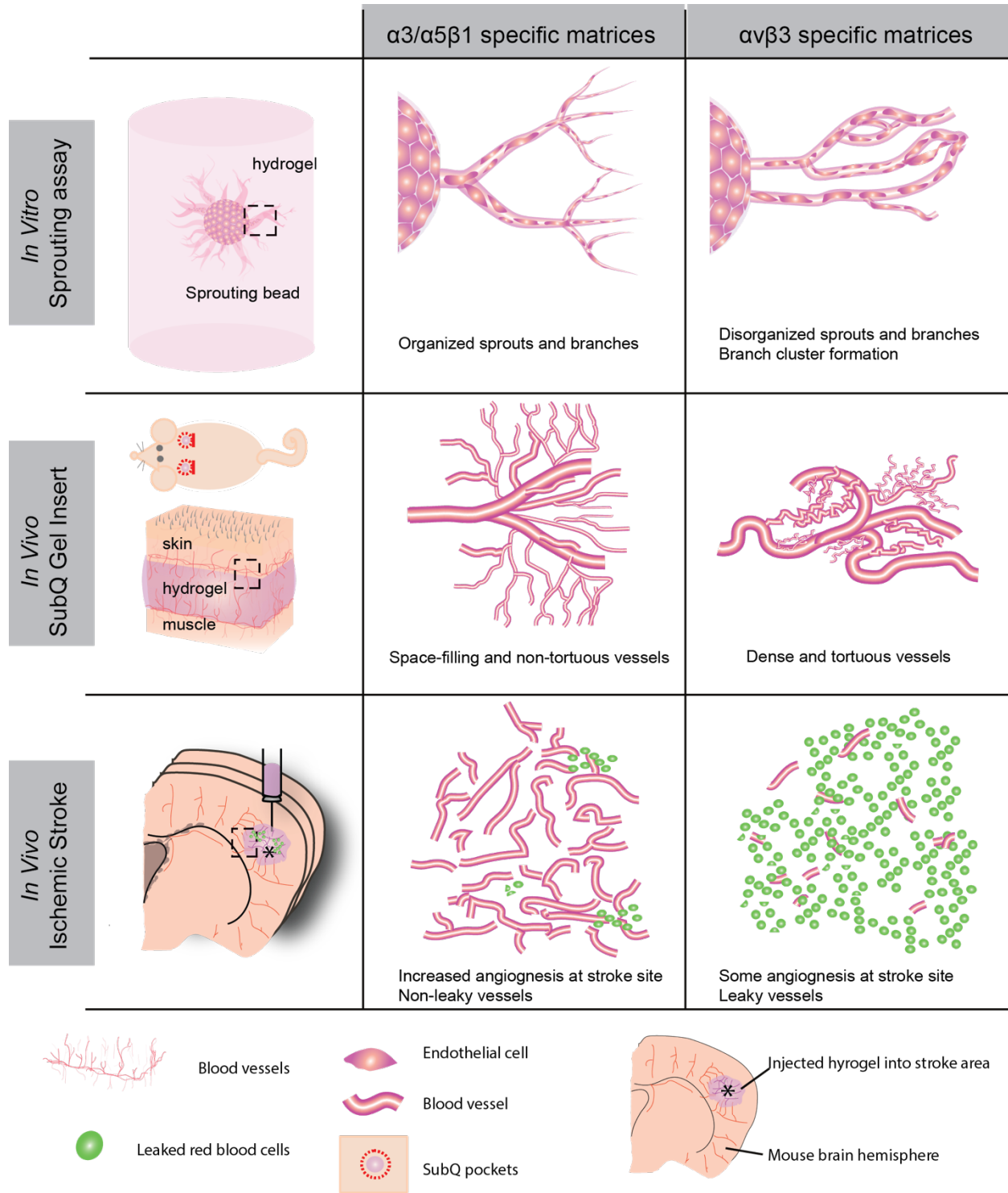


Figure 4.14 Summary figure for in vitro sprouting assay, in vivo subcutaneous modified matrigel assay and in vivo ischemic stroke model. In conclusion, $\alpha3/\alpha5\beta1$ and $\alpha v\beta3$ integrin-specific materials regulate angiogenesis process differently both in vitro and in vivo. $\alpha3/\alpha5\beta1$ specific materials affects vascular patterning in vivo by reducing vessel tortuosity and also promoting the development and maturation of newly formed vessels in the damaged brain, thus representing a promising candidate in the design of therapeutic pro-angiogenic scaffolds.

Integrin binding is a fundamental design parameter for engineering matrices for tissue repair and regeneration. The incorporation of integrin binding molecules within engineered matrices ranges from peptides such as RGD¹¹⁷, to protein fragments¹¹⁸, and natural proteins¹¹⁹, with the primary purpose to promote cell spreading and migration within these matrices. However, integrin binding ligands are often overlooked as bioactive cues, capable of dictating morphogenesis and guiding tissue repair. Our work shows that integrin stimulation from engineered matrices is a morphogenic signal that can be harnessed to generate either a normal vasculature or a diseased vasculature depending on the integrin being engaged (Figure 4.14). In the work presented here, we establish an integrin-specific material platform via the immobilization of fibronectin derived protein fragments to fibrin or hyaluronic acid matrices to induce specific $\alpha3/\alpha5\beta1$ or $\alpha v\beta3$ integrin activation. We found that $\alpha3/\alpha5\beta1$ and $\alpha v\beta3$ integrin-specific materials regulate vascular patterning. $\alpha v\beta3$ integrin-specific materials lead to pathological tumor-like sprouting clumps, which can later be rescued by the blockage of αv integrin. $\alpha3/\alpha5\beta1$ integrin-specific materials lead to a space filling vasculature that has reduced vessel tortuosity and promotes the development and maturation of newly formed vessels in the damaged brain, thus representing a promising candidate in the design of therapeutic pro-angiogenic scaffolds.

Chapter 5

VEGF clusters improve diabetic skin wound healing

5.1 Introduction

An estimated 3 to 6 million chronic skin ulcers occur in patients every year in the United States^{164, 165}, among which, diabetic foot ulcers (DFUs) have become one of the most common and severe complications of diabetes. It is known that DFUs are now the leading cause for hospitalization in patients with diabetes and also the presence of an ulcer may increase the risk of lower-extremity amputation by almost six folds, affecting Diabetic patients' quality of lives, hospital stay and survival rate¹⁶⁶⁻¹⁶⁹. The severity of DFUs is due to the impairment of numerous components of wound healing in diabetic patients¹⁷⁰, including hemostasis and inflammation, matrix deposition, and angiogenesis. These impairments are present in a wide variety of tissues including myocardium, skeletal muscle, nerve, and skin. Specifically, cutaneous wounds in diabetics have exhibited altered blood flow, impaired neutrophil anti-microbial activity, and also dysfunctional inflammatory state associated with abnormal chemokine expression¹⁷¹. Compared with healing through contraction, as occurs in normal wounds, diabetic wounds tend to heal by cellular infiltration, deposition of granulation tissue, and re-epithelialization. This process is common to the healing of chronic ulcers in patients with diabetes decubitus ulcers, and venous stasis¹⁷².

As the master regulator of angiogenesis, Vascular endothelial growth factor (VEGF) is not only crucial for vascular development during embryogenesis^{173, 174}, but also is required for the homeostasis of blood vessels in adult¹⁷⁵. Increasing evidence suggest that the relatively low level of VEGF in diabetic wounds is responsible for the impaired healing process in these

patients¹⁷⁶. While the basal level of VEGF is increased in un-wounded skin of *db/db* mice, the VEGF level comes with a significant delay after wounds occur. In full-thickness diabetic excisional wound, VEGF levels initially increase but eventually decrease to undetectable levels by day 5. In comparison, VEGF peaks in nondiabetic normal tissue and granulation tissue is accumulating at the same time points¹⁷⁷. Thus, VEGF is a potential agent that helps promoting diabetic wound healing.

However, as a paracrine endothelial cell mitogen, a chemotactic agent, and an inducer of both vascular and skin permeability¹⁷⁸⁻¹⁸², VEGF has been plagued with negative clinical trials showing little therapeutic benefit at safe doses¹⁵⁵⁻¹⁵⁸ and the generation of a leaky and immature vasculature^{159, 160}. Topical VEGF application (20µg every other day) on *db/db* cutaneous wounds showed accelerate wound healing despite the induction of disordered vasculature¹⁷⁰. Clinical trials have also been performed using topical recombinant human VEGF on diabetic foot ulcers; however, even though positive trends such as epithelialization stimulation and collagen production were seen, no published information is available beyond these phase I studies¹⁸³.

Despite the fact that soluble VEGF alone doesn't result in a healthy vascular network formation and requires microenvironment dosage control¹⁸⁴, experimental studies have shown that sustained⁷⁴, immobilized VEGF promotes angiogenesis and the formation of healthy vessels^{44, 185}. Thus, it is crucial to utilize different presentation of VEGF to promote diabetic wound healing. Our lab previously showed that VEGF clusters with polystyrene bead core increased endothelial tube branch points compared with covalently-linked VEGF and soluble VEGF¹⁰⁶. Based on the previous work, two different types of new heparin-based VEGF clusters, highly clustered VEGF (hcV) and lowly clustered VEGF (lcV) were synthesized and applied on diabetic cutaneous wounds with one-time small dosage (200ng per wound). Highly clustered VEGF (hcV) were shown to effectively reduce wound size, encourage re-epithelialization and

promote endothelial cell/pericyte recruitment after 7 days while IcV didn't. This present work shows that small dosage of highly clustered VEGF can be utilized as an effective agent to promote diabetic cutaneous wound healing.

5.2 Materials and methods

5.2.1 Synthesis of VEGF clusters

Heparin was first modified with p-azidobenzyl hydrazide (ABH, Pierce, Rockford, IL) through EDC mediated conjugation in a 1:3 molar ratio of ABH to available carboxylic acids. The pH was monitored during the course of the reaction and the conjugation took place at pH 4.75 in PBS. After 2 h of reaction at room temperature, the carboxylic acid groups on heparin were reactivated with EDC, but this time reacted with adipic dihydrazide (ADH) in 27 molar excess in order to saturate reaction binding sites and prevent unwanted crosslinking. Again, the reaction pH was monitored at pH 4.75 in PBS. This reaction was allowed to proceed overnight at room temperature, at which point the reaction solution was dialyzed against DI water. The dialysis units were then placed in PBS at pH 7.4 for buffer exchange. Heparin with ABH and ADH was then reacted with NHS-acrylate to convert the amine groups to acrylates. The reaction proceeded overnight at room temperature, and then dialyzed again. After dialysis, the solution was lyophilized for two days. The powder was dissolved in sodium acetate, pH 4, at 100 mg/ml and combined with Tween-80 and Span-80 (8% HLB). The solution was placed in a ten-fold volume of hexane and combined with N,N,N',N'-tetramethyl-ethane-1,2-diamine (TEMED) and ammonium persulfate (APS) during sonication to initiate radical polymerization. The resultant nanoparticles were purified via liquid-liquid extraction in hexane. In the final stage of the extraction process, bubbling nitrogen gas into the nanoparticle solution evaporated off excess hexane. The particles were then dialyzed in 100 kD MWCO dialysis units for several days and stored until use. The amount of heparin in the solution was determined by lyophilizing a small aliquot of the solution. Similar to the heparin-coated polystyrene particles, VEGF was incubated

at 4°C at 100 mg/ ml, followed by 365 nm wavelength UV light activation for 10 min to lock VEGF covalently to the surface. Excess VEGF was removed by dialysis in 100 kD MWCO dialysis units.

5.2.2 Excisional skin wound model

Seven to nine week old female db/db mice were used for these studies under the ACR protocol #2010-011. Mice were anesthetized with 2–3% isoflurane in an induction chamber and kept under anesthesia during the whole surgery. The back of the mice was shaved, washed with betadine and 70% ethanol and a dose of buprenorphine (2.5 mg/kg) was administered, subcutaneously, prior to the surgery. Four excisional wounds were made in the skin aside the midline of the animal using a 6-mm biopsy punch. 40 µl of Fib3+hcV (200ng), Fib3+IcV(200ng), Fib3+Vs(200ng) or Fib3 gel alone was applied topically on the wounds and wait for gelation for 20 minutes. The whole backs were covered with tegerderm to allow visualization and measurement of the wound size. All animals were observed daily for signs of inflammation and pain for the first 48 hours post-surgery. Wounds were photographed at day 0 and day 7, based on which the percentages of wound closure were calculated.

5.2.3 Histological Analyses

All animals were sacrificed at day 7 with isoflurane overdose. Four 8-mm round pieces of tissue were collected from each db/db mouse containing the whole wound area and the surrounding tissue and skin, cut precisely in half at the midline of the wound. Half of the tissues were fixed in 1% Paraformaldehyde (PFA) for 16-18 hrs at 4 °C, then preserved in 70% EtOH, and then paraffin embedded while the corresponding halves were cyro-embedded in OCT right after sacrifice. Paraffin sections were cut at 5 µm and the H&E stainings were performed. HALO

Next Generation Imaging analysis software (Indica Labs; Corrales, NM) was then used to analyze the images.

5.2.4 Immunofluorescent Staining and Analyses

For cryo-embedded samples, 25 μ m thickness sample slices were cut, fixed in ice-cold acetone for 5 min, washed with 1XPBS for 5 min before blocked for 1 hr at room temperature in blocking buffer: 1XPBS + 0.05% Tween-20 + 5% normal goat serum. Sections are then washed in 1XPBST. Primary antibodies were prepared in blocking buffer, including rabbit anti-mouse Keratin 14 (Biolegend; #905301; 1:200), rat anti-mouse CD31 (BD Pharmingen; #553370; 1:100), and rabbit anti-mouse NG2(Millipore; #AB5320; 1:200). Sections were stained with primary antibodies overnight, then were washed with 1XPBST twice, then re-incubated with blocking buffer for 10 min before secondary antibody incubation. Secondary antibodies were all prepared at a dilution of 1:200 in blocking buffer together with 2 μ g/mL DAPI. Sections were then incubated in secondary antibodies for 2 hours at room temperature, and subsequently washed with 1X PBST and 1XPBS. Sections were mounted in Antifade Gold mounting medium. Imaging was performed using a Nikon C2 confocal and images were analyzed using Image J.

5.2.5 Statistical Analysis

Statistical analyses were performed using Prism (GraphPad, San Diego, CA). Data were analyzed using a one-way analysis of variance (ANOVA) followed by a Tukey post-hoc test. The results are expressed as mean \pm SD.

Single, double, triple and quadruple asterisks represent $p < 0.05$, $p < 0.01$, $p < 0.001$ and $p < 0.0001$, respectively. A p value < 0.05 was considered statistically significant.

5.3 Results and discussion

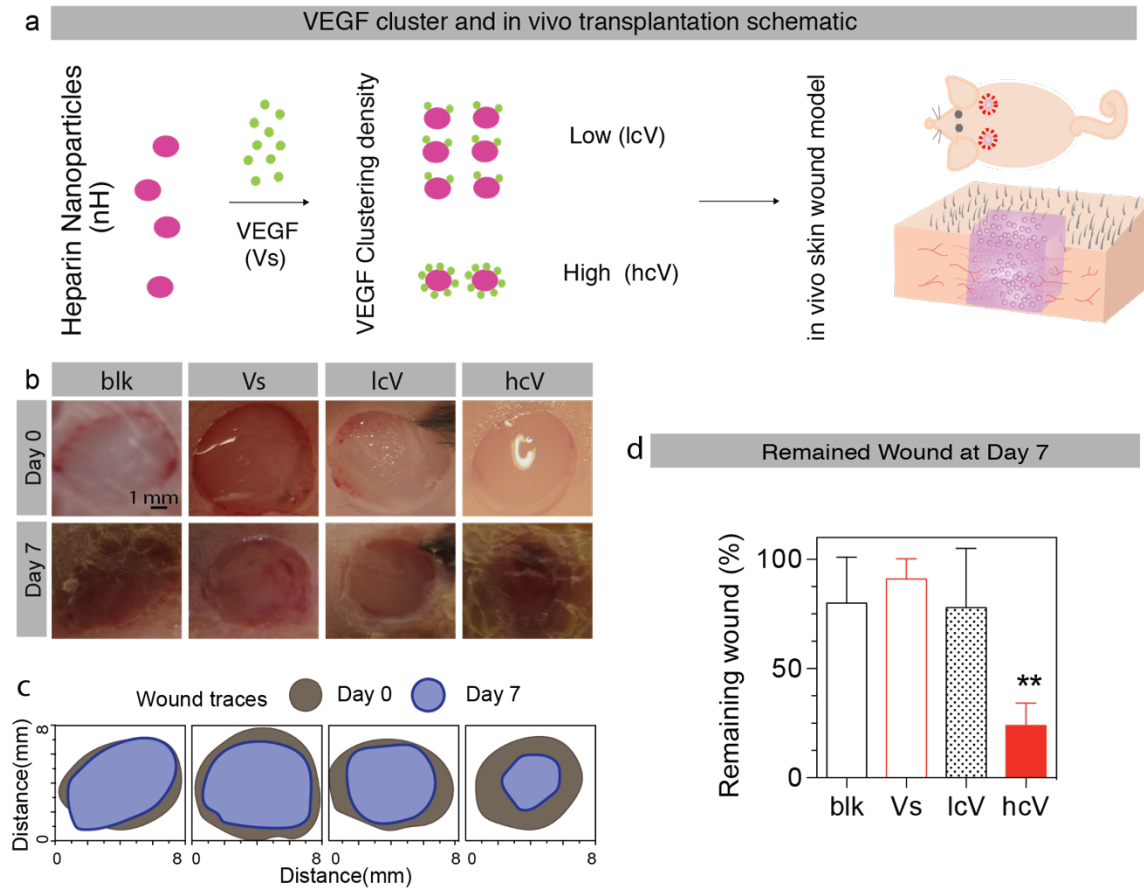


Figure 5.1 (a) Scheme for heparin nanoparticles and VEGF clusters synthesis. (b) *Db/db* mice skin wounds were induced at day 0. Mice were sacrificed at day 7 and wound images were taken and analyzed for blank fibrin gel (blk), soluble VEGF + gel(Vs), low clustered VEGF (lcV) and high clustered VEGF (hcV) conditions. Scale bar, 1mm. (c) Traces of wound-bed closure during seven days in vivo for each treatment category. (d) Quantification of the percentage of the remained wounds at day 7 (n=3-4). ** indicates $P < 0.01$.

It is known that vascular growth is essential for effective tissue repair and is profoundly attenuated in preclinical models of impaired healing such as diabetic mice. To understand how VEGF clustering affects diabetic wound healing outcomes, an excisional skin wound model was used to assess angiogenesis in diabetic (*db/db*) mice. Two types of heparin-core VEGF clusters with 100-fold difference of bound-VEGF density (20mg VEGF/mg heparin and 0.2mg VEGF/mg heparin) were synthesized as previously described (Nih L et al, in preparation), and encapsulated in a hydrogel prior to administration(Figure6.1a). In order to maintain accurate

dosage locally on the wound beds, fibrin gel depleted of fibronectin was used as a fast-degradable carrier for these VEGF clusters. Fibrin matrix is known for its biocompatibility and safety for usage in human studies¹⁸⁶. The gelation process is also fast, stable and easy to be induced through Factor XIII reaction. Full thickness excision of 6-mm circle skin wounds were created on the back of diabetic mice at day 0 and the wounds were covered with one local dosage of 40µl fibrin matrix alone (blk) or fibrin matrices containing 200ng VEGF per gel in the format of lowly clustered VEGF (lcV) or highly clustered VEGF (hcV) or soluble VEGF (Vs). At day 7, mice were sacrificed and significant increased wound closure was observed visually in hcV condition compared with all the other three groups. Consistently, quantification of wound closure also showed that hcV condition reduced wound size significantly when compared with blk, Vs and lcV conditions (Figure 6.1b-d).

8-mm circular pieces of mice skin covering the whole wound area and the surrounding tissue were collected using biopsy punch. The samples were then cut precisely in half at the midline of the wound. Halves of the wounds were fixed for paraffin embedding and the other halves were cryo-embedded right after sacrifice.

As expected, the analysis of H&E stained paraffin sections showed that the fibrin matrix was completely resolved 7 days after injury (Figure 6.2a). Since the wound area created by the surgical incision was clean and uninfected in diabetic mouse, the epithelial regeneration predominates over fibrosis with minimal wound contraction, with a predominant migration of neutrophils toward the central wound area, and basal cells at the cut edge of the epidermis showing increased mitotic activity. In the blank treated group (blk), epithelia cells from both edges migrated to the center of the wound and proliferated along the dermis, but no continuous epithelia layer was observed. Similar morphological features were seen in the Vs-treated group, where neutrophilia were still predominant while the monocytes and granulation tissues extended into the fibrin clot and filled the wound gaps. However, no continuous regenerated epithelia

layer was observed. In the lcV-treated group, no granulation tissue was filled into the wound area except in the margins.

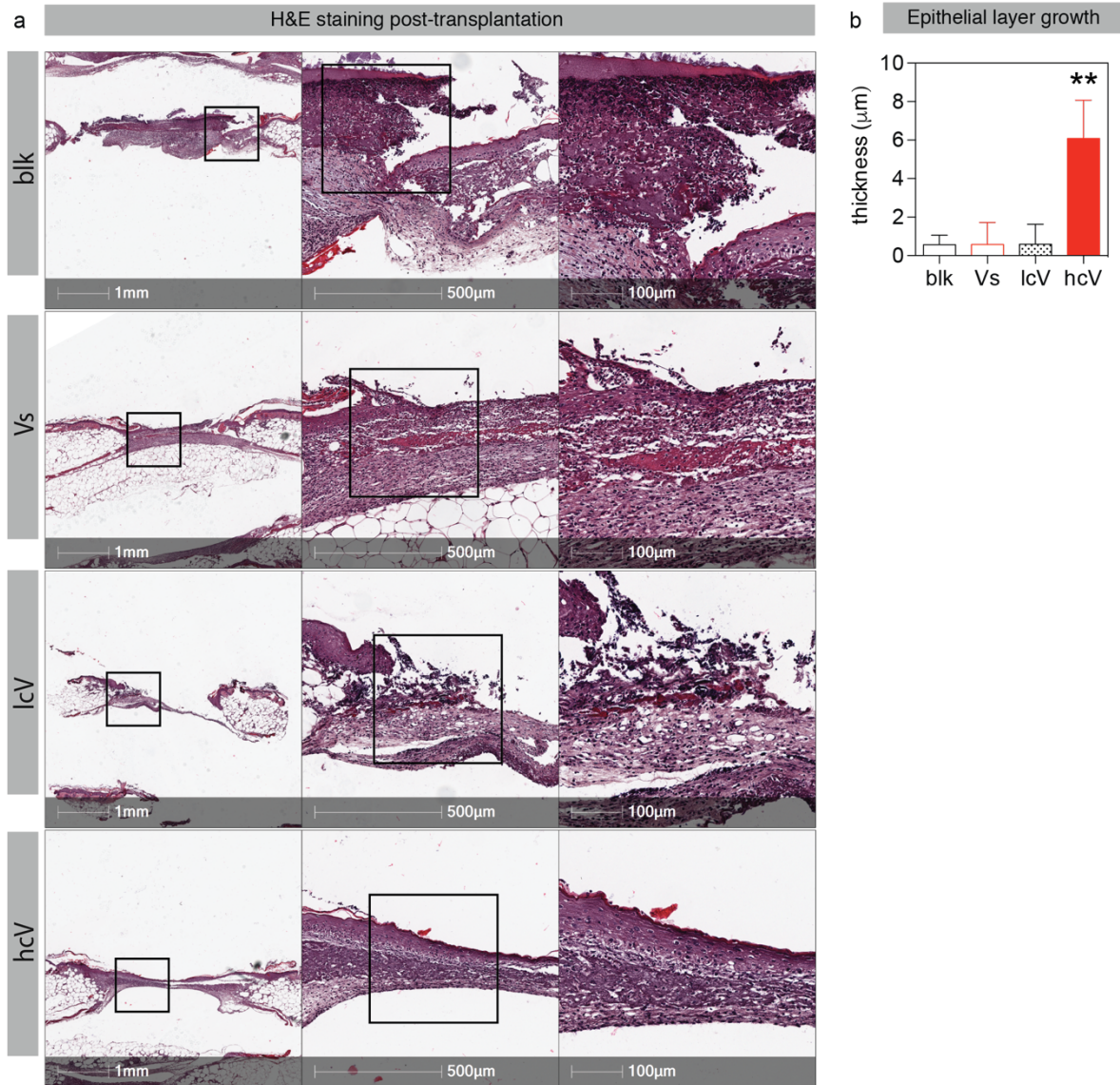


Figure 5.2 (a) Day 7 H&E representative images for blank fibrin gel (blk), soluble VEGF + gel(Vs), low clustered VEGF (lcV) and high clustered VEGF (hcV) conditions. Under blk condition, predominated neutrophils concentrated in the edges of the wound area, basal cells at the cut edges of the epidermis show increased mitotic activities, no regenerated epithelium formed and granulation tissue beneath the fibrin clot to fill the open wound area. Under Vs condition, neutrophils are still majority of inflammation cells that covered the surface of epidermis gap, fibrin clot deposited in the dermis are partially replaced by neutrophils and monocytes, still no regenerated epithelium was yielded. Under lcV condition, wound space is wide open and no granulation tissue filled into the wound area except in the margin. A thin layer of base membrane with scattered neutrophils and monocytes continuously grows to cover the base of

wound area. Under hcV condition, neovascularization begins emerge, collagen fibrin begins to bridge the wound area with increased fibroblast. A continuous layer of regenerated epithelium is formed and covers the whole wound area. (b) Comparison of epithelial layer thickness at day 7 (n=3-4, one way anova). ** indicates P < 0.01.

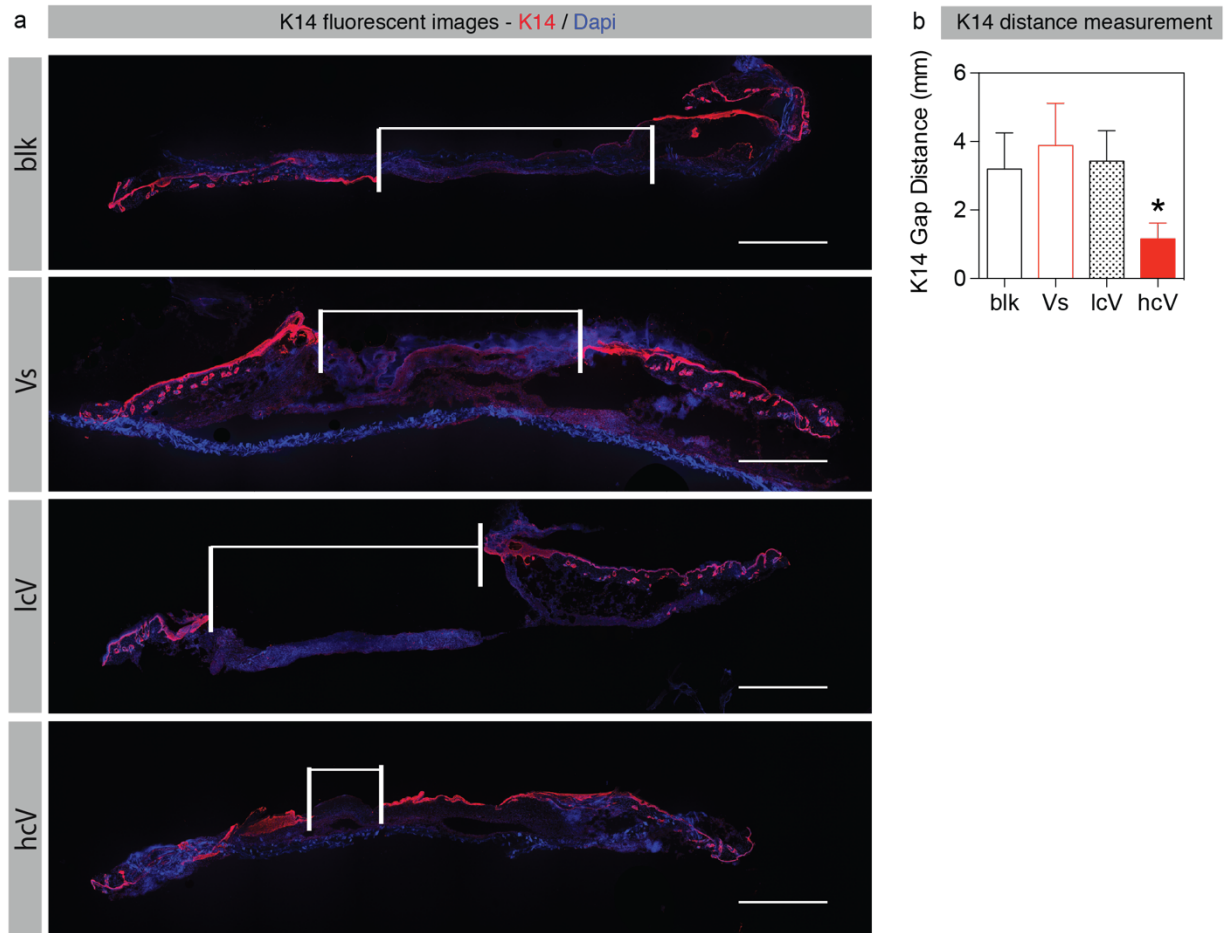


Figure 5.3(a) Full-scan K14 immunofluorescent representative images for blank fibrin gel (blk), soluble VEGF + gel(Vs), low clustered VEGF (lcV) and high clustered VEGF (hcV) conditions. Scale bar, 1mm.(b) Quantification of K14 staining gap distance at day 7 (n=3-4, one way anova). * indicates P < 0.05.

Interestingly, a neovascularization was observed in the hcV-treated group, where a majority of neutrophilia and fibrin clot were replaced by fibroblasts, macrophages and granulation tissue that filled the wound space. In this group, a thin layer of epidermal re-epithelialization covering the entirely wound surface was observed. Re-epithelialization post-injury is an important factor for wound healing. This observation indicates that the administration of hcV induced the greatest number of epithelial cells migration to the wound bed and promoted

the wound healing process. The quantification of the epithelial layer thickness. showed that the hcV condition yielded the greatest value compared with the all other conditions (Figure 6.2a,b).

Cryo-sections were stained with K14 (a keratinocyte marker) to look at the keratinocyte layer gap at day 7. Consistently with the previous findings, the hcV condition significantly shortened the wound gap compared with blank gel, Vs and lcV conditions, confirming a significantly faster healing process (Figure 6.3a,b).

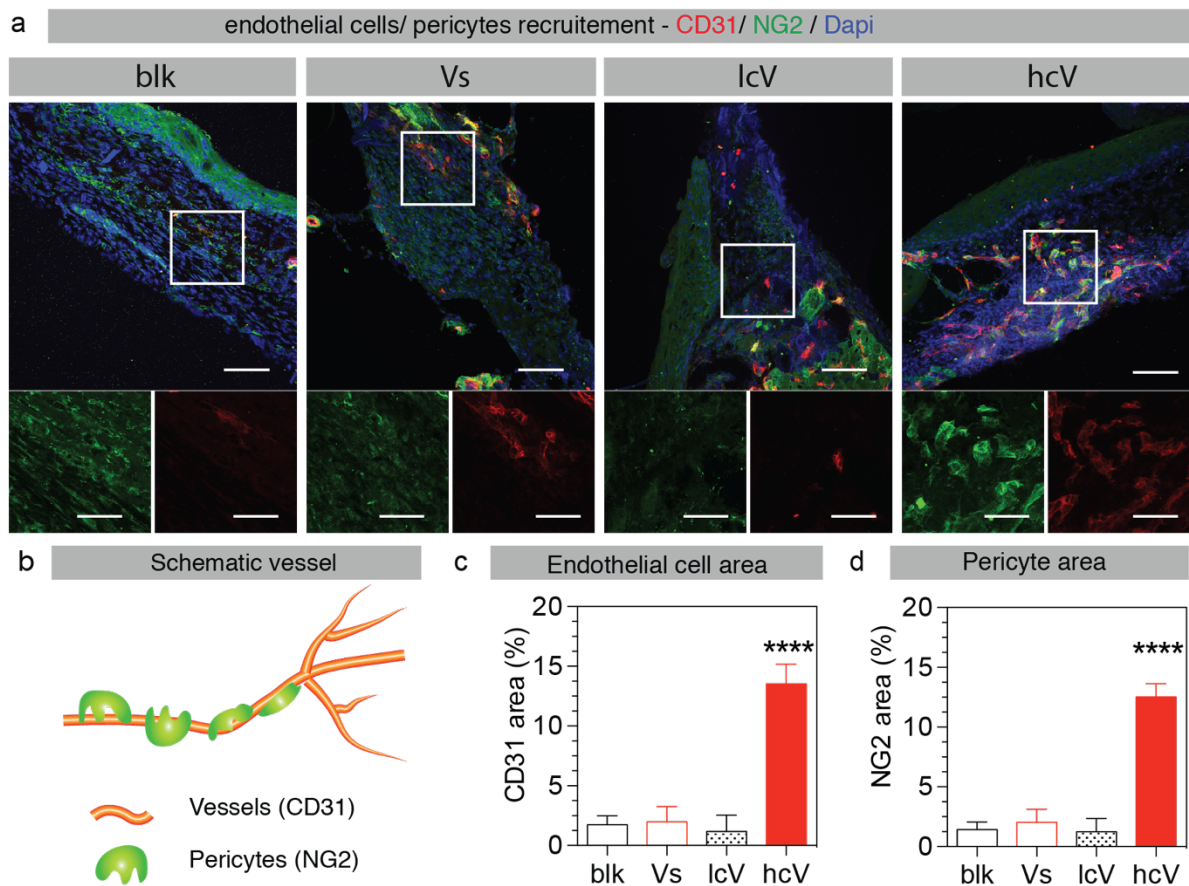


Figure 5.4 (a) Representative images for CD31 and NG2 immunofluorescent staining. Top row scale bar, 100µm. Bottom row scale bar, 50µm. (b) Schematic for endothelial cells (CD31) and pericytes (NG2) interaction. (c,d) Quantification of area percentage of CD31+ and NG2+ cells in granulation tissue at day 7 (n=3-4). **** indicates $P < 0.0001$.

To further examine the granulation tissue compositions and vessel formation on the wound bed, staining for endothelial cells (CD31) and pericytes (NG2) were performed on cryo-sections (Figure 6.4a,b). The granulation tissue was imaged and quantified for both markers.

The location of the granulation tissue was chosen at the margin of the wound bed. Quantitative analysis of vascular structures by CD31/NG2 double staining showed that the fibrin alone (blk), soluble VEGF (Vs) and low clustered VEGF (lcV) treatments had little effect on wound angiogenesis at day 7. In contrast, wounds treated with hcV showed a significantly increased density of both CD31+ and NG2+ cells at day 7, indicating a more advanced vascular formation in the wound site, associating the hcv administration to an advanced healing process (Figure 6.4c,d).

5.4 Conclusions

Vascular Endothelial Growth Factor (VEGF) has been utilized to promote vessel formation and wound healing in diabetic patients, yet no promising clinical outcomes were seen at safe dosage. Here we propose to use highly clustered VEGF (hcV) as a therapy for diabetic cutaneous wound. The application of small amount of hcV (200ng per 6-mm wound) promoted wound healing in *db/db* diabetic mice after 7 days post-surgery. The administration of hcV within a fibrin hydrogel directly at the wound sites showed the greatest extent of wound closure and re-epithelization compared with the administration of low clustered VEGF (lcV), soluble VEGF (Vs) or a blank hydrogel (blk) that does not contain the growth factor. Highly clustered VEGF (hcV) also promoted the formation of a granulation tissue and the recruitment of endothelial cells and pericytes to the wound bed. This work shows for the first time that small dosage of VEGF of controlled clustering density can be utilized as a therapy for diabetic wound healing. This work also provides a template for the design of future growth factor-based therapies in the field of tissue engineering.

In conclusion, we found that highly clustered VEGF (hcV) promoted a greater wound healing in diabetic mice at day 7 compared with soluble VEGF and low clustered VEGF. These results could be explained by the effect of hcV on the VEGF receptor 2 (VEGFR2) on endothelial cell surface. It is already known that different presentation of VEGF can lead to

different VEGFR2 pathway activation. For example, it was shown that the anchorage of VEGF to the extracellular matrix can convey differential signaling response to endothelial cells⁹⁹. It was also shown that when VEGF is covalently-immobilized to surface, VEGF internalization is not required for VEGF Receptor-2 phosphorylation¹⁸⁷. Specifically, in diabetic mice, cell surface abundance of VEGFR2 is reduced and VEGFR2 signaling pathway is ligand-independent¹⁸⁸. Our observations suggest that highly clustered VEGF promotes the activation of VEGFR2 differently, increasing the pro-repair angiogenesis in diabetic wound with trivial dosage. This finding could help with future presentation design of growth factors to achieve efficient wound healing.

Chapter 6

Ultra-large nano-patterned artificial surfaces for the study of distribution effects of bio cues such as VEGF

6.1 Introduction

Fabrication of nanopatterned gold slides

Current scheme: standard photolithography

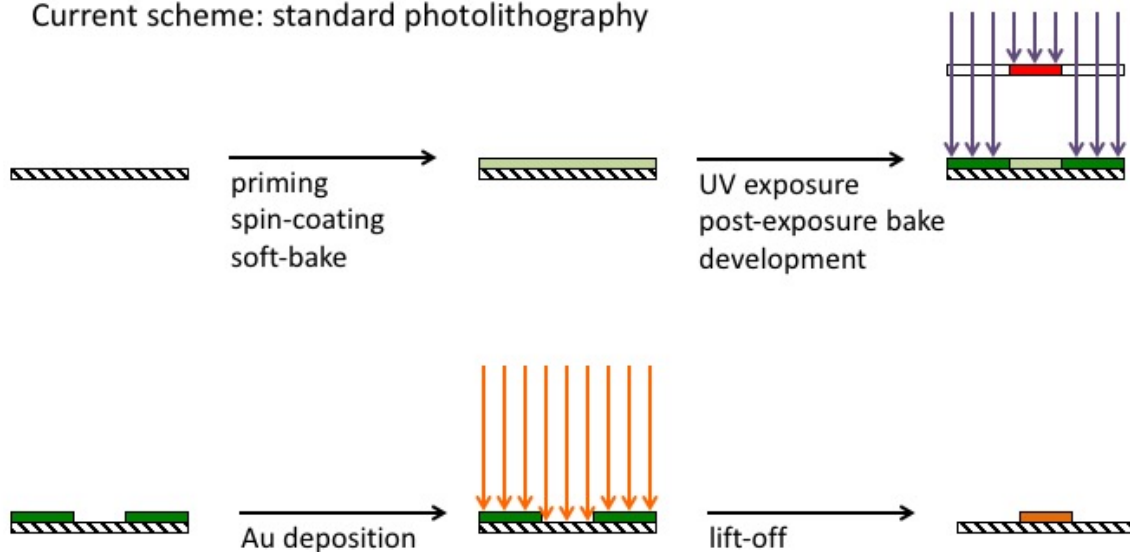


Figure 6.1 Schematic of the wafer fabrication process.

Here, we report a method of rapidly generating subcellular nano-scaled features on large glass wafers that can be easily accomplished within a day in batch. In addition, the wafer fabrication steps (Figure 6.1) were completely automated and can be readily scaled up. The product nano-features can then be used for Western Blots and qPCR for both protein and mRNA level of studies, especially for pathway activation studies from nano-patterned surfaces.

For common cellular response on nano-patterns, cells were always seeded on top of the generated surface to look at cellular responses, yet few studies have been done to really

understand the activation of biocue pathways, especially for covalently immobilized signals. The pathway activation from biocues normally happen within seconds or minutes after cellular contact with the biocues, thus requires precise engineering controls. Here, we combine the nano-pattern surface together with a cell sandwich method to look at the pathway activation from nano-patterned covalently-linked VEGF.

Besides the distribution of biocues, the amount of biocues is also important to understand the cellular outcomes. For example, surfaces loaded with different density of RGD can greatly impact cell adhesion and migration. Thus, besides precise distribution control, precise amount control is also needed to correlates cellular response with dosage. However, few methods are available to control protein amounts on nano-patterns. Here, we present a method to precisely control the amount of covalently-immobilized VEGF and observed different pathway response.

Last but not least, our method can later be combined with microprinting method to easily create mixtures of micro-patterns and nano-patterns to study complicated biocues. We believe this will be able to harness the therapeutic outcomes on implants.

Overall, we propose an ultra-large nano-islands surface production system, which can produce consistent nano-patterned surfaces in batches. This system can be utilized to generate nano-patterned wafer with wide range of particle sizes for different type of applications. Our system also has precisely control over the amount of protein immobilized on gold nano-isalnds and thus enable the comparison of the cellular outcomes from different dosage. This system allows us to perform bulk biocue distribution study, both from the sandwich assay, where we directly sandwich cells with the nano-patterend VEGF surfaces, and direct cell seeding on nano-patterned surfaces. Also, this method can be combined with microprinting method to generate

modified nano-pattern within specific micro-scale microprinting area. This method is also applicable to different protein immobilization.

6.2 Materials and methods

6.2.1 Materials

The alkanethiols (1-mercapto-11-undecyl)septa(ethylene glycol) amine (EG-NH₂) and (1-mercapto-11-undecyl)tetra(ethylene glycol) (EG-OH) were purchased from Prochimia (Sopot, Poland). 5000 Da methoxy(ethylene glycol)silane (mPEG-silane) purchased from Laysan Bio (Arab, AL, USA). Heparin sodium salt from porcine intestinal mucosa purchased from Alfa Aesar (Ward Hill, MA, USA). p-azidobenzoyl hydrazide (ABH) from bioworld (Dublin, OH, USA). Human vascular endothelial growth factor A165 (VEGF) was obtained from Genentech. Human umbilical vein endothelial cells (HUVECs), endothelial cell basal and growth media (EBM-2 and EGM-2 respectively) were purchased from Lonza (Basel, Switzerland). Reagents used in the gold nanopatterned wafer fabrication were standard reagents issued in the Integrated Systems Nanofabrication Cleanroom facility at University of California, Los Angeles. Polydimethylsiloxane (PDMS) sheets were made using the Sylgard 184 silicone elastomer kit from Dow Corning (Midland, MI, USA) following the manufacturer's recommendation. The following biological buffers were made up in-house, namely, phosphate buffered saline (PBS; 137 mM NaCl, 2.7 mM KCl, 10 mM Na₂HPO₄, 1.8 mM KH₂PO₄, pH 7.4), PBST (PBS + 0.05% Tween-20), Tris buffered saline (TBS; 137 mM NaCl, 20 mM Tris, pH 7.6), TBST (TBS + 0.1% Tween-20), lysis buffer (150 mM NaCl, 50 mM Tris pH 7.4, 1% nonidet p-40, 0.25% sodium deoxycholate, 1 mM EDTA, 1 mM sodium vanadate, 10 mM β -glycerophosphate, 20 μ g/mL aprotinin, 20 μ g/mL leupeptin, 1 mM phenylmethylsulfonyl fluoride). All other reagents and products were purchased from Fisher Scientific and used as supplied unless otherwise noted.

6.2.2 Gold nanopatterned wafer fabrication

Nanopatterns comprising discs of diameter 0.5 μm at a pitch of 1.67 μm were generated via photolithography using a stepper. Processing conditions at each step were optimized and verified using identical wafers that had been coated with opaque chromium backing (30 nm) that facilitated imaging using the AMAT 7830i CD-SEM. Briefly, ultraflat fused silica wafers (university wafers) were primed with hexamethyldisilazane (HDMS), spin-coated with AZ® nLOF 5510 negative tone lift-off photoresist to a film thickness of 1 μm , then baked at 91 °C in contact-mode for 60 s. Following, the wafers were subjected to i-line ($\lambda = 365 \text{ nm}$) exposure in the ASML 5500 optical stepper using a reticle to create holes of diameter 0.5 μm at a pitch of 1.67 μm . The exposed wafers were baked at 110 °C in contact-mode for 60 s, and then puddle-developed with Microposit MF-319 developer for 60 s. Any residual photoresist in the holes was removed by oxygen plasma ashing for 1 minute at 50 °C. 5 nm titanium and 30 nm gold was deposited sequentially on the wafers using an e-beam evaporator at a rate of 1 Å/s each. Lift-off was conducted by immersion in AZ® 300T photoresist stripper at 80 °C for 5-10 min, following by immersion in acetone for 2 min in a sonicating bath. Wafers were washed in a cascade rinsers for 5 min, blow-dried, then sent for dicing using a Disco DAD321 Dicing Saw. The resulting diced silica pieces were washed sequentially in acetone, isopropanol and methanol, blow-dried, then stored under argon until use. Substrates with a continuous gold film were simply fabricated by e-beam evaporation of 5 nm titanium and 30 nm gold on cleaned standard laboratory glass slides. The gold substrates were stored under argon until use.

6.2.3 Heparin-ABH synthesis

Heparin was modified with the photoreactive group ABH as reported previously¹⁸⁷. Briefly, heparin was oxidized with sodium periodate to introduce aldehyde groups that could then be reacted with the hydrazide group on ABH. The mixture was then dialyzed against water

to remove the unreacted components and salts, lyophilized, then stored at -20 °C in the dark until use.

6.2.4 Discontinuous nano-patterned VEGF surface (cVc) processing

Nanopatterned substrates were immersed in a 2 mM alkanethiol mixture (comprising 1 % EG-NH₂ and 99 % EG-OH) in ethanol under argon for 18-24 h. Following incubation, the substrates were washed twice in ethanol, blow-dried, then immersed in 1 (w/v)% mPEG-silane and 1 (v/v)% triethylamine in toluene under argon for 5 h. Following incubation, the substrates were washed sequentially in toluene, ethanol, 70% ethanol, PBS, then immersed in 1 mg/mL heparin-ABH in PBS, pH 9-9.5 for 2 h. Following incubation, the substrates were washed three times with PBST, then blocked in 1% bovine serum albumin (BSA, fraction V, heat shock treated) in PBS for 1 h. Following incubation, the substrate were incubated in 1 % BSA in PBS with (or without, for the control condition) 100 ng/mL VEGF overnight at 4 °C. Following incubation, the substrate was exposed to UV ($\lambda = 365 \text{ nm}$, 3 mW/cm^2) for 10 min. The substrates were washed three times with PBST, then incubated with 1 mg/mL heparin in PBST at 4 °C until use (within 2 days).

6.2.5 Homogenous VEGF surface processing (Vc)

Homogenous gold substrates were immersed in a 2 mM alkanethiol mixture (comprising 1 % EG-NH₂ and 99 % EG-OH) in ethanol under argon for 18-24 h. Following incubation, the substrate were incubated in 1 % BSA in PBS with (or without, for the control condition) 100 ng/mL or 10 ng/ml VEGF overnight at 4 °C. Following incubation, the substrate was exposed to UV ($\lambda = 365 \text{ nm}$, 3 mW/cm^2) for 10 min. The substrates were washed three times with PBST, then incubated with 1 mg/mL heparin in PBST at 4 °C until use (within 2 days).

6.2.6 Bound VEGF quantification

For quantitation of surface-bound VEGF, PDMS molds with wells of known dimensions were fixed over the substrate. Direct enzyme-linked immunosorbent assay (ELISA) was carried out using human VEGF165 biotinylated goat pAb (R&D Systems, Minneapolis, MN, USA) and streptavidin horseradish peroxidase.

6.2.7 Bound VEGF visualization

For imaging of VEGF on the substrates, human VEGF mouse mAb (clone 26503) (R&D Systems) and goat anti-mouse IgG-AlexaFluor 555 (Molecular Probes, Life Technologies, Grand Island, NY, USA) were used to detect the surface-bound VEGF. Slides were imaged on the Axio Observer Z1 (Carl Zeiss, Jena, Germany) using the EC Plan-Neofluar 100x/1.3 Oil DIC objective.

6.2.8 Cell culture conditions

Primary normal HUVECs were purchased from Lonza (CC-2519). HUVECs were cultured in endothelial growth media (EGM-2) until 80% confluency before passaging into a fresh flask. In this way, HUVECs were continually expanded in cell culture flasks and used from passage 4 to 6. For the experiments, HUVECs were passaged onto fibronectin-coated PDMS sheets as reported previously¹⁸⁷. Briefly, PDMS sheets were incubated with 5% (3-aminopropyl)triethoxysilane (APTES) in ethanol overnight at room temperature. The now hydrophilic PDMS sheets were washed and sterilized in 70% ethanol before incubation with 100 µg/mL fibronectin in PBS at 37 °C, 5% CO₂ in a tissue culture incubator. HUVECs were plated on the PDMS cell sheets at a density of 15×10^3 cells per cm² and grown to about 80%

confluency over 2 days. Before the experiments, HUVECs were serum-starved in endothelial basal media (EBM-2; Lonza) for 6 hours.

6.2.9 Cell exposure to VEGF conditions

For cells exposure to VEGF in solution (Vs), EBM-2 was aspirated from the cell sheets and replaced with PBS with (or without, for the control condition) 2 ng/mL VEGF. This VEGF concentration was selected based on a mass transfer analysis to be equivalent to a surface VEGF concentration of 100 pg/cm¹⁸⁷.

For cells exposed to VEGF presented on a surface (Vc, cVc), before cell exposure, the substrates were washed three times with PBST, then three times with sterile PBS. Then, cell sheets were lifted from the petri dish with tweezers, quickly placed vertically and dabbed on a kimwipe at the edge to blot off excess media. The cell sheets were immediately placed cell-side in contact with the surface with (or without, for the control condition) VEGF. Incubation times (up to 2 h in the tissue culture incubator) were as indicated in the text.

6.2.10 Western blot analysis

Following VEGF exposure, cells were washed twice in ice-cold PBS containing 2 mM sodium vanadate, then lysed in lysis buffer (5 μ L per cm² surface area). The collected cell lysate was spun down at 13000 \times g for 10 min at 4 °C to pellet out any cell debris. The protein concentration of the cell lysate was evaluated using the DC protein assay kit from Bio-Rad (Hercules, CA, US) following the manufacturer's protocol. 5 μ g protein was loaded into each well of a 4-12 % gradient Tris-glycine SDS-PAGE gel (Novex or Bolt gel from Invitrogen, Life Technologies) run using the manufacturer's recommended protocol. The separated proteins were transferred to nitrocellulose membrane via wet tank transfer using ice-cold Tris-glycine buffer containing 20% methanol for 350 mA for 2 hr at 4 °C. Membranes were blocked with 5%

milk in TBST for 1 h at room temperature before blotting with the desired primary antibodies in 5% milk in TBST overnight at 4 °C. Primary antibodies (all purchased from Cell Signaling Technology (Danvers, MA, USA) unless otherwise stated) used were: phospho-VEGFR-2 (Y1175) rabbit mAb (#2478), VEGFR-2 (55B11) rabbit mAb (#2479), phospho-p44/42 MAPK (T202/Y204) antibody (#9101), p44/42 MAPK antibody (#9102), phospho-p38 MAPK (T180/Y182) antibody (#9211), p38 MAPK antibody (#9212), phospho-Akt (S473) (193H12) rabbit mAb (#4058), Akt antibody (#9272), phospho-VEGFR-2 (Y1214) rabbit pAb (#44-1052 from Invitrogen). The secondary antibody was goat anti-rabbit IgG (H+L) horseradish peroxidase conjugate from Invitrogen (#G-21234) diluted in 5% milk in TBST. The blots were developed with Amersham ECL Prime Western blotting detection reagent (GE Healthcare, Piscataway, NJ, USA) before imaging with the Gel Doc XR+ system with Image Lab Software (Bio-Rad). Band intensities were quantified using Image Lab.

6.2.11 Quantitative real-time PCR

Following VEGF exposure, cells were washed once with PBS, then incubated with 0.25% trypsin-EDTA (Gibco, Life Technologies) for 3 min at 37 °C. Trypsin was immediately quenched with 4% fetal bovine serum (Atlanta biologicals, Flowery Branch, GA, USA) in PBS. The collected cell suspension was spun down at 500 ×g for 5 min at 4 °C to pellet out the cells. Lysis buffer from the RNAqueous micro total RNA isolation kit (Ambion, Life Technologies) was immediately added to cell pellet. Total RNA was isolated from the cells following the manufacturer's protocol. RNA concentration was evaluated by UV absorbance ($\lambda = 260$ nm). Reverse transcription was carried out by loading 0.25 μ g RNA per reaction of the iScript Advanced cDNA synthesis kit (Bio-Rad). Quantitative real-time PCR (qPCR) was carried out using 10 ng cDNA per reaction of the Maxima SYBR Green/ROX qPCR master mix (Thermo Scientific, Pittsburgh, PA, USA) following the manufacturer's recommended protocol for three-

step cycling using the StepOnePlus real-time PCR system (Applied Biosystems, Life Technologies). Threshold cycles (C_T) were evaluated by the bundled software and expression fold change was calculated using the delta-delta C_T method assuming 100% efficiency. GAPDH was used as the housekeeping gene.

6.2.12 Short-term exposure immunofluorescent staining

Following VEGF exposure, cells were washed once with PBS, then incubated with 4% paraformaldehyde in PBS for 15 min at room temperature. The fixed cells were blocked with 10% normal goat serum (Invitrogen) containing 0.3% Triton-X for 1 h at room temperature before incubating with the desired primary antibodies in 1% BSA in PBS containing 0.3% Triton-X overnight at 4 °C. Primary antibodies used were: Jag1 (28H8) rabbit mAb (Cell Signaling Technologies), Dll4 (447506) rat mAb (R&D Systems), PECAM-1 (9G11) mouse mAb (R&D Systems). Following 3 washes with PBS, the cells were incubated with the corresponding secondary antibodies and Hoescht 33528 for 1 h at room temperature. Secondary antibodies (all from Molecular Probes, Life Technologies) used were: goat anti-rabbit IgG-AlexaFluor 488, goat anti-rat IgG-AlexaFluor 568, goat anti-mouse IgG-AlexaFluor 555. Following 3 washes with PBS, cells were coated lightly with glycerol and mounted on glass slides. Slides were imaged on the LSM 780 confocal laser scanning microscope (Carl Zeiss) using the EC Plan-Neofluar 40x/1.3 Oil DIC objective. For ease of imaging, a scratch was created using a yellow pipette tip on the cell sheets prior to VEGF exposure and cells on the edges of the scratch were imaged.

6.2.13 Overnight HUVEC spreading on cVc surface

Before cell exposure, the cVc surfaces were washed three times with PBST, then three times with sterile PBS. HUVEC cells were then seeded at a density of 33,333 cells per ml in

EGM-2 depleted of VEGF and Fibronectin. After 21 hours, cells were fixed with ice-cold methanol for 15 min. The cell samples were then washed 3 times with PBS. The fixed cells were blocked with 10% normal goat serum (Invitrogen) containing 1% BSA, 0.3M Glycine and 0.1% Tween-20 for 1 h at room temperature before incubating with Paxillin (5H11) mouse mAb (EMD Millipore) in the same blocking buffer overnight at 4°C. Following 3 washes with PBS, the cells were incubated with goat anti-rabbit IgG-AlexaFluor 555 (Life Technologies) and DAPI for 1 h at room temperature. Following 3 washes with PBS, cells were coated lightly with glycerol and mounted on glass slides. Slides were imaged on the LSM 780 confocal laser scanning microscope (Carl Zeiss).

6.2.14 Microprinting on nano-patterned surface

Nano-patterned glass surfaces were washed with acetone and ethanol, dried, then immersed in 1 (w/v)% mPEG-silane and 5 (v/v)% triethylamine in toluene under argon at 60°C for 3 days. Following mPEG-silane incubation, the substrates were washed sequentially in toluene and ethanol. Microprinting PDMS stamps were incubated in 0.17 (v/v)% EG-NH₂ in ethanol for 10 min, then the stamp was put into vacuum for 20 min. Stamps were then put in contact with the nano-patterned glass surfaces for 20 s. Then, the substrates were incubated at room temperature for 1 hour. After an hour, the glass surfaces were washed with ethanol. Then, the slides were immersed in 0.075 (v/v)% EG-OH in ethanol under argon at room temperature overnight. Next day, the substrates were washed sequentially in ethanol and PBS, and dried. The surfaces were then reacted with fibronectin in 10 mM MES (pH 6) at room temperature for 1 hour. The concentration of fibronectin used was 1 mg/mL; and, the molar ratio of NHS and EDC used was 20,000:115,000:1 (NHS:EDC:Fibronectin). Then, the slides were washed with PBS.

6.2.15 Cell seeding on microprinted fibronectin-immobilized nano-patterned surface

D1 cells in DMEM were seeded on the nano-patterned surfaces for 20 min at density of 100,000 cells/mL. Then, additional DMEM with 5 (v/v)% FBS and 1 (v/v)% penicillin-streptomycin was added to provide sufficient cell attachment to the surfaces. The slides with cells were then incubated for 16-18 hours. Next day, the slides with cells attached were incubated with 1% paraformaldehyde in PBS at room temperature for 15 min. Then, the slides were washed with PBS. The fixed cells were then blocked with 10% normal goat serum (Invitrogen) containing 1 (w/v)% BSA, 0.1% Tween-20, and 0.3 M glycine at room temperature for 1 hour before incubating with the desired primary antibodies (in the same blocking buffer) at 4°C overnight. The primary antibodies used were: Paxillin and rabbit anti-fibronectin. After the primary antibody incubation, the cells were washed sequentially with PBS containing 0.05% Tween-20 and PBS. The cells were then incubated with the corresponding secondary antibodies and DAPI at room temperature for 2 hours. The secondary antibodies used were: goat anti-mouse IgG-AlexaFluor 647, goat anti-rabbit IgG-AlexaFluor 488, and rhodamine-phalloidin. Then, the cells were again washed with PBS containing 0.05% Tween-20 and PBS sequentially. The nano-patterned surfaces with cells were then mounted on glass slides with antifade mountant. The slides were then imaged on Nikon C2.

6.2.16 Statistical analysis

All experiments were conducted in at least triplicates with the results reported as mean \pm standard error mean. One-way ANOVA with a Tukey post-test was used to establish statistical significance ($p < 0.05$) if shown.

6.3 Results and discussion

6.3.1 Gold nanopatterned wafer fabrication

The ASML stepper in conjunction with standard lithography techniques was chosen for the rapid fabrication of large areas (4- to 6-inch wafers) with sub-micron (hundreds of nm) features (Figure 6.1). Fused silica or glass was chosen as the substrate for ease of imaging in later experiments. In order to generate well-resolved features on the glass substrate, a negative photoresist was chosen in conjunction with lift-off to leave standing cylinders of titanium/gold on an ultra-flat glass surface.

The reticle used in the stepper to generate holes in the photoresist was initially designed to leave 0.3 μm holes at a pitch of 1.67 μm . Optimization of both the exposure energy and the focus offset using a die matrix typically generates a series of holes ranging from 0.4 to 0.8 μm (Figure 6.2A). As expected, higher exposure energies (towards the right of the matrix in Figure 6.2A) resulted in smaller features. However, over-exposure of the AZ® nLOF 5510 negative photoresist resulted in problems during lift-off and the absence of any nanopattern at worst. The final exposure parameters used for the substrates used in this paper were thus chosen to generate 0.7 μm holes at a pitch of 1.67 μm (Figure 6.2B, left). Following metal deposition and photoresist lift-off, the features generated were 0.7 μm islands at a pitch of 1.67 μm (Figure 6.2B, right). Representative images of ultra-flat glass wafer and nano-patterned glass wafer were shown in Figure 6.2C. After patterning, each glass wafer can be sliced into three 2.2cm by 6.7cm glass slide. This gives ultra-large nano-patterned area of 14.74 cm^2 per slide. Each batch production can produce 10 nano-patterned wafers which eventually yielded 30 ultra-large nano-patterned glass slides. It is observed that glass surface showed a golden yellow color after nano-patterning, yet still transparent (Figure 6.2C).

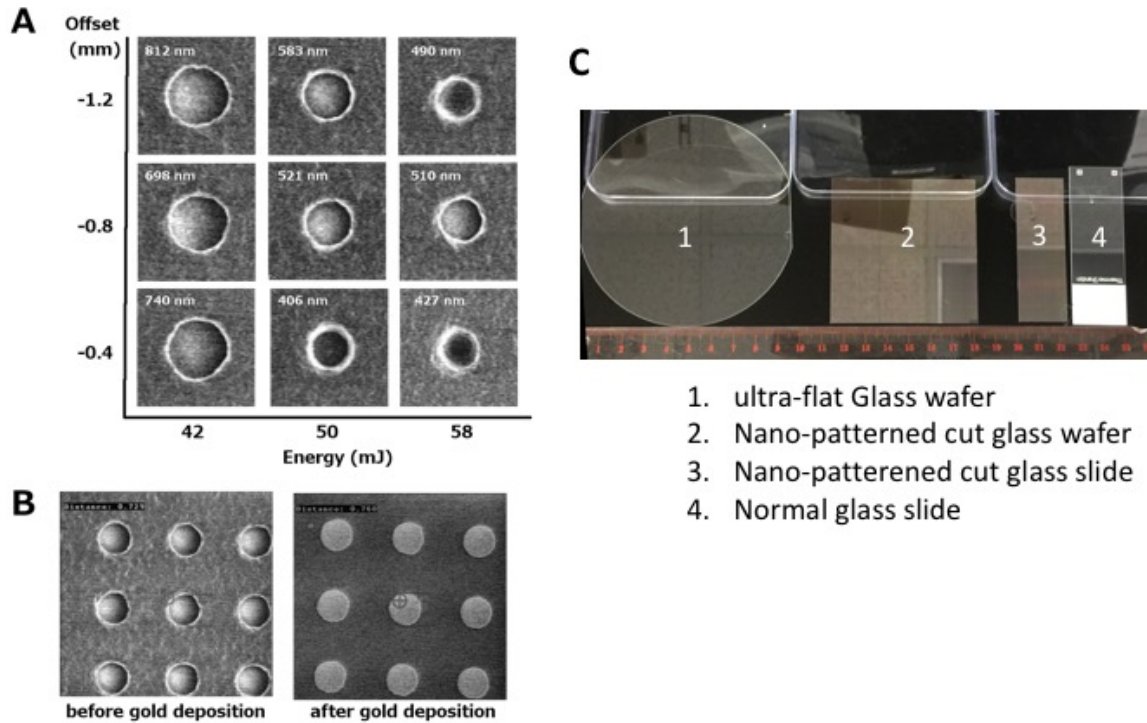


Figure 6.2 CD-SEM images of photoresist mask and gold nanopatterned glass wafers. (A) Representative matrix of focus offset (vertical axis) and UV exposure energy (horizontal axis) used to generate a range of hole sizes and morphologies on the photoresist layer using a photomask designed for 300 nm holes at a 1.67 μm pitch. Numbers on the panels reflect the approximate hole diameters measured using the imaging software. (B) Size and morphology of the features before and after gold deposition using an e-beam evaporator. The photoresist mask (left) was lifted off using AZ300T stripper, followed by sonication in acetone to reveal standing gold cylinders (right). (C) Representative photo of nano-patterned substrate.

6.3.2 VEGF conjugation to nano-patterned glass surface

In our study, we utilize VEGF as a template. Vascular endothelial growth factor A (VEGF) is a key protein involved at multiple stages of blood vessel formation during development and also in the adult as physiologic and pathologic angiogenesis¹⁸⁹. Current therapeutic strategies involving VEGF aim to disrupt the interaction of VEGF and its key receptor, VEGF receptor-2, (VEGFR-2) thereby blocking the angiogenic response in tumors. In contrast, pro-angiogenic strategies that attempt to promote angiogenesis using VEGF (with bulk dosage or gene transfection) in areas of tissue ischemia have been less successful, suggesting the existence of a gap in our knowledge of how VEGF functions to promote physiologically normal angiogenesis.

At the cellular level, VEGF-VEGFR signaling has been shown to trigger different intracellular signaling cascades associated with cell survival, proliferation and migration⁹⁷. During angiogenesis, the activation of these cascades must somehow be weighted in order to effectuate the distinct phases of angiogenesis. Thus, the facile application of soluble VEGF, often used to maintain and expand endothelial cells *in vitro*, is unlikely to translate into an effective therapeutic strategy for promoting the formation of a complex and mature vascular network. Indeed, many well-known *in vitro* models of sprouting angiogenesis require the assistance of fibroblasts for the formation of stable vessels, even in the constant presence of VEGF^{190, 191}. This suggests that the homogenous application of soluble VEGF is necessary but not sufficient for inducing stable vessel formation. In fact, other presentations of VEGF have shown to efficiently induce healthy vessel formation, such as covalently-linked VEGF and clustered VEGF. However, the distribution of VEGF has not been fully investigated. Here, we hypothesize that besides the presentation of VEGF (soluble, electrostatically or covalently-bound VEGF), the nano-scale distribution of VEGF also regulates VEGFR-2 pathway and affect cellular outcomes.

This work builds on that foundation by demonstrating that the endothelial cell response can be further tuned by a discontinuous distribution of covalently-bound VEGF. Here, we describe a method for rapidly fabricating large areas of nanoscaled gold islands that can be chemically conjugated to VEGF via heparin. Endothelial response to nano-scaled subcellular discrete distribution of VEGF was found to differ from that of a continuous surface of VEGF. This posits the patterning of VEGF as an alternative means of directing endothelial cell response in a spatiotemporal manner. VEGF was immobilized on the homogeneous gold surfaces (Vc) and gold nanopatterned (cVc) surfaces following the bind-and-lock strategy previously published by our lab (Figure 6.3)¹⁹². The primary advantage of this technique is the presentation of VEGF in a physiologically relevant context (bound to heparin) that enhances

signal transduction¹⁹³. Heparin binding also improves the stability of VEGF and increases its half-life from 100 min to 2 days at 37 °C¹⁸⁷. Briefly, a 1% amine-functionalized self-assembled monolayer (SAM) of alkanethiol was formed on the gold. The exposed glass was then passivated with a layer of mPEG-silane to minimize surface fouling during subsequent conjugation steps¹⁹⁴. Later, oxidized heparin functionalized with the UV-crosslinkable ABH group was conjugated to the amine-functionalized SAM via reductive amination. Thus, VEGF was allowed to “bind” to the immobilized heparin via affinity interaction. In the end, the bound VEGF was “locked” to the heparin backbone via UV crosslinking.

VEGF was conjugated to nanopatterned gold slides via modified heparin: the process

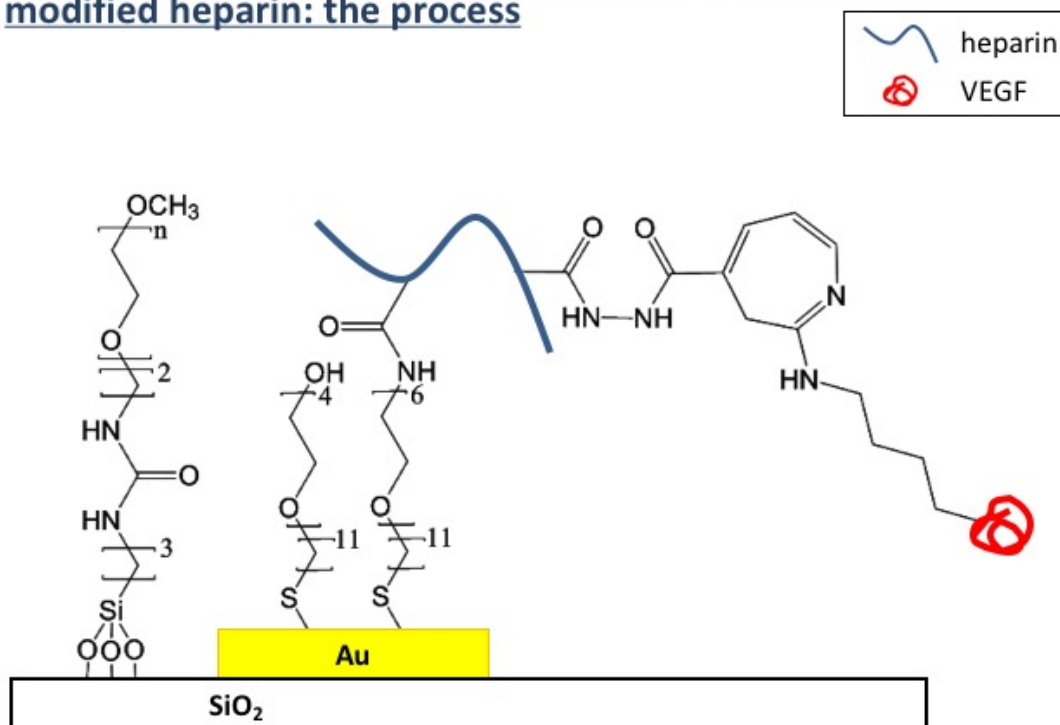


Figure 6.3 Schematic of the VEGF conjugation procedure.

Due to the large spacing between the gold islands, the gold surface coverage on the nanopatterned glass surfaces amounted to less than 10% of the total surface area. Without passivation of the glass background via mPEG-silane, the amount of non-specifically bound VEGF overwhelmed the amount of specifically bound VEGF (Figure 6.4A). When comparing

immobilized VEGF amount on homogeneous gold surface (Vc) with and without silanization, this additional processing step did not significantly impact the VEGF conjugation process. After silanization, the bulk VEGF surface concentration of cVc condition ($204 \pm 94 \text{ pg/cm}^2$) was approximately 5 times lower than Vc ($546 \pm 22 \text{ pg/cm}^2$) under the same processing conditions (same amount of VEGF dosage). In later experiments, gold surfaces were generated with this surface concentration of VEGF (denoted Vc high) and also a lower surface concentration of VEGF (denoted Vc low) to match the bulk VEGF concentration on cVc.

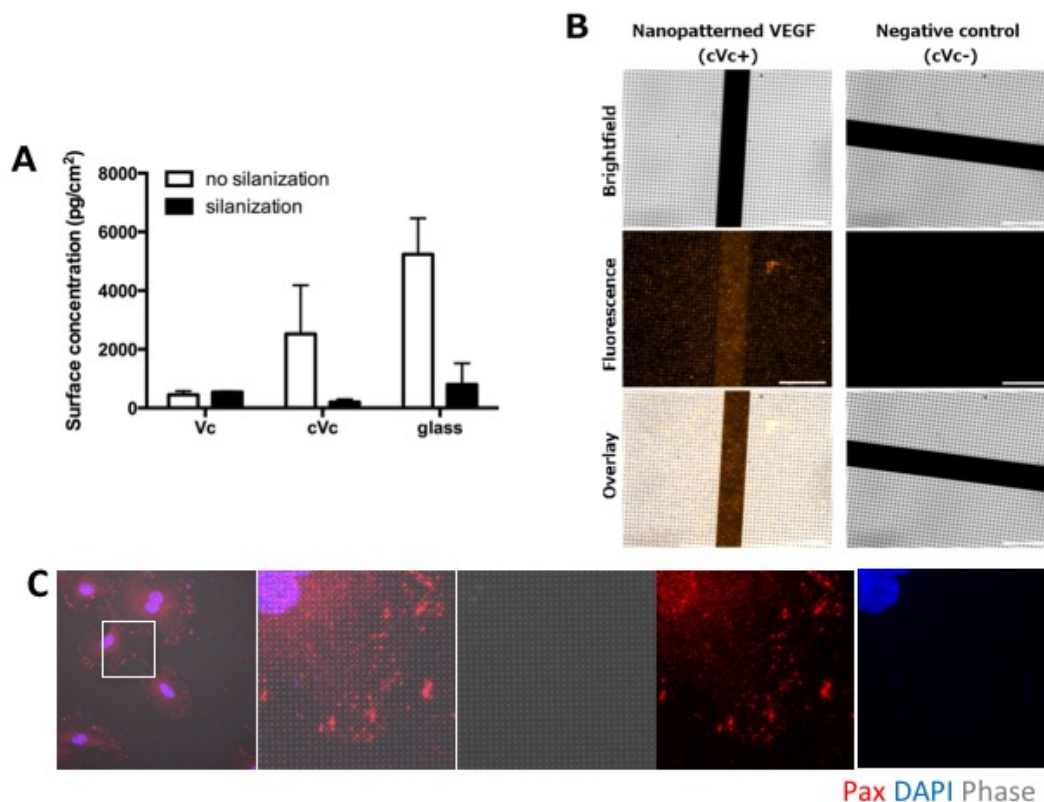


Figure 6.4 Specific binding of VEGF to gold nanopatterned features on glass. (A) Bulk surface concentration of VEGF on homogeneous gold-coated glass (Vc), heterogeneous gold nanopatterned glass (cVc) and bare glass (Vg) following identical VEGF conjugation protocols. Silanization of exposed glass surfaces using mPEG-silane was necessary to reduce non-specific adsorption of VEGF to the non-patterned surface (compare clear and filled columns). (B) Conjugated VEGF on gold nanopatterned glass visualized by standard immunofluorescent techniques employing a primary anti-VEGF antibody and fluorescently-tagged secondary antibody. The gold islands were visualized under brightfield and overlaid with the fluorescent images, demonstrating specific binding of VEGF to the gold nanofeatures (cVc+). The no VEGF control (cVc-) processed in the absence of VEGF demonstrated no fluorescence under identical imaging conditions. (C) Representative immunofluorescent images of HUVECs seeding on cVc surface.

VEGF binding to the gold nanopatterns was then verified by sequential incubation of the surface with a VEGF antibody and an AlexaFluor 555-labeled secondary antibody. Gold nanopatterned surfaces conjugated to VEGF displayed a fluorescent nanopattern corresponding with the gold nanopattern imaged via brightfield microscopy (Figure 6.4B). Control surfaces processed identically but without VEGF incubation did not display the fluorescent nanopattern under identical imaging parameters. The seeding of HUVEC cells on the cVc surface also showed clear paxillin signal co-localized with gold nano-patterns, indicating that nano-patterned surface of VEGF with heparin can also be used as a biocue to promote cell attachment (Figure 4C).

6.3.3 Protein level analysis on VEGFR-2 phosphorylation time course

To study the effect of nano-scaled distribution of immobilized VEGF on endothelial cell VEGFR-2 activation, a sandwich assay was utilized as previously published¹⁸⁷. Briefly, cells cultivated on fibronectin-coated PDMS sheet was first sandwiched together with cVc and Vc surfaces for 5, 10, 15, 30, 60 and 120 min respectively, then collected for Western Blot analysis. Soluble VEGF (Vs, 2ng/ml) was also performed as a control group. Benefited from ultra-surface area of this nano-patterned surface, enough lysate was collected easily for the standard Western Blot analysis.

The binding of VEGF to VEGFR-2 induces receptor dimerization and autophosphorylation of specific intracellular tyrosine residues. In particular, Y1175 and Y1214 are major phosphorylation sites associated with the activation of the MAPK pathways in endothelial cells, activating intracellular signaling cascades critical for proliferation, migration and survival^{97, 98}.

In the soluble VEGF control group, the administration of soluble VEGF (Vs+) results in a large spike in relative VEGFR-2 phosphorylation at Y1175 (pY1175/VEGFR-2) within minutes as expected (Figure 6.5A). Background levels of pY1175/VEGFR-2 in the absence of VEGF (Vs-) were close to zero at all timepoints. Similarly, Y1214 phosphorylation (pY1214/VEGFR-2) also increases, but tails off more gradually with time (Figure 6.5B). The background levels of pY1214/VEGFR-2 in the absence of VEGF (Vs-) is likely due to the culture conditions of the HUVECs on fibronectin-coated PDMS. Such background levels were not observed in HUVECs cultured on tissue-culture plastic (unpublished data), suggesting that the presence of integrin ligand such as fibronectin or changes in mechanical stiffness of the culture substrate have effects on VEGFR-2 phosphorylation at Y1214.

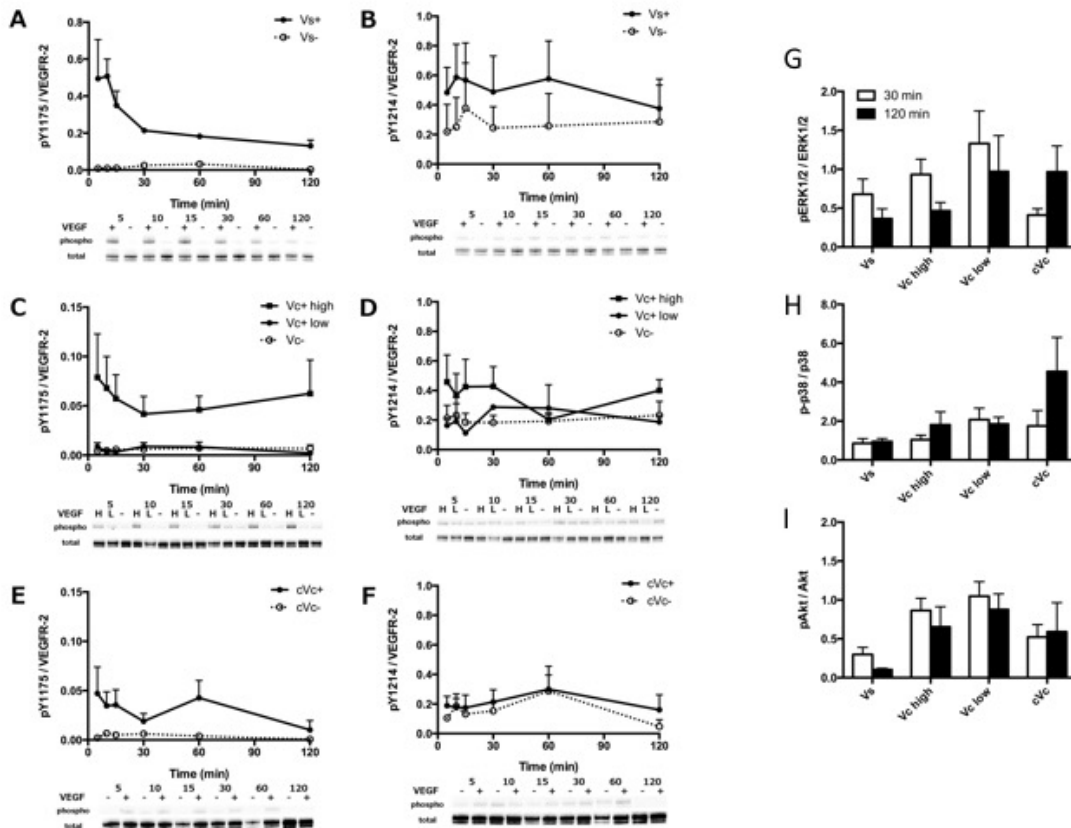


Figure 6.5 Time course for the phosphorylation status of VEGFR-2 at the tyrosine 1175 and 1214 residue (pY1175, pY1214 respectively) of cells in contact with different forms of VEGF quantified using Western

blot densitometry. (A, B) Phosphorylation time course of VEGFR-2 from cells in contact with soluble VEGF (Vs+; solid circles) or the no VEGF buffer control (Vs-; empty circles). (C, D) Phosphorylation time course of VEGFR-2 from cells in contact with VEGF covalently conjugated on a continuous gold film at high concentration (Vc+ high; solid squares) or low concentration (Vc+ low; solid circles), and gold film with no VEGF (Vc-; empty circles). (E, F) Phosphorylation time course of VEGFR-2 from cells in contact with VEGF covalently conjugated on a gold nanopattern (cVc+; solid circles), and gold nanopattern with no VEGF (cVc-; empty circles). (G) Relative phosphorylation of ERK1/2. (H) Relative phosphorylation of p38. (I) Relative phosphorylation of Akt.

In the presence of covalently-bound VEGF, only the condition with high amount of VEGF immobilized (Vc+ high) showed sustained Y1175 phosphorylation levels while low amount of VEGF immobilized gold surface (Vc+ low) and directly exposure to continuous gold surface without VEGF (Vc-) conditions showed Y1175 phosphorylation level close to zero at all time points (Figure 6.5C). Thus, with homogeneous immobilization of VEGF, high amount of VEGF ($546 \pm 22 \text{ pg/cm}^2$) was needed in order to activate Y1175 phosphorylation. Y1214 phosphorylation of Vc+ high condition remained comparable to that in the presence of soluble VEGF at early time points (Figure 6.5D). Little Y1214 phosphorylation was observed in Vc+ low condition, consistent with the trend observed for Y1175 phosphorylation. Consistent with the Vs-control, the background levels of pY1214/VEGFR-2 on Vc- remained slightly elevated due to the effects of Fibronectin-coated PDMS sheets.

In contrast, nanopatterned covalently-bound VEGF (cVc+), which has same amount of VEGF as Vc+ low condition, resulted in similar levels of Y1175 phosphorylation as Vc+ high condition (Figure 6.5E). Background levels of pY1175/VEGFR-2 on the respective control, cVc- (exposure to a nanopatterned gold without VEGF), were close to zero. This indicates that the discontinuous distribution of covalently-bound VEGF (cVc+) is more efficient than homogeneous immobilization of VEGF (Vc+). No difference of pY1214/VEGFR-2 was seen between cVc+ and cVc- condition, indicating the pY1214 requires higher dosage of cVc to be activated (Figure 6.5F).

Overall, the most interesting finding in Y1175 and Y1214 phosphorylation study is that lowering the surface VEGF concentration to match the bulk cVc VEGF concentration (Vc+ low)

did not result in significant phosphorylation of Y1175 as observed in cVc condition (Figure 6.5C), suggesting that the nanopatterned discontinuous distribution of equivalent masses of VEGF is more efficient at Y1175 phosphorylation in VEGFR-2 activation pathway.

For simplicity, future experiments will focus on a comparative study of the different VEGF presentations, henceforth referred to as Vs for soluble VEGF, Vc for covalently-bound VEGF, and cVc for clustered (nanopatterned) covalently-bound VEGF.

The phosphorylation of VEGFR-2 at specific residues leads to the activation of downstream signaling cascades resulting in different cellular outcomes^{97, 98}. For example, activation of the ERK1/2 MAPK pathway following Y1175 phosphorylation is typically associated with the proliferative response in HUVECs. While activation of the p38 MAPK pathway following Y1214 phosphorylation is associated with the migratory response in HUVECs. Activation of the anti-apoptotic Akt pathway is also associated with multiple aspects of vascular homeostasis and angiogenesis¹⁹⁵.

In response to the addition of soluble VEGF, the phosphorylation of these protein kinases typically peaks within 30 min¹⁹⁶⁻¹⁹⁸. Thus, the relative phosphorylation of these kinases would have decreased by the 120-min timepoint, either due to consumption of VEGF, or internalization and degradation of VEGFR-2. Interestingly, nanopatterned VEGF (cVc) showed the opposite trend with initially low levels of ERK1/2 and p38 phosphorylation (at 30 min) that increased over time (at 120 min; Figure 6.5G,H). Overall, it also appeared that covalently-bound VEGF, in all forms (Vc and cVc) was more effective at triggering the p38 and Akt pathways (Figure 6.5H,I). The extended p38 phosphorylation kinetics is congruent with the results reported by Chen and colleagues using collagen-bound VEGF although they did not report data past the 30-minute timepoint⁹⁹. Chen and colleagues also reported reduced levels of Akt phosphorylation in their experiment setup when comparing collagen-bound VEGF with soluble

VEGF. However, with our set up, we observe a slight, though not statistically significant, increase in Akt phosphorylation, suggesting that the presentation of heparin-bound VEGF in our experimental setup may be more favorable for promoting vasculogenesis and/or angiogenesis.

Overall, it is proven that this ultra-large nano-patterned surface can be utilized to effectively test the protein level of biocue activations.

6.3.4 Changes in gene expression in response to nanopatterned VEGF

The initial stages of angiogenic sprouting involve the activation of the quiescent endothelium, selection of the leading tip cell and consequent lateral inhibition of the neighboring cells, which become stalk cells^{54, 199}. The differentiation of the endothelial cells into tip and stalk cells is marked by an increase in Notch signaling via the expression of Notch ligands, Dll4 and Jag1²⁰⁰. Also, during angiogenesis process, Notch signaling has been shown to result in the differential regulation of VEGFR-1, 2, 3^{201, 202}. Thus, we proceed with the qPCR analysis for these specific genes.

At the 30 min timepoint, there was no significant fold change in VEGFR mRNA levels (Figure 6.6A, B, C). By the 120 min timepoint, Vs resulted in a statistically significant upregulation of VEGFR-1 and VEGFR-2, but not VEGFR-3 gene expression. Notably, there were no statistically significant changes to the mRNA levels of all three VEGFRs in the presence of cVc. Interestingly, cVc surface showed an increased trend in VEGFR-2 expression compared with Vc low, further confirming the effects of the discontinuous distribution.

The Notch receptor-ligand pathway forms a close counterpart to the VEGF receptor-ligand pathway in directing endothelial cell response during sprouting angiogenesis²⁰⁰. In particular, the Notch ligands Dll4 and Jagged1 are known to form an antagonistic pair in regulating tip and stalk cell phenotype, with Dll4 predominantly expressed in tip cells, and

Jagged1 and Dll1 in the adjacent stalk cells^{140, 203, 204}. Statistically, there were no significant changes to the mRNA levels of all three Notch ligands under the different incubation conditions (Figure 6.6 D, E, F), although Dll4 appeared to be slightly upregulated in the presence of Vs. This could suggest that 120 min is not sufficiently long for the establishment of Notch signaling and differential expression of the different Notch ligands. On the other hand, roughly even populations of stalk and tip cells may have been induced by the treatment, averaging out to a basal level of Notch ligands following bulk harvest of the endothelial cells.

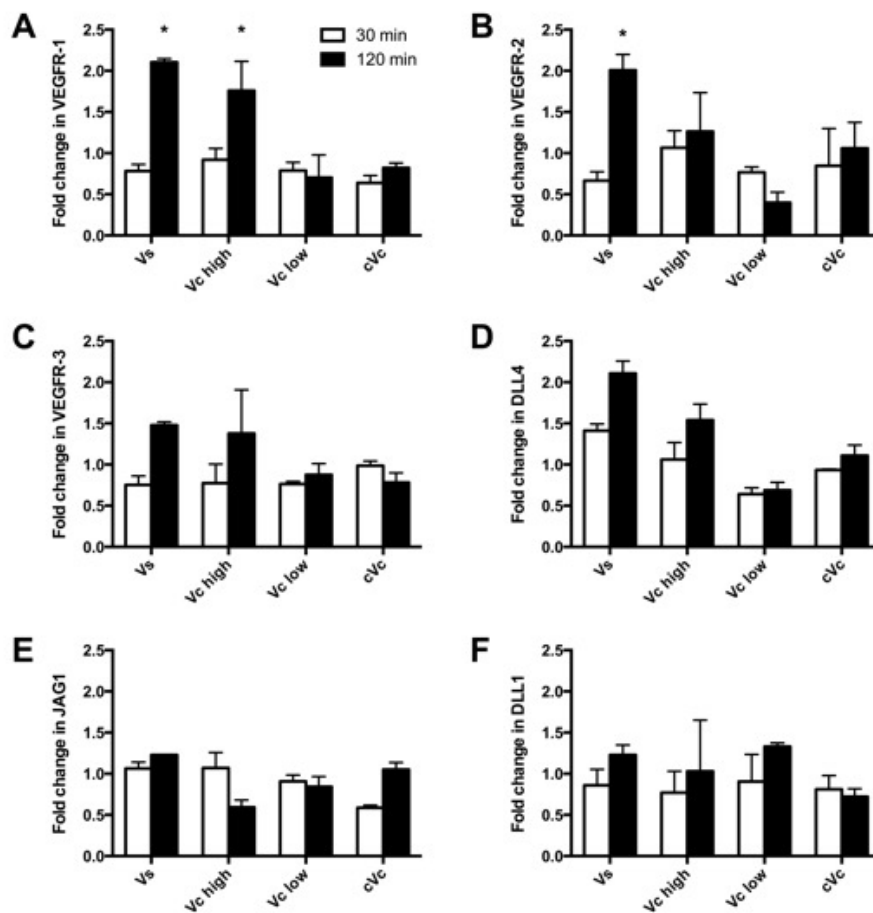


Figure 6.6 Fold change in mRNA levels (relative to the corresponding negative controls) of the VEGFRs and Notch ligands from cells in contact with different forms of VEGF quantified using quantitative real time PCR. (A) Fold change in VEGFR-1 mRNA levels. (B) Fold change in VEGFR-2 mRNA levels. (C) Fold change in VEGFR-3 mRNA levels. (D) Fold change in Dll4 mRNA levels. (E) Fold change in Jag1 mRNA levels. (F) Fold change in Dll1 mRNA levels.

6.3.5 2D cellular response to nanopatterned VEGF

Due to the differential expression of Notch ligands in tip and stalk cells, we theorized that the lack of significant changes to the Notch ligand mRNA levels may be due to an averaging effect when cells were pooled for RNA extraction. We therefore proceeded to look at the intracellular distribution of these ligands at the point of cell harvest – 30 min and 120 min (Figure 6.7). Surprisingly, we found changes in the intracellular distribution in the Notch ligands as early as 30 minutes into the incubation with VEGF. This timepoint is typically too short for there to be changes in protein expression due to changes in gene expression in response to external stimuli. Notably, with soluble VEGF treatment, Dll4 was expressed as punctate structures in the cytoplasm at both timepoints (Figure 6.7B, E). These structures were less prominent in cells exposed to VEGF in other configurations.

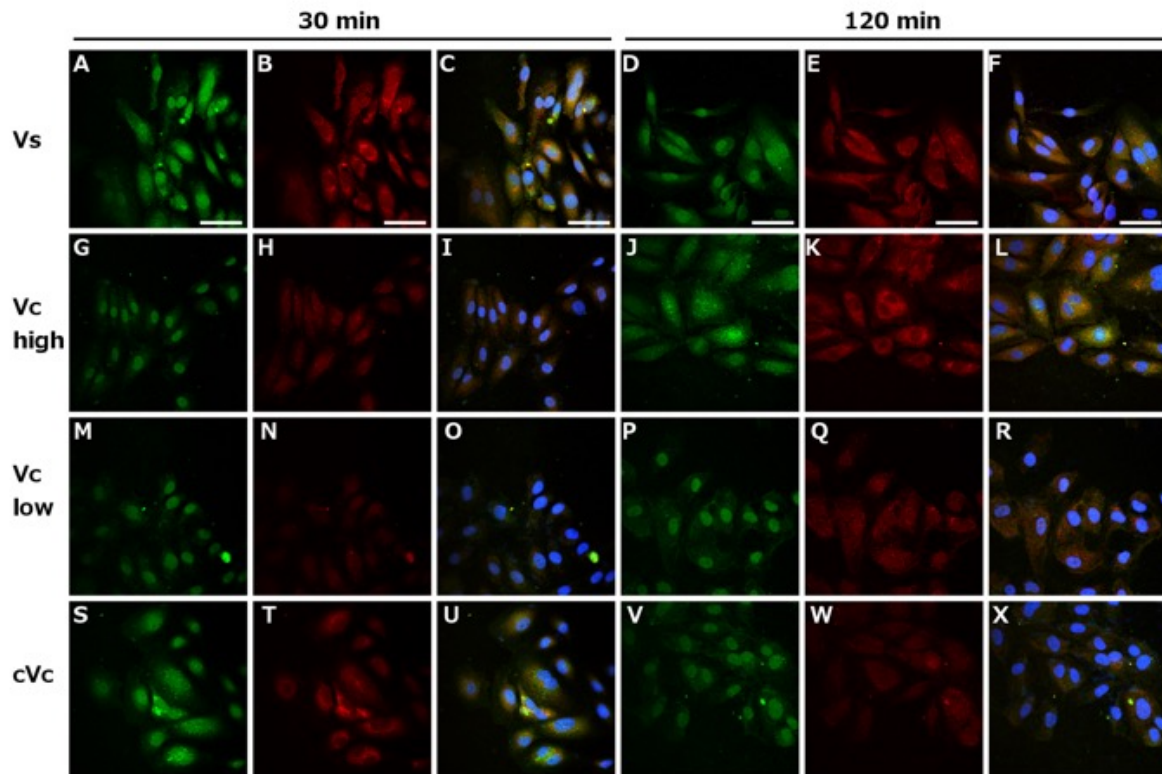


Figure 6.7 Intracellular distribution of Jagged1 (green) and Dll4 (red) in cells in contact with different forms of VEGF imaged using confocal microscopy. Hoescht 33528 (blue) was used to stain the nuclei. (A-C) Intracellular distribution of Jagged1, Dll4, and the overlay (with Hoescht) in cells exposed to Vs for 30

min. (D-F) Intracellular distribution of Jagged1, Dll4, and the overlay (with Hoescht) in cells exposed to Vs for 120 min. (G-I) Intracellular distribution of Jagged1, Dll4, and the overlay (with Hoescht) in cells exposed to Vc high for 30 min. (J-L) Intracellular distribution of Jagged1, Dll4, and the overlay (with Hoescht) in cells exposed to Vc high for 120 min. (M-O) Intracellular distribution of Jagged1, Dll4, and the overlay (with Hoescht) in cells exposed to Vc low for 30 min. (P-R) Intracellular distribution of Jagged1, Dll4, and the overlay (with Hoescht) in cells exposed to Vc low for 120 min. (S-U) Intracellular distribution of Jagged1, Dll4, and the overlay (with Hoescht) in cells exposed to cVc for 30 min. (V-X) Intracellular distribution of Jagged1, Dll4, and the overlay (with Hoescht) in cells exposed to cVc for 120 min.

Also at the 30 min timepoint, there appeared to be pronounced cytoplasmic localization of Jagged1 in cells exposed to cVc (Figure 8S), compared to the other conditions. However, this disappeared by the 120 min timepoint, indicative of the presence of some kind of feedback mechanism controlling the intracellular distribution of Jagged1. Such cytoplasmic localization of Jagged1 was also observed in cells incubated on Vc high for 120 min, but not for Vc low (Figure 6.7J, P). This suggests that different VEGF amount and distribution may exhibit qualitatively different effects at very different timepoints, and that we may be missing out on important differences by limiting ourselves to short, predetermined timepoints.

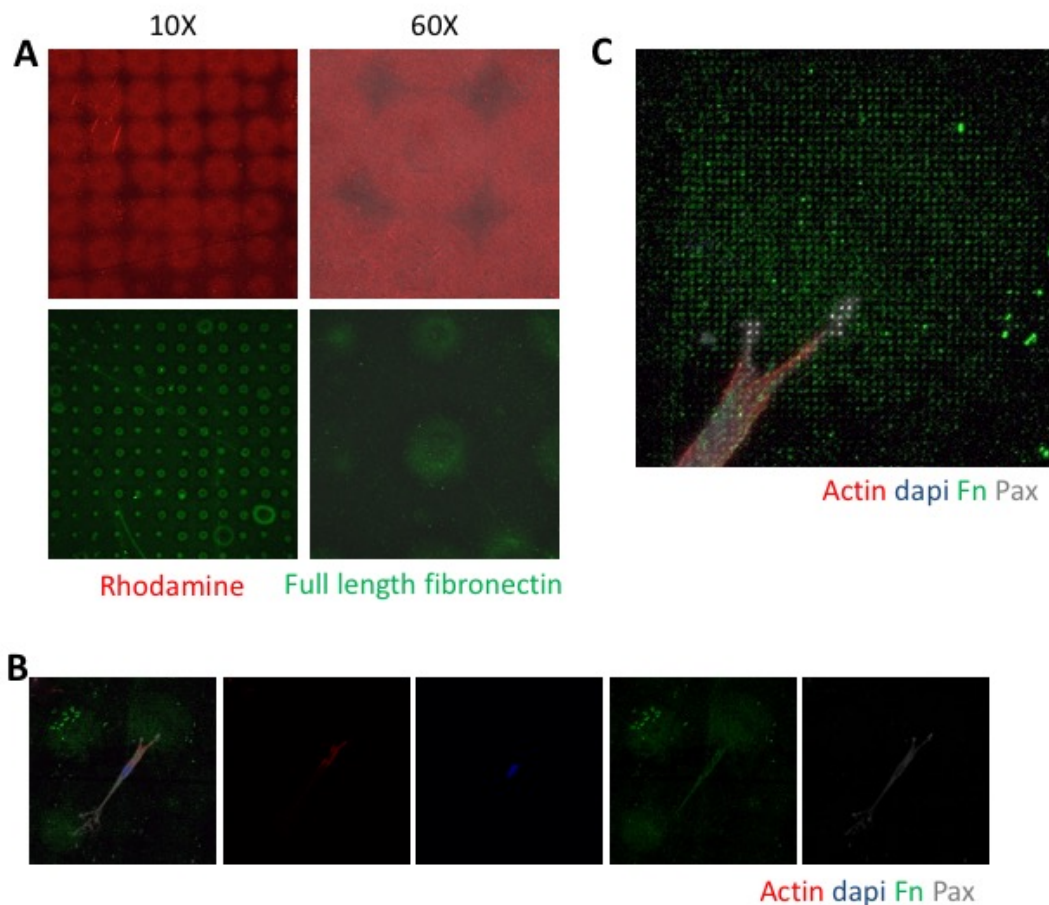


Figure 6.8 (A) Representative of microprinting outcomes on nanopatterned surface. (B) 10X images of D1 cells attachment on nanopatterned fibronectin surface with microprinting patterns. (C) Enlarged image of D1 cells seeding on nanopatterned fibronectin surface within circular microprinting patterns.

6.3.6 Microprinting on nanopatterned fibronectin surfaces

Microprinting can also be performed on this ultra-large nano-patterned surface. It can help to create micro-pattern on top of nano-patterning, which enables distribution study of biocues within an area with controlled size and shape. For example, MSCs can differentiate based on the shape of the micro-pattern²⁰⁵, but little is known about how distribution signal within the patterns affect cellular outcomes.

In our study, microprinting patterns were printed on top of nano-patterned surface using amine-end alkanethiol, followed by biocue immobilization, such as fibronectin. This results fibronectin signals only on gold nano-pattern within specific micro-scale region (Figure 6.8A). D1

cells were then seeded on the fibronectin-immobilized surface for 20 min to allow quick attachment. It was observed the cells attached to the microprinting region of fibronectin (Figure 6.8B). Clear focal adhesion can also be observed specifically on nano-patterns where fibronectin was immobilized (Figure 6.8C).

6.4 Conclusions

The discontinuous nano-pattern artificial surface created in this study coupled nano-scale gold pattern with micron-scale spacing, mimicking the naturally heterogeneous distribution of growth factors in the naturally occurring pericellular matrix. In this study, we have shown that the presentation of VEGF in different forms (Vs, Vc, and cVc), triggers distinct endothelial cell responses. Benefiting from the ultra-large nano-pattern surface and the ease of heparin “locking” technique, similar type of study can be easily performed on the other growth factors using the same system. This nano-patterned surface can also be combined with microprinting technology to look at cellular response within a confined shape.

Chapter 7

Conclusions and future directions

7.1 Introduction

The objective of this research was to study and engineer the signals that promote angiogenesis in wound healing process. These signals include but not limited to growth factors and integrin ligands. ECM molecules such as Fibronectin, growth factors such as VEGF (Vascular Endothelial Growth Factors) and their receptors have been shown to be key regulators of angiogenesis and neovascularization, with embryos lacking these genes, resulting in lethality due to defects in angiogenesis^{1,2}. The following sections reall the proposed specific aim and hypotheses, describing both the major conclusions and the future directions.

7.2 Specific Aim 1 (Chapter 3)

This aim developed a portable imager which detects nanocapsule degradation real-time. The VEGF nanocapules with different protease-degradability were utilized as template in this study. Samples treated with protease at different time points were tested. Samples were also real-time imaged to monitor real-time degradation.

Hypothesis 1: Nano-lens based computational microscopy can be utilized as an effective tool to monitor nanocapsule degradation, such as protein-core VEGF nanocapsules.

By using our computation holographic microscopy based method, a lot of obstacles are overcome. In general, design and synthesis of biodegradable nanoparticles, without the cargo, require a direct method for observing and quantification of the changes in their matrix. Several

techniques such as Raman spectroscopy¹⁹, fluorescence resonance energy transfer²⁰, optical absorption^{21,22,23} and Magnetic Resonance Imaging (MRI)²⁴ have been previously utilized to monitor the degradation process of the nanoparticle matrix. However, these methods can only be used for specific types of nanoparticles and are not universally applicable for any type of particle. Some of the more general strategies that have been used for monitoring nanoparticle degradation involve measurement of weight or size by using chromatography²⁵, dynamic light scattering (DLS)¹⁴ and electron microscopy (EM)²⁶. These methods can provide an estimation of the nanoparticle degradation process but each has its own set of drawbacks. For example, EM is performed on dry samples and thus it is not possible to perform degradability measurements with most polymeric nanoparticles, such as hydrogels, liposomes etc. DLS, on the other hand, can perform measurements in solution but is not very accurate and also is quite limited in terms of the dynamic range of particle size and density that can be measured, often requiring large amounts of sample volume for each measurement.

Here, two different testing methods were used to monitor and quantify the degradation of VEGF nanoparticles. The first method involves sizing the nanoparticles by discretely sampling the synthesis solution at different time points after addition of proteases. A second method using a sandwich assay was developed to monitor the live degradation process in a continuous manner by placing a trypsin coated coverslip on the nanoparticle/nanolens complex, also imaged by our computational holographic microscope. These computational imaging experiments were performed on both degradable and non-degradable nanoparticles, showing a drastic change to the polymer matrix bound together by degradable crosslinkers compared to the nondegradable ones. Overall, this computational holographic imaging based nanoparticle monitoring platform provides a much needed, cost effective and high-throughput method to quantify the degradation process of any type of nanoparticle using very small amounts of sample volume.

There are also some draw-backs of this technology. For examples, some size-range of nanoparticles may fall off the testing cover slip, rendering a biased data set. Future systematically optimization of both software and sample loading coverslips will need to be done to enable this technology to be commercially used.

7.3 Specific Aim 2 (Chapter 4)

This aim investigated the effects of specific integrin activation on angiogenesis. A 3D fibin gel sprouting assay was carried out to study HUVEC sprouting and branching *in vitro*. Then a modified matrigel assay was performed on mouse model to look at neo-vessel infiltration and neo-vessel morphology. Later, an ischemic stroke mouse model was also utilized to study the neo-vessel generation and infiltration in the stroked area *in vivo*.

Hypothesis 2: Integrin-specificity matrix can be utilized to as a morphogenic cue in guiding endothelial cell responses both *in vitro* and *in vivo*. Specific integrin activation could induce the generation of healthy and non-leaky vessels.

In Chapter 4, it is shown that through engineering hydrogel materials to promote $\alpha3/\alpha5\beta1$ integrin binding with VEGF presence, a space filling and mature vasculature can be formed compared to hydrogel materials that promote a $\alpha v\beta3$ integrin binding (e.g. RGD). *In vitro*, $\alpha3/\alpha5\beta1$ scaffolds promoted endothelial cells to sprout and branch, forming organized extensive networks that eventually reached and anastomosed with neighboring branches. *In vivo*, $\alpha3/\alpha5\beta1$ scaffolds delivering vascular VEGF promoted non-tortuous blood vessel infiltration and non-leaky blood vessels by 10 days post stroke. In contrast, materials that promote $\alpha v\beta3$ integrin binding promoted endothelial sprout clumping *in vitro* and leaky vessels *in vivo*. This work shows for the first time that precisely controlled integrin activation from a biomaterial can be

harnessed to direct therapeutic vessel regeneration and reduce VEGF induced vascular permeability *in vivo*.

Here, the effects on integrin specificity is only studied for angiogenesis. Future studies should involve other therapeutic related research directions, such as lymphogenesis. Also, the integrin-specificity can be tuned in all kinds of biomaterials, such as FDA-approved PEG to look at therapeutic outcomes on different wounds. Besides the integrin specificity, the combination of different integrin specificity can also be studied. It has been shown that different integrins are activated during different stages of angiogenesis. By using combinations of integrin-specific materials, optimum wound healing outcome may be achieved.

7.4 Specific Aim 3 (Chapter 5)

This aim utilized the cluster format of VEGF to treat diabetic mouse cutaneous wounds. The wound closure percentage, epithelial layer thickness, endothelial cell and pericyte infiltration percentage were all studied.

Hypothesis 3: Clustered VEGF can promote diabetic cutaneous wound healing.

In Chapter 5, it was found that highly clustered VEGF (hcV) promoted a greater wound healing in diabetic mice at day 7 compared with soluble VEGF and low clustered VEGF. These results could be explained by the effect of hcV on the VEGF receptor 2 (VEGFR2) activation on endothelial cell surface. It is already known that different presentation of VEGF can lead to different VEGFR2 pathway activation. For example, it was shown that the anchorage of VEGF to the extracellular matrix can convey differential signaling response to endothelial cells⁹⁹. It was also shown that when VEGF is covalently-immobilized to surface, VEGF internalization is not required for VEGF Receptor-2 phosphorylation¹⁸⁷. Specifically, in diabetic mice, cell surface abundance of VEGFR2 is reduced and VEGFR2 signaling pathway is ligand-independent¹⁸⁸.

Our observations suggest that highly clustered VEGF promotes the activation of VEGFR2 differently, increasing the pro-repair angiogenesis in diabetic wound with trivial dosage. This finding could help with future presentation design of growth factors to achieve efficient wound healing.

For this specific study, only two different types of VEGF clusters were utilized. It is still not clear on that mechanism regarding how different VEGF clusters function. It was shown by previous lab member that the size of VEGF clusters doesn't vary yet the loading amount of VEGF can be controlled to have order of magnitude difference. It is possible that the effects of hcV merely comes from the exposed amount of VEGF within certain area. It is also possible that the orientation and attachment angle of VEGF also plays a role.

7.5 Specific Aim 4 (Chapter 6)

This aim designed a large nano-patterned surface to study the distribution effects of VEGF. VEGF was immobilized to nano-islands on ultra-flat glass surface which is about 600-700nm in diameter. Homogenous immobilized VEGF was used as control. VEGFR-2 activation study was performed using Western Blots and qPCR. HUVECs were later directly seeded on the nano-patterned surface to look at cell attachment and spreading.

Hypothesis 4: The discontinuous distribution of VEGF immobilization on nano-patterned surfaces will result in a distinct VR-2 phosphorylation pattern, downstream signal, EC morphology and phenotype compared with homogenous immobilized VEGF. Both western blot analysis and PCR technique can be used to analyze the outcomes on the protein and mRNA expression levels.

The discontinuous nano-pattern artificial surface created in Chapter 6 coupled nano-scale gold pattern with micron-scale spacing, mimicking the naturally heterogeneous distribution

of growth factors in the naturally occurring pericellular matrix. In this study, we have shown that the presentation of VEGF in different forms (Vs, Vc, and cVc), triggers distinct endothelial cell responses. Benefiting from the ultra-large nano-pattern surface and the ease of heparin “locking” technique, similar type of study can be easily performed on the other growth factors using the same system. This nano-patterned surface can also be combined with microprinting technology to look at cellular response within a confined shape.

As a demonstration, this study only showed one type of heterogeneous VEGF distribution. However, there are many more we can do. We can fix the distance between gold islands and vary the gold island size, or we can fix the gold island size but change the distance between them. Instead of looking at the difference between heterogeneous versus homogenous distribution of VEGF, we can actually look into the activation difference between different heterogeneous distributions. The results from this type of study can greatly impact the development of the implant industry. It has been known that the roughness of the surface, the presentation of bio-signals on implants can greatly affect therapeutic outcomes. It will be even more interesting to take the distribution effects of bio-signals into consideration.

Chapter 8

References

1. Gerber, H.P. et al. VEGF is required for growth and survival in neonatal mice. *Development***126**, 1149-1159 (1999).
2. Shalaby, F. et al. Failure of Blood-Island Formation and Vasculogenesis in Flk-1-Deficient Mice. *Nature***376**, 62-66 (1995).
3. Hynes, R.O. Integrins: bidirectional, allosteric signaling machines. *Cell***110**, 673-687 (2002).
4. Hynes, R.O. The Extracellular Matrix: Not Just Pretty Fibrils. *Science***326**, 1216-1219 (2009).
5. Giancotti, F.G. & Ruoslahti, E. Integrin signaling. *Science***285**, 1028-1032 (1999).
6. Milner, R. & Campbell, I.L. Developmental regulation of beta1 integrins during angiogenesis in the central nervous system. *Mol Cell Neurosci***20**, 616-626 (2002).
7. Brooks, P.C., Clark, R.A. & Cheresh, D.A. Requirement of vascular integrin alpha v beta 3 for angiogenesis. *Science***264**, 569-571 (1994).
8. Tonnesen, M.G., Feng, X. & Clark, R.A. Angiogenesis in wound healing. *J Investig Dermatol Symp Proc***5**, 40-46 (2000).
9. Friedlander, M. et al. Definition of two angiogenic pathways by distinct alpha v integrins. *Science***270**, 1500-1502 (1995).
10. Staatz, W.D., Rajpara, S.M., Wayner, E.A., Carter, W.G. & Santoro, S.A. The membrane glycoprotein Ia-IIa (VLA-2) complex mediates the Mg⁺⁺-dependent adhesion of platelets to collagen. *J Cell Biol***108**, 1917-1924 (1989).
11. Kirchhofer, D., Languino, L.R., Ruoslahti, E. & Pierschbacher, M.D. Alpha 2 beta 1 integrins from different cell types show different binding specificities. *J Biol Chem***265**, 615-618 (1990).
12. Elices, M.J. & Hemler, M.E. The human integrin VLA-2 is a collagen receptor on some cells and a collagen/laminin receptor on others. *Proc Natl Acad Sci U S A***86**, 9906-9910 (1989).
13. Hynes, R.O. & Bader, B.L. Targeted mutations in integrins and their ligands: Their implications for vascular biology. *Thromb Haemostasis***78**, 83-87 (1997).
14. Rupp, P.A. & Little, C.D. Integrins in vascular development. *Circulation research***89**, 566-572 (2001).
15. Stupack, D.G. & Cheresh, D.A. ECM remodeling regulates angiogenesis: endothelial integrins look for new ligands. *Sci STKE***2002**, pe7 (2002).

16. Zovein, A.C. et al. beta 1 Integrin Establishes Endothelial Cell Polarity and Arteriolar Lumen Formation via a Par3-Dependent Mechanism. *Dev Cell***18**, 39-51 (2010).
17. Bayless, K.J., Salazar, R. & Davis, G.E. RGD-dependent vacuolation and lumen formation observed during endothelial cell morphogenesis in three-dimensional fibrin matrices involves the alpha(v)beta(3) and alpha(5)beta(1) integrins. *Am J Pathol***156**, 1673-1683 (2000).
18. Mahabeleshwar, G.H. et al. Integrin affinity modulation in angiogenesis. *Cell Cycle***7**, 335-347 (2008).
19. Turlo, K.A. et al. An essential requirement for beta 1 integrin in the assembly of extracellular matrix proteins within the vascular wall. *Dev Biol***365**, 23-35 (2012).
20. Yamamoto, H. et al. Integrin beta1 controls VE-cadherin localization and blood vessel stability. *Nature communications***6**, 6429 (2015).
21. Hodivala-Dilke, K.M. et al. Beta3-integrin-deficient mice are a model for Glanzmann thrombasthenia showing placental defects and reduced survival. *J Clin Invest***103**, 229-238 (1999).
22. Weis, S.M. et al. Cooperation between VEGF and beta3 integrin during cardiac vascular development. *Blood***109**, 1962-1970 (2007).
23. Kumar, S. & Weaver, V.M. Mechanics, malignancy, and metastasis: the force journey of a tumor cell. *Cancer Metastasis Rev***28**, 113-127 (2009).
24. Carroll, J.M., Romero, M.R. & Watt, F.M. Suprabasal integrin expression in the epidermis of transgenic mice results in developmental defects and a phenotype resembling psoriasis. *Cell***83**, 957-968 (1995).
25. Reynolds, L.E. et al. Enhanced pathological angiogenesis in mice lacking beta3 integrin or beta3 and beta5 integrins. *Nat Med***8**, 27-34 (2002).
26. Alghisi, G.C., Ponsonnet, L. & Rugg, C. The integrin antagonist cilengitide activates alphaVbeta3, disrupts VE-cadherin localization at cell junctions and enhances permeability in endothelial cells. *PLoS one***4**, e4449 (2009).
27. Desgrosellier, J.S. & Cheresh, D.A. Integrins in cancer: biological implications and therapeutic opportunities. *Nat Rev Cancer***10**, 9-22 (2010).
28. Garmy-Susini, B. et al. Integrin alpha4beta1-VCAM-1-mediated adhesion between endothelial and mural cells is required for blood vessel maturation. *J Clin Invest***115**, 1542-1551 (2005).
29. Benoit, D.S. & Anseth, K.S. The effect on osteoblast function of colocalized RGD and PHSRN epitopes on PEG surfaces. *Biomaterials***26**, 5209-5220 (2005).
30. Mhanna, R. et al. GFOGER-modified MMP-sensitive polyethylene glycol hydrogels induce chondrogenic differentiation of human mesenchymal stem cells. *Tissue Eng Part A***20**, 1165-1174 (2014).

31. Shekaran, A. et al. Bone regeneration using an alpha 2 beta 1 integrin-specific hydrogel as a BMP-2 delivery vehicle. *Biomaterials***35**, 5453-5461 (2014).
32. Lee, S.T. et al. Engineering integrin signaling for promoting embryonic stem cell self-renewal in a precisely defined niche. *Biomaterials***31**, 1219-1226 (2010).
33. Gonzalez, A.L., Gobin, A.S., West, J.L., McIntire, L.V. & Smith, C.W. Integrin interactions with immobilized peptides in polyethylene glycol diacrylate hydrogels. *Tissue Eng***10**, 1775-1786 (2004).
34. Mann, B.K., Gobin, A.S., Tsai, A.T., Schmedlen, R.H. & West, J.L. Smooth muscle cell growth in photopolymerized hydrogels with cell adhesive and proteolytically degradable domains: synthetic ECM analogs for tissue engineering. *Biomaterials***22**, 3045-3051 (2001).
35. Martino, M.M. et al. Controlling integrin specificity and stem cell differentiation in 2D and 3D environments through regulation of fibronectin domain stability. *Biomaterials***30**, 1089-1097 (2009).
36. van der Walle, C.F., Altroff, H. & Mardon, H.J. Novel mutant human fibronectin FIII9-10 domain pair with increased conformational stability and biological activity. *Protein Eng***15**, 1021-1024 (2002).
37. Baron, M. et al. ¹H NMR assignment and secondary structure of the cell adhesion type III module of fibronectin. *Biochemistry***31**, 2068-2073 (1992).
38. Krammer, A., Craig, D., Thomas, W.E., Schulten, K. & Vogel, V. A structural model for force regulated integrin binding to fibronectin's RGD-synergy site. *Matrix Biol***21**, 139-147 (2002).
39. Grant, R.P., Spitzfaden, C., Altroff, H., Campbell, I.D. & Mardon, H.J. Structural requirements for biological activity of the ninth and tenth FIII domains of human fibronectin. *J Biol Chem***272**, 6159-6166 (1997).
40. Altroff, H. et al. Interdomain tilt angle determines integrin-dependent function of the ninth and tenth FIII domains of human fibronectin. *J Biol Chem***279**, 55995-56003 (2004).
41. Martino, M.M. et al. Engineering the Growth Factor Microenvironment with Fibronectin Domains to Promote Wound and Bone Tissue Healing. *Sci Transl Med***3** (2011).
42. Brown, A.C., Rowe, J.A. & Barker, T.H. Guiding epithelial cell phenotypes with engineered integrin-specific recombinant fibronectin fragments. *Tissue Eng Part A***17**, 139-150 (2011).
43. Kisiel, M. et al. Improving the osteogenic potential of BMP-2 with hyaluronic acid hydrogel modified with integrin-specific fibronectin fragment. *Biomaterials***34**, 704-712 (2013).
44. Martino, M.M. & Hubbell, J.A. The 12th-14th type III repeats of fibronectin function as a highly promiscuous growth factor-binding domain. *Faseb J***24**, 4711-4721 (2010).

45. Traub, S. et al. The promotion of endothelial cell attachment and spreading using FNIII10 fused to VEGF-A165. *Biomaterials***34**, 5958-5968 (2013).
46. Wijelath, E. et al. Enhancement of capillary and cellular ingrowth in ePTFE implants with a proangiogenic recombinant construct derived from fibronectin. *J Biomed Mater Res A***95**, 641-648 (2010).
47. Najjar, M. et al. Fibrin gels engineered with pro-angiogenic growth factors promote engraftment of pancreatic islets in extrahepatic sites in mice. *Biotechnol Bioeng***112**, 1916-1926 (2015).
48. Brady, A.C. et al. Proangiogenic hydrogels within macroporous scaffolds enhance islet engraftment in an extrahepatic site. *Tissue Eng Part A***19**, 2544-2552 (2013).
49. Holmes, K., Roberts, O.L., Thomas, A.M. & Cross, M.J. Vascular endothelial growth factor receptor-2: structure, function, intracellular signalling and therapeutic inhibition. *Cell Signal***19**, 2003-2012 (2007).
50. Roskoski, R. Vascular endothelial growth factor (VEGF) signaling in tumor progression. *Crit Rev Oncol Hemat***62**, 179-213 (2007).
51. Olsson, A.K., Dimberg, A., Kreuger, J. & Claesson-Welsh, L. VEGF receptor signalling - in control of vascular function. *Nat Rev Mol Cell Bio***7**, 359-371 (2006).
52. Ferrara, N., Gerber, H.P. & LeCouter, J. The biology of VEGF and its receptors. *Nat Med***9**, 669-676 (2003).
53. Giacca, M. & Zacchigna, S. VEGF gene therapy: therapeutic angiogenesis in the clinic and beyond. *Gene Ther***19**, 622-629 (2012).
54. Carmeliet, P. & Jain, R.K. Molecular mechanisms and clinical applications of angiogenesis. *Nature***473**, 298-307 (2011).
55. De Smet, F., Segura, I., De Bock, K., Hohensinner, P.J. & Carmeliet, P. Mechanisms of vessel branching: filopodia on endothelial tip cells lead the way. *Arterioscler Thromb Vasc Biol***29**, 639-649 (2009).
56. Potente, M., Gerhardt, H. & Carmeliet, P. Basic and therapeutic aspects of angiogenesis. *Cell***146**, 873-887 (2011).
57. Phelps, E.A. & Garcia, A.J. Engineering more than a cell: vascularization strategies in tissue engineering. *Curr Opin Biotechnol*.
58. Liu, L.Y., Ratner, B.D., Sage, E.H. & Jiang, S.Y. Endothelial cell migration on surface-density gradients of fibronectin, VEGF, or both proteins. *Langmuir***23**, 11168-11173 (2007).
59. Sun, Q. et al. Sustained release of multiple growth factors from injectable polymeric system as a novel therapeutic approach towards angiogenesis. *Pharm Res***27**, 264-271.

60. Peattie, R.A. et al. Effect of gelatin on heparin regulation of cytokine release from hyaluronan-based hydrogels. *Drug Deliv***15**, 389-397 (2008).
61. Backer, M.V., Patel, V., Jehning, B.T., Claffey, K.P. & Backer, J.M. Surface immobilization of active vascular endothelial growth factor via a cysteine-containing tag. *Biomaterials***27**, 5452-5458 (2006).
62. Zisch, A.H., Schenk, U., Schense, J.C., Sakiyama-Elbert, S.E. & Hubbell, J.A. Covalently conjugated VEGF-fibrin matrices for endothelialization. *J Control Release***72**, 101-113 (2001).
63. Moon, J.J. et al. Biomimetic hydrogels with pro-angiogenic properties. *Biomaterials***31**, 3840-3847.
64. Phelps, E.A., Landazuri, N., Thule, P.M., Taylor, W.R. & Garcia, A.J. Bioartificial matrices for therapeutic vascularization. *Proc Natl Acad Sci U S A***107**, 3323-3328.
65. Zisch, A.H. et al. Cell-demanded release of VEGF from synthetic, biointeractive cell ingrowth matrices for vascularized tissue growth. *FASEB J***17**, 2260-2262 (2003).
66. Lee, S., Jilani, S.M., Nikolova, G.V., Carpizo, D. & Iruela-Arispe, M.L. Processing of VEGF-A by matrix metalloproteinases regulates bioavailability and vascular patterning in tumors. *J. Cell Biol.***169**, 681-691 (2005).
67. Chen, T.T. et al. Anchorage of VEGF to the extracellular matrix conveys differential signaling responses to endothelial cells. *J Cell Biol***188**, 595-609.
68. Fairbrother, W.J., Champe, M.A., Christinger, H.W., Keyt, B.A. & Starovasnik, M.A. Solution structure of the heparin-binding domain of vascular endothelial growth factor. *Structure***6**, 637-648 (1998).
69. Ruhrberg, C. et al. Spatially restricted patterning cues provided by heparin-binding VEGF-A control blood vessel branching morphogenesis. *Gene Dev***16**, 2684-2698 (2002).
70. Lee, S., Jilani, S.M., Nikolova, G.V., Carpizo, D. & Iruela-Arispe, M.L. Processing of VEGF-A by matrix metalloproteinases regulates bioavailability and vascular patterning in tumors. *J Cell Biol***169**, 681-691 (2005).
71. von Degenfeld, G. et al. Microenvironmental VEGF distribution is critical for stable and functional vessel growth in ischemia. *Faseb J***20**, 2657-2659 (2006).
72. Dor, Y. et al. Conditional switching of VEGF provides new insights into adult neovascularization and pro-angiogenic therapy. *EMBO J***21**, 1939-1947 (2002).
73. Lee, R.J. et al. VEGF gene delivery to myocardium: deleterious effects of unregulated expression. *Circulation***102**, 898-901 (2000).
74. Golub, J.S. et al. Sustained VEGF delivery via PLGA nanoparticles promotes vascular growth. *Am J Physiol-Heart C***298**, H1959-H1965 (2010).

75. Formiga, F.R. et al. Sustained release of VEGF through PLGA microparticles improves vasculogenesis and tissue remodeling in an acute myocardial ischemia-reperfusion model. *Journal of Controlled Release***147**, 30-37 (2010).
76. Bible, E. et al. Neo-vascularization of the stroke cavity by implantation of human neural stem cells on VEGF-releasing PLGA microparticles. *Biomaterials***33**, 7435-+ (2012).
77. Simon-Yarza, T. et al. PEGylated-PLGA microparticles containing VEGF for long term drug delivery. *Int J Pharm***440**, 13-18 (2013).
78. Parajo, Y., d'Angelo, I., Welle, A., Garcia-Fuentes, M. & Alonso, M.J. Hyaluronic acid/Chitosan nanoparticles as delivery vehicles for VEGF and PDGF-BB. *Drug Deliv***17**, 596-604 (2010).
79. Amsden, B.G. et al. VEGF-induced angiogenesis following localized delivery via injectable, low viscosity poly(trimethylene carbonate). *Journal of Controlled Release***145**, 109-115 (2010).
80. Borselli, C. et al. Bioactivation of collagen matrices through sustained VEGF release from PLGA microspheres. *Journal of Biomedical Materials Research Part A***92A**, 94-102 (2010).
81. Park, K. Efficient delivery of VEGF via heparin-functionalized nanoparticle-fibrin complex. *Journal of Controlled Release***143**, 281-281 (2010).
82. Chung, Y.I. et al. Efficient revascularization by VEGF administration via heparin-functionalized nanoparticle-fibrin complex. *Journal of controlled release : official journal of the Controlled Release Society***143**, 282-289 (2010).
83. Geng, H.Q., Song, H., Qi, J. & Cui, D.X. Sustained release of VEGF from PLGA nanoparticles embedded thermo-sensitive hydrogel in full-thickness porcine bladder acellular matrix. *Nanoscale Res Lett***6** (2011).
84. Wang, J.H. et al. Continued sustained release of VEGF by PLGA nanospheres modified BAMG stent for the anterior urethral reconstruction of rabbit. *Asian Pac J Trop Med***6**, 481-484 (2013).
85. Singh, S., Wu, B.M. & Dunn, J.C.Y. Delivery of VEGF using collagen-coated polycaprolactone scaffolds stimulates angiogenesis. *Journal of Biomedical Materials Research Part A***100A**, 720-727 (2012).
86. Poh, C.K. et al. In vitro characterizations of mesoporous hydroxyapatite as a controlled release delivery device for VEGF in orthopedic applications. *Journal of Biomedical Materials Research Part A***100A**, 3143-3150 (2012).
87. Strieth, S. et al. Biocompatibility of porous polyethylene implants tissue-engineered by extracellular matrix and VEGF. *Journal of Biomedical Materials Research Part A***93A**, 1566-1573 (2010).

88. Jabbarzadeh, E. et al. VEGF-incorporated biomimetic poly(lactide-co-glycolide) sintered microsphere scaffolds for bone tissue engineering. *J Biomed Mater Res B Appl Biomater***100**, 2187-2196 (2012).
89. Choi, J.Y. et al. Fabrication and In Vivo Evaluation of the Electrospun Small Diameter Vascular Grafts Composed of Elastin/PLGA/PCL and Heparin-VEGF. *Tissue Eng Regen Med***7**, 149-154 (2010).
90. Jia, X.L. et al. Sustained Release of VEGF by Coaxial Electrospun Dextran/PLGA Fibrous Membranes in Vascular Tissue Engineering. *J Biomat Sci-Polym E***22**, 1811-1827 (2011).
91. Chen, L. et al. Loading of VEGF to the heparin cross-linked demineralized bone matrix improves vascularization of the scaffold. *J Mater Sci-Mater M***21**, 309-317 (2010).
92. Zhang, H. et al. Dual-delivery of VEGF and PDGF by double-layered electrospun membranes for blood vessel regeneration. *Biomaterials***34**, 2202-2212 (2013).
93. Willems, W.F., Larsen, M., Friedrich, P.F., Shogren, K.L. & Bishop, A.T. Induction of angiogenesis and osteogenesis in surgically revascularized frozen bone allografts by sustained delivery of FGF-2 and VEGF. *J Orthop Res***30**, 1556-1562 (2012).
94. Simon-Yarza, T. et al. Functional benefits of PLGA particulates carrying VEGF and CoQ(10) in an animal of myocardial ischemia. *Int J Pharmaceut***454**, 784-790 (2013).
95. Shin, S.H. et al. Sequential delivery of TAT-HSP27 and VEGF using microsphere/hydrogel hybrid systems for therapeutic angiogenesis. *Journal of Controlled Release***166**, 38-45 (2013).
96. Jay, S.M. et al. Dual delivery of VEGF and MCP-1 to support endothelial cell transplantation for therapeutic vascularization. *Biomaterials***31**, 3054-3062 (2010).
97. Holmes, K., Roberts, O.L., Thomas, A.M. & Cross, M.J. Vascular endothelial growth factor receptor-2: structure, function, intracellular signalling and therapeutic inhibition. *Cell Signal***19**, 2003-2012 (2007).
98. Koch, S. & Claesson-Welsh, L. Signal transduction by vascular endothelial growth factor receptors. *Cold Spring Harb Perspect Med***2**, a006502 (2012).
99. Chen, T.T. et al. Anchorage of VEGF to the extracellular matrix conveys differential signaling responses to endothelial cells. *J Cell Biol***188**, 595-609 (2010).
100. Olsson, A.K., Dimberg, A., Kreuger, J. & Claesson-Welsh, L. VEGF receptor signalling - in control of vascular function. *Nat Rev Mol Cell Biol***7**, 359-371 (2006).
101. Murata, T. et al. Role of prostaglandin D2 receptor DP as a suppressor of tumor hyperpermeability and angiogenesis in vivo. *Proc Natl Acad Sci U S A***105**, 20009-20014 (2008).
102. Curtis, A.S. & Varde, M. Control of Cell Behavior: Topological Factors. *J Natl Cancer Inst***33**, 15-26 (1964).

103. Das, G.D., Lammert, G.L. & McAllister, J.P. Contact guidance and migratory cells in the developing cerebellum. *Brain Res***69**, 13-29 (1974).
104. Arnold, M. et al. Activation of integrin function by nanopatterned adhesive interfaces. *Chemphyschem***5**, 383-388 (2004).
105. Lam, J. & Segura, T. The modulation of MSC integrin expression by RGD presentation. *Biomaterials***34**, 3938-3947 (2013).
106. Anderson, S.M., Siegman, S.N. & Segura, T. The effect of vascular endothelial growth factor (VEGF) presentation within fibrin matrices on endothelial cell branching. *Biomaterials***32**, 7432-7443 (2011).
107. Kolodziej, C.M. et al. Combination of integrin-binding peptide and growth factor promotes cell adhesion on electron-beam-fabricated patterns. *J Am Chem Soc***134**, 247-255 (2012).
108. Qi, L. et al. The effects of topographical patterns and sizes on neural stem cell behavior. *PLoS one***8**, e59022 (2013).
109. Dalby, M.J., Gadegaard, N., Riehle, M.O., Wilkinson, C.D. & Curtis, A.S. Investigating filopodia sensing using arrays of defined nano-pits down to 35 nm diameter in size. *Int J Biochem Cell Biol***36**, 2005-2015 (2004).
110. Andersson, A.S. et al. Nanoscale features influence epithelial cell morphology and cytokine production. *Biomaterials***24**, 3427-3436 (2003).
111. Pesen, D. & Haveland, D.B. Modulation of cell adhesion complexes by surface protein patterns. *ACS Appl Mater Interfaces***1**, 543-548 (2009).
112. Malmstrom, J. et al. Large area protein patterning reveals nanoscale control of focal adhesion development. *Nano Lett***10**, 686-694 (2010).
113. Malmstrom, J. et al. Focal complex maturation and bridging on 200 nm vitronectin but not fibronectin patches reveal different mechanisms of focal adhesion formation. *Nano Lett***11**, 2264-2271 (2011).
114. Boggild, T., Runager, K. & Sutherland, D.S. Nanopattern Gradients for Cell Studies Fabricated Using Hole-Mask Colloidal Lithography. *ACS Appl Mater Interfaces***8**, 14975-14979 (2016).
115. Arnold, M. et al. Induction of cell polarization and migration by a gradient of nanoscale variations in adhesive ligand spacing. *Nano Lett***8**, 2063-2069 (2008).
116. Huang, J. et al. Impact of order and disorder in RGD nanopatterns on cell adhesion. *Nano Lett***9**, 1111-1116 (2009).
117. Lin, H.B., Zhao, Z.C., Garcia-Echeverria, C., Rich, D.H. & Cooper, S.L. Synthesis of a novel polyurethane co-polymer containing covalently attached RGD peptide. *Journal of biomaterials science. Polymer edition***3**, 217-227 (1992).

118. Ghosh, K., Ren, X.D., Shu, X.Z., Prestwich, G.D. & Clark, R.A. Fibronectin functional domains coupled to hyaluronan stimulate adult human dermal fibroblast responses critical for wound healing. *Tissue Eng***12**, 601-613 (2006).
119. Hou, S. et al. The repair of brain lesion by implantation of hyaluronic acid hydrogels modified with laminin. *J Neurosci Methods***148**, 60-70 (2005).
120. Brown, A.C., Dysart, M.M., Clarke, K.C., Stabenfeldt, S.E. & Barker, T.H. Integrin alpha3beta1 Binding to Fibronectin Is Dependent on the Ninth Type III Repeat. *J Biol Chem***290**, 25534-25547 (2015).
121. Markowski, M.C., Brown, A.C. & Barker, T.H. Directing epithelial to mesenchymal transition through engineered microenvironments displaying orthogonal adhesive and mechanical cues. *J Biomed Mater Res A***100**, 2119-2127 (2012).
122. Schense, J.C. & Hubbell, J.A. Cross-linking exogenous bifunctional peptides into fibrin gels with factor XIIIa. *Bioconjug Chem***10**, 75-81 (1999).
123. Lei, Y., Gojgini, S., Lam, J. & Segura, T. The spreading, migration and proliferation of mouse mesenchymal stem cells cultured inside hyaluronic acid hydrogels. *Biomaterials***32**, 39-47 (2011).
124. Li, X. et al. Genetic control of the rate of wound healing in mice. *Heredity (Edinb)***86**, 668-674 (2001).
125. Carmichael, S.T. Rodent models of focal stroke: size, mechanism, and purpose. *NeuroRx***2**, 396-409 (2005).
126. Hoeben, A. et al. Vascular endothelial growth factor and angiogenesis. *Pharmacol Rev***56**, 549-580 (2004).
127. Nakatsu, M.N., Davis, J. & Hughes, C.C. Optimized fibrin gel bead assay for the study of angiogenesis. *J Vis Exp*, 186 (2007).
128. Nakatsu, M.N. et al. Angiogenic sprouting and capillary lumen formation modeled by human umbilical vein endothelial cells (HUVEC) in fibrin gels: the role of fibroblasts and Angiopoietin-1. *Microvasc Res***66**, 102-112 (2003).
129. Carmeliet, P. & Jain, R.K. Angiogenesis in cancer and other diseases. *Nature***407**, 249-257 (2000).
130. Santulli, R.J. et al. Studies with an orally bioavailable alpha V integrin antagonist in animal models of ocular vasculopathy: retinal neovascularization in mice and retinal vascular permeability in diabetic rats. *J Pharmacol Exp Ther***324**, 894-901 (2008).
131. Aota, S., Nomizu, M. & Yamada, K.M. The short amino acid sequence Pro-His-Ser-Arg-Asn in human fibronectin enhances cell-adhesive function. *J Biol Chem***269**, 24756-24761 (1994).

132. Danen, E.H. et al. Requirement for the synergy site for cell adhesion to fibronectin depends on the activation state of integrin alpha 5 beta 1. *J Biol Chem***270**, 21612-21618 (1995).
133. Mogford, J.E., Davis, G.E., Platts, S.H. & Meininger, G.A. Vascular smooth muscle alpha v beta 3 integrin mediates arteriolar vasodilation in response to RGD peptides. *Circulation research***79**, 821-826 (1996).
134. Voura, E.B., Ramjeesingh, R.A., Montgomery, A.M. & Siu, C.H. Involvement of integrin alpha(v)beta(3) and cell adhesion molecule L1 in transendothelial migration of melanoma cells. *Molecular biology of the cell***12**, 2699-2710 (2001).
135. Friedlander, M. et al. Involvement of integrins alpha v beta 3 and alpha v beta 5 in ocular neovascular diseases. *Proc Natl Acad Sci U S A***93**, 9764-9769 (1996).
136. Henderson, N.C. et al. Targeting of alphav integrin identifies a core molecular pathway that regulates fibrosis in several organs. *Nat Med***19**, 1617-1624 (2013).
137. Fiore, V.F. et al. Conformational coupling of integrin and Thy-1 regulates Fyn priming and fibroblast mechanotransduction. *J Cell Biol***211**, 173-190 (2015).
138. Liu, Z., Wang, F. & Chen, X. Integrin alpha(v)beta(3)-Targeted Cancer Therapy. *Drug Dev Res***69**, 329-339 (2008).
139. Danhier, F., Le Breton, A. & Preat, V. RGD-based strategies to target alpha(v) beta(3) integrin in cancer therapy and diagnosis. *Mol Pharm***9**, 2961-2973 (2012).
140. De Smet, F., Segura, I., De Bock, K., Hohensinner, P.J. & Carmeliet, P. Mechanisms of Vessel Branching Filopodia on Endothelial Tip Cells Lead the Way. *Arterioscl Throm Vas***29**, 639-649 (2009).
141. Adams, R.H. & Alitalo, K. Molecular regulation of angiogenesis and lymphangiogenesis. *Nat Rev Mol Cell Bio***8**, 464-478 (2007).
142. Isogai, S., Lawson, N.D., Torrealday, S., Horiguchi, M. & Weinstein, B.M. Angiogenic network formation in the developing vertebrate trunk. *Development***130**, 5281-5290 (2003).
143. Wacker, A. & Gerhardt, H. Endothelial development taking shape. *Current opinion in cell biology***23**, 676-685 (2011).
144. Lenard, A. et al. In vivo analysis reveals a highly stereotypic morphogenetic pathway of vascular anastomosis. *Dev Cell***25**, 492-506 (2013).
145. Wallez, Y., Vilgrain, I. & Huber, P. Angiogenesis: the VE-cadherin switch. *Trends Cardiovasc Med***16**, 55-59 (2006).
146. Montero-Balaguer, M. et al. Stable vascular connections and remodeling require full expression of VE-cadherin in zebrafish embryos. *PLoS one***4**, e5772 (2009).

147. Lei, Y. & Segura, T. DNA delivery from matrix metalloproteinase degradable poly(ethylene glycol) hydrogels to mouse cloned mesenchymal stem cells. *Biomaterials***30**, 254-265 (2009).
148. Zhu, S., Nih, L., Carmichael, S.T., Lu, Y. & Segura, T. Enzyme-Responsive Delivery of Multiple Proteins with Spatiotemporal Control. *Adv Mater***27**, 3620-3625 (2015).
149. Wen, J. et al. Controlled Protein Delivery Based on Enzyme-Responsive Nanocapsules. *Advanced Materials***23**, 4549-4553 (2011).
150. Zhu, S. & Segura, T. Cell-Demanded VEGF Release via Nanocapsules Elicits Different Receptor Activation Dynamics and Enhanced Angiogenesis. *Ann Biomed Eng***44**, 1983-1992 (2016).
151. Yang, J.P., Liu, H.J. & Liu, X.F. VEGF promotes angiogenesis and functional recovery in stroke rats. *J Invest Surg***23**, 149-155 (2010).
152. Taimeh, Z., Loughran, J., Birks, E.J. & Bolli, R. Vascular endothelial growth factor in heart failure. *Nat Rev Cardiol***10**, 519-530 (2013).
153. Detmar, M. The role of VEGF and thrombospondins in skin angiogenesis. *J Dermatol Sci***24 Suppl 1**, S78-84 (2000).
154. Alon, T. et al. Vascular Endothelial Growth-Factor Acts as a Survival Factor for Newly Formed Retinal-Vessels and Has Implications for Retinopathy of Prematurity. *Nat Med***1**, 1024-1028 (1995).
155. Henry, T.D. et al. The VIVA trial: Vascular endothelial growth factor in Ischemia for Vascular Angiogenesis. *Circulation***107**, 1359-1365 (2003).
156. Kastrup, J. et al. Direct intramyocardial plasmid vascular endothelial growth factor-A165 gene therapy in patients with stable severe angina pectoris A randomized double-blind placebo-controlled study: the Euroinject One trial. *J Am Coll Cardiol***45**, 982-988 (2005).
157. Stewart, D.J. et al. Angiogenic gene therapy in patients with nonrevascularizable ischemic heart disease: a phase 2 randomized, controlled trial of AdVEGF(121) (AdVEGF121) versus maximum medical treatment. *Gene Ther***13**, 1503-1511 (2006).
158. Hedman, M. et al. Safety and feasibility of catheter-based local intracoronary vascular endothelial growth factor gene transfer in the prevention of postangioplasty and in-stent restenosis and in the treatment of chronic myocardial ischemia: phase II results of the Kuopio Angiogenesis Trial (KAT). *Circulation***107**, 2677-2683 (2003).
159. Roberts, W.G. & Palade, G.E. Increased microvascular permeability and endothelial fenestration induced by vascular endothelial growth factor. *Journal of cell science***108 (Pt 6)**, 2369-2379 (1995).
160. Esser, S. et al. Vascular endothelial growth factor induces endothelial fenestrations in vitro. *J Cell Biol***140**, 947-959 (1998).

161. Andres, R.H. et al. The CCR2/CCL2 Interaction Mediates the Transendothelial Recruitment of Intravascularly Delivered Neural Stem Cells to the Ischemic Brain. *Stroke* (2011).
162. Arai, K., Jin, G., Navaratna, D. & Lo, E.H. Brain angiogenesis in developmental and pathological processes: neurovascular injury and angiogenic recovery after stroke. *Febs J***276**, 4644-4652 (2009).
163. Xiong, Y., Mahmood, A. & Chopp, M. Angiogenesis, neurogenesis and brain recovery of function following injury. *Curr Opin Investig Drugs***11**, 298-308 (2010).
164. Coon, W.W., Willis, P.W., 3rd & Keller, J.B. Venous thromboembolism and other venous disease in the Tecumseh community health study. *Circulation***48**, 839-846 (1973).
165. Amlung, S.R., Miller, W.L. & Bosley, L.M. The 1999 National Pressure Ulcer Prevalence Survey: a benchmarking approach. *Adv Skin Wound Care***14**, 297-301 (2001).
166. Valensi, P., Girod, I., Baron, F., Moreau-Defarges, T. & Guillon, P. Quality of life and clinical correlates in patients with diabetic foot ulcers. *Diabetes Metab***31**, 263-271 (2005).
167. Faglia, E. et al. The role of early surgical debridement and revascularization in patients with diabetes and deep foot space abscess: retrospective review of 106 patients with diabetes. *J Foot Ankle Surg***45**, 220-226 (2006).
168. Davis, W.A., Norman, P.E., Bruce, D.G. & Davis, T.M. Predictors, consequences and costs of diabetes-related lower extremity amputation complicating type 2 diabetes: the Fremantle Diabetes Study. *Diabetologia***49**, 2634-2641 (2006).
169. Malay, D.S., Margolis, D.J., Hoffstad, O.J. & Bellamy, S. The incidence and risks of failure to heal after lower extremity amputation for the treatment of diabetic neuropathic foot ulcer. *J Foot Ankle Surg***45**, 366-374 (2006).
170. Galiano, R.D. et al. Topical vascular endothelial growth factor accelerates diabetic wound healing through increased angiogenesis and by mobilizing and recruiting bone marrow-derived cells. *Am J Pathol***164**, 1935-1947 (2004).
171. Wetzler, C., Kampfer, H., Stallmeyer, B., Pfeilschifter, J. & Frank, S. Large and sustained induction of chemokines during impaired wound healing in the genetically diabetic mouse: prolonged persistence of neutrophils and macrophages during the late phase of repair. *J Invest Dermatol***115**, 245-253 (2000).
172. Albertson, S., Hummel, R.P., 3rd, Breeden, M. & Greenhalgh, D.G. PDGF and FGF reverse the healing impairment in protein-malnourished diabetic mice. *Surgery***114**, 368-372; discussion 372-363 (1993).
173. Carmeliet, P. et al. Abnormal blood vessel development and lethality in embryos lacking a single VEGF allele. *Nature***380**, 435-439 (1996).
174. Ferrara, N. et al. Heterozygous embryonic lethality induced by targeted inactivation of the VEGF gene. *Nature***380**, 439-442 (1996).

175. Lee, S. et al. Autocrine VEGF signaling is required for vascular homeostasis. *Cell***130**, 691-703 (2007).
176. Wang, Z., Zhang, J. & Zhang, B. Vascular endothelial growth factor gene expression in patients' ischemic skeletal muscle with diabetic foot. *Zhonghua Yu Fang Yi Xue Za Zhi***36**, 505-507 (2002).
177. Frank, S. et al. Regulation of vascular endothelial growth factor expression in cultured keratinocytes. Implications for normal and impaired wound healing. *J Biol Chem***270**, 12607-12613 (1995).
178. Ferrara, N. Molecular and biological properties of vascular endothelial growth factor. *J Mol Med (Berl)***77**, 527-543 (1999).
179. Yamagishi, S. et al. Vascular endothelial growth factor acts as a pericyte mitogen under hypoxic conditions. *Lab Invest***79**, 501-509 (1999).
180. Griffioen, A.W. & Molema, G. Angiogenesis: potentials for pharmacologic intervention in the treatment of cancer, cardiovascular diseases, and chronic inflammation. *Pharmacol Rev***52**, 237-268 (2000).
181. Brkovic, A. & Sirois, M.G. Vascular permeability induced by VEGF family members in vivo: role of endogenous PAF and NO synthesis. *J Cell Biochem***100**, 727-737 (2007).
182. Gavard, J. & Gutkind, J.S. VEGF controls endothelial-cell permeability by promoting the beta-arrestin-dependent endocytosis of VE-cadherin. *Nat Cell Biol***8**, 1223-U1217 (2006).
183. Hanft, J.R. et al. Phase I trial on the safety of topical rhVEGF on chronic neuropathic diabetic foot ulcers. *J Wound Care***17**, 30-32, 34-37 (2008).
184. Ozawa, C.R. et al. Microenvironmental VEGF concentration, not total dose, determines a threshold between normal and aberrant angiogenesis. *J Clin Invest***113**, 516-527 (2004).
185. Koch, S. et al. Enhancing angiogenesis in collagen matrices by covalent incorporation of VEGF. *J Mater Sci-Mater M***17**, 735-741 (2006).
186. Rousou, J. et al. Randomized clinical trial of fibrin sealant in patients undergoing re sternotomy or reoperation after cardiac operations. A multicenter study. *J Thorac Cardiovasc Surg***97**, 194-203 (1989).
187. Anderson, S.M. et al. VEGF internalization is not required for VEGFR-2 phosphorylation in bioengineered surfaces with covalently linked VEGF. *Integr Biol-Uk***3**, 887-896 (2011).
188. Warren, C.M., Ziyad, S., Briot, A., Der, A. & Iruela-Arispe, M.L. A ligand-independent VEGFR2 signaling pathway limits angiogenic responses in diabetes. *Science signaling***7**, ra1 (2014).
189. Carmeliet, P. & Jain, R.K. Principles and mechanisms of vessel normalization for cancer and other angiogenic diseases. *Nat Rev Drug Discov***10**, 417-427 (2011).

190. Nakatsu, M.N. et al. VEGF(121) and VEGF(165) regulate blood vessel diameter through vascular endothelial growth factor receptor 2 in an in vitro angiogenesis model. *Lab Invest***83**, 1873-1885 (2003).
191. Nicosia, R.F. The aortic ring model of angiogenesis: a quarter century of search and discovery. *Journal of cellular and molecular medicine***13**, 4113-4136 (2009).
192. Anderson, S.M., Chen, T.T., Iruela-Arispe, M.L. & Segura, T. The phosphorylation of vascular endothelial growth factor receptor-2 (VEGFR-2) by engineered surfaces with electrostatically or covalently immobilized VEGF. *Biomaterials***30**, 4618-4628 (2009).
193. Keyt, B.A. et al. The carboxyl-terminal domain (111-165) of vascular endothelial growth factor is critical for its mitogenic potency. *J Biol Chem***271**, 7788-7795 (1996).
194. Lan, S., Veisoh, M. & Zhang, M. Surface modification of silicon and gold-patterned silicon surfaces for improved biocompatibility and cell patterning selectivity. *Biosens Bioelectron***20**, 1697-1708 (2005).
195. Shiojima, I. & Walsh, K. Role of Akt signaling in vascular homeostasis and angiogenesis. *Circulation research***90**, 1243-1250 (2002).
196. Gourlaouen, M., Welti, J.C., Vasudev, N.S. & Reynolds, A.R. Essential role for endocytosis in the growth factor-stimulated activation of ERK1/2 in endothelial cells. *J Biol Chem***288**, 7467-7480 (2013).
197. Dellinger, M.T. & Brekken, R.A. Phosphorylation of Akt and ERK1/2 is required for VEGF-A/VEGFR2-induced proliferation and migration of lymphatic endothelium. *PLoS one***6**, e28947 (2011).
198. Lamalice, L., Houle, F. & Huot, J. Phosphorylation of Tyr1214 within VEGFR-2 triggers the recruitment of Nck and activation of Fyn leading to SAPK2/p38 activation and endothelial cell migration in response to VEGF. *J Biol Chem***281**, 34009-34020 (2006).
199. Geudens, I. & Gerhardt, H. Coordinating cell behaviour during blood vessel formation. *Development***138**, 4569-4583 (2011).
200. Blanco, R. & Gerhardt, H. VEGF and Notch in tip and stalk cell selection. *Cold Spring Harb Perspect Med***3**, a006569 (2013).
201. Suchting, S. et al. The Notch ligand Delta-like 4 negatively regulates endothelial tip cell formation and vessel branching. *Proc Natl Acad Sci U S A***104**, 3225-3230 (2007).
202. Benedito, R. et al. Notch-dependent VEGFR3 upregulation allows angiogenesis without VEGF-VEGFR2 signalling. *Nature***484**, 110-114 (2012).
203. Hofmann, J.J. & Iruela-Arispe, M.L. Notch signaling in blood vessels: who is talking to whom about what? *Circ Res***100**, 1556-1568 (2007).
204. Benedito, R. et al. The Notch Ligands Dll4 and Jagged1 Have Opposing Effects on Angiogenesis. *Cell***137**, 1124-1135 (2009).

205. Mathieu, P.S. & Lobo, E.G. Cytoskeletal and Focal Adhesion Influences on Mesenchymal Stem Cell Shape, Mechanical Properties, and Differentiation Down Osteogenic, Adipogenic, and Chondrogenic Pathways. *Tissue Eng Part B-Re***18**, 436-444 (2012).